Master Thesis, Department of Geosciences

Fault architecture in extensional faults affecting sandstone, Northumberland, Great Britain

Marie Lovise Rostad Valdresbråten

UNIVERSITY OF OSLO

FACULTY OF MATHEMATICS AND NATURAL SCIENCES

Fault architecture in extensional faults affecting sandstone, Northumberland, Great Britain

Marie Lovise Rostad Valdresbråten

Master Thesis in Geosciences

Discipline: Geology

Department of Geosciences

Faculty of Mathematics and Natural Sciences

University of Oslo

01.06.11

Acknowledgements

First and foremost I would like to thank my primary supervisor, Professor Roy H. Gabrielsen, this thesis would not have been possible to write without the guidance and support I received from him. I would also like to thank my supervisor Professor Roald B. Færseth for the invaluable guidance he provided during fieldwork. Senior researcher Simon Buckley has been a great resource who has scanned and prepared the LiDAR data essential to this thesis, of which I am also very grateful.

Further, I owe my deepest gratitude to Master Student Shaun Eaves for reading through the manuscript and giving constructive criticism. I would also like to make a special reference to Phd Student Jord de Boer and Jorunn Valdresbråten who has read through parts of the manuscript.

I am also grateful for valuable social and scientific discussions with my fellow students, with special regards to Linda I. Holm, Erik Jensen and Magnus V. Kjemperud, with additional thanks directed to Magnus V. Kjemperud for assistance and discussions during fieldwork and Erik Jensen for help and guidance with software such as adobe.

Abstract

The study of fluid flow in faults has lately gained much attention, due its impact on the production profiles in hydrocarbon fields and its potential influence on the sealing capacity of cap rock. In the modelling of such systems, detailed understanding of fault architecture is crucial.

The present study particularly focuses on the study of fault architecture in sandy sequences. Fieldwork was carried out at two coastal locations (Crag Point and Snab Point), within the Northumberland Basin, Northern England (Kimbell et al. 1989). Faults found in these localities affect homogeneous sandstone from the coal measure strata of Carboniferous age (Jones 1968). They are characterized by steeply dipping fault systems. Datasets include those utilized from satellite imagery, aerial photography, field observations, and LiDAR scan data.

The localities offer good exposures of fault cores in vertical as well as in horizontal sections. Geometry and orientation of the master fault planes and their associated fracture systems were determined. Thereafter, the size of the main fault lens axes and the orientation of these axes were measured. These data provide a statistical database. Both faults are affected by well-developed hanging and footwall wall damage zones. It is realized that both fault systems studied by us are subordinate structures in the hanging walls and footwalls of larger faults with displacements in the order of hundred of meters.

The steep geometry of the faults is ascribed to effects due to reactivation and/or lithological control. Fault core thickness of the faults in this study is related to amount of displacement and proportional to amount of lenses within the core. The lenses in this study are relatively thicker than lens relations stated in the literature (Lindanger et al. 2007, Bastesen et al. 2009, Braathen et al. 2009) where the faults vertical displacement has negligible importance on lens thickness. The conclusion drawn from this is that the individual fault systems exercise great control on lens dimensions. The probability of the fault systems in this thesis to be sealing or have any influence on fluid flow is dependent on degree of cementation as no membranes of significance is observed.

Table of contents

1. Introduction

1.1 Objectives

This is a one year master thesis in geology conducted at the University of Oslo and is based on fieldwork in England including detailed LiDAR scanning and structural analysis. The thesis work was in collaboration with the University of Oslo (UiO) and the Centre for Integrated Petroleum Research at the University of Bergen (UiB). The project encompasses petroleum geology and structural geology and was created by the Centre for Integrated Petroleum Research.

The study of fluid flow in faults has received much attention of late, due to its impact on the production profiles in hydrocarbon fields and its potential influence on the sealing capacity of cap rock (e.g.Caine et al. 1996, Heynekamp et al. 1999, Braathen et al. 2004). To better understand what influences fluid flow in the subsurface it is important to conduct field analogue studies. The foremost scientific aim of this thesis is to study the architecture, fault facies and properties of two faults exhibiting sand-sand juxtaposition by detailed description and analysis. Subsequently the faults geometry and their relation to the regional setting are studied and seen in relation to the fault architecture. This thesis is part of the Fault Facies II project at the Centre for Integrated Petroleum Research and results obtained in this thesis will be added to a database of previously studied fault facies.

1.2 Study area and accessibility

Fieldwork was conducted over a period stretching three weeks in the summer of 2010, from June 17 to July 9. Supervisors' Professor Roy H. Gabrielsen and Professor Roald B.Færseth accompanied the author for the first week in order to give an introduction to the regional geology as well as field methods to be used. Data was collected from June 20 onward and was carried out with field support from Magnus V. Kjemperud and email communication with Roy H. Gabrielsen and Roald B.Færseth.

Two field sites were studied, both situated along coastal sections in the Northumberland Basin, North-eastern England. The fault systems at both sites displace fluvial sandstone ofthe middle Coal Measure strata of Carboniferous age. Crag Point is the southernmost locality with Snab Point approximately 17km to the north.

Snab Point is located in Morpheth, south of Cresswell (UTM coordinates 0593625E, 6121214N; figure 1.1, see road map sheet OS Landranger Map 81). From Newcastle-Upon-Tyne take the A189 approximately 30km northbound to Ellington (Figure 1.1). Turn right at Ellington roundabout following signs to Cresswell before turning right to the first seafront car park south of Golden Sands Holiday Park (Figure 1.1). The locality at Snab Point is easily accessed from a parking lot at the cliff tops above, 200m south of Golden Sands Holiday Park (figure 1.1).

Figure 1. 1 Snab Point Study area (GoogleMaps™ 2011). Picture to the left displays Snab Points location in relation to Cresswell and Ellington. The red square marks the location of the picture to the right which is a close up of Snab Point modified from GoogleMaps™(2011)

Crag Point is located on the coastal section between Whitley Sluice and Hartley Steps (UTM coordinates 0598077E 6104577N; figure 1.2 see roadmap OS Landranger Map 88). The locality at Crag Point was accessed from the Hartley Steps car park. From Blyth, travel 7km south on the A193 before turning left at a roundabout at the southern end of Seaton Sluice (figure 1.2). The car park is located at the end of this road, from which it is less than 1km walk to crag Point cliff face going down Hartley steps then walking below the cliffs along the coast in a northerly direction (figure 1.2).

Figure 1. 2 Crag Point study area (GoogleMaps™ 2011). a) Marks the location of the study area in a regional setting. Red square marks of the picture to the right which is a close up of Crag Point modified from GoogleMaps™(2011)

At Crag Point all faults were mapped in cross section from the bottom of the cliffs. Fault traces were easy accessed. It got progressively more challenging towards the north to reach the cliff bottom. The northern part of the locality had a cliff bottom of slippery boulders and local tide schedules should be consulted prior to any visit. The cliffs were near vertical and the brittle nature of the rock inhibited climbing. Field measurements were therefore only taken at the lowest part of the cliffs. Brush and shuffle were used at areas where scree covered exposures in soft rocks.

At Snab Point the fault traces were easily accessible along strike on the tidal flat exposures and were limited at high tide. Vertical exposures at Snab Point were not high and exposures were only limited in places by vegetation cover. Vegetation and weathering of rocks on the tidal flat at times made the identification of fractures, fault and host rocks difficult, as well as attributed to a slippery surface. Brush and shuffle were used at places with high amounts of vegetation (particularly in the intertidal area).

1.3 Methods and structural nomenclature

1.3.1 Equipment and methods used

Datasets used include satellite imagery, aerial photographs, field observations, and LiDAR scan data. The geometry and orientation of the master fault planes and their associated fracture systems were first determined. Thereafter, the size of the main fault lens axes and the

orientation were measured together with similar data from the lens surfaces and their associated fracture systems.

To determine the exact location of the two field sites studied in this thesis a Garmin GPS (Global Positioning System) was used. Both localities were within GPS zone 30U using ellipsoid WGS84. Satellite and aerial maps from GoogleMaps™ (2011) were used to localise the field sites. Aerial photographs from GoogleMaps™ (2010) and Getmapping® (2010) formed the basis for large scale mapping of surface features at Snab Point (e.g. figure 3.1.1).

LiDAR (Light Detection And Ranging) data was collected by Senior Researcher at CiPR Simon Buckley from a nearby tidal flat over one of the field sites. LiDAR gathers spatially constrained point data yielding a model where the shape of the outcrop is captured. The method uses laser as a mean to scan the area of interest and following data processing, digital photographs are draped over the model (Enge et al. 2007). For this project Senior Researcher Simon Buckley handled all of the data gathering and processing providing a dataset that was ready for interpretation (Buckley 2010). The 3D geometrical model that this dataset provides is a unique tool to revisit the locality and make new measurements after fieldwork was carried out. It has also proved useful for doing observations on areas unreachable in the field.

For displaying strike and dip measurements collected in the field or from LiDAR measurements the stereographic projection program GEOrient© (Holcombe 2010) version 9.4.5 was used. The program provides the opportunity to display measurements of strike and dip of fractures and bedding and trend and plunge of lineations in several ways such as rose diagrams and equal area plots. It also provides basic statistical information of the data such as mean principal direction and mean resultant direction.

The data gathered provide a statistical database consisting of fracture frequency curves and stereographic projections of planar features (bedding, fractures), rose diagrams and dimension axes plots of the fault lenses. All planar features were measured using the right hand rule given that the dip plunges to the right of the strike. Field measurements were taken using a Brunton pocket transit precision compass. Measurements extracted from the LiDAR data tools provided by the Lime software were used.

1.3.2 Terminology and definition

The following section is a brief description of terms and nomenclature used in this study both as a basis for field measurements and in the description. Several of the features are further described in the discussion chapter.

Fault configurations

There are three principal fault types, *normal, reverse* and *strike-slip*. These are formed by different configurations of the principal stresses the maximum and minimum horizontal stress and the vertical stress (figure 1.3). During maximum vertical stress the crust is extending. When the maximum horizontal stress is largest and the minimum horizontal stress smallest the crust experiences strike-slip movement. When both horizontal stresses are larger than the vertical stress the crust is contracting (Anderson 1951, Gabrielsen 2010).

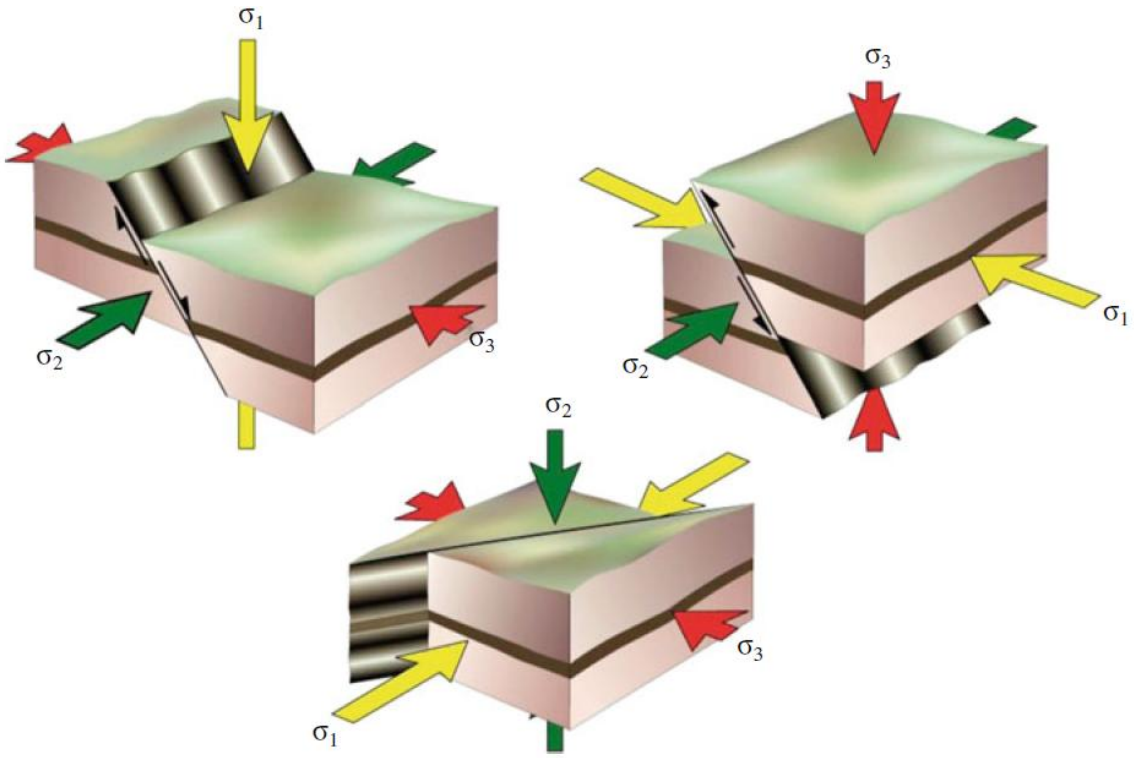

figure 1. 3 Principal stress configurations . Idealized normal fault, top left. Idealized reverse fault, top right. Idealized strike-slip fault, bottom (Fossen and Gabrielsen 2005).

Strike-slip faults might display branching in vertical section into flower structures. Where a negative flower structure is concave up with normal components along its flanks and a positive flower structure is convex up and has reverse components along its flanks (Harding 1985, Nystuen 1989).

Traditionally faults are modelled as planes (Fredman et al. 2008). In reality they are three dimensional with varying properties both along dip and strike (Caine et al. 1996, Heynekamp et al. 1999, Fredman et al. 2008, Braathen et al. 2009). The property most interesting to this study is how fluid flows along and across the fault, whether it acts as a conduit or a barrier. This is important in production of hydrocarbons and of increasing importance in groundwater exploration and production.

Fault system

A *fault system* consists of several faults that are parallel or intersect each other and are assumed to be formed during the same faulting episode (Nystuen 1989). A fault system can consist of several fault zones or comprise a horst and graben system or a graben.

Graben

A *graben* is a negative form bounded by parallel to sub parallel faults on both sides (Nystuen 1989). Consequently a *horst and graben system* is a fault system consisting of several structural low grabens separated by structurally high horsts that have parallel to sub parallel fault along their flanks assumed to be formed during the same faulting episode.

Fault zone

A *fault zone* is defined as the entire area that has experienced varying degrees of deformation due to an associated main fault within. Several faulting episodes can activate one fault thus individual deformation structures within a fault zone need not to be associated with the same fault system (Caine et al. 1996).

A fault zone consists of several components which can be classified according to their hierarchic order and where the larger order components are composed of several smaller order ones. The highest order of fault zone components is the fault core and the damage zone which is oriented parallel and more or less symmetric around the faulting centre (Figure 1.4) (Sibson 1977, Chester and Logan 1986, Caine et al. 1996, Braathen et al. 2009, Gabrielsen 2010).

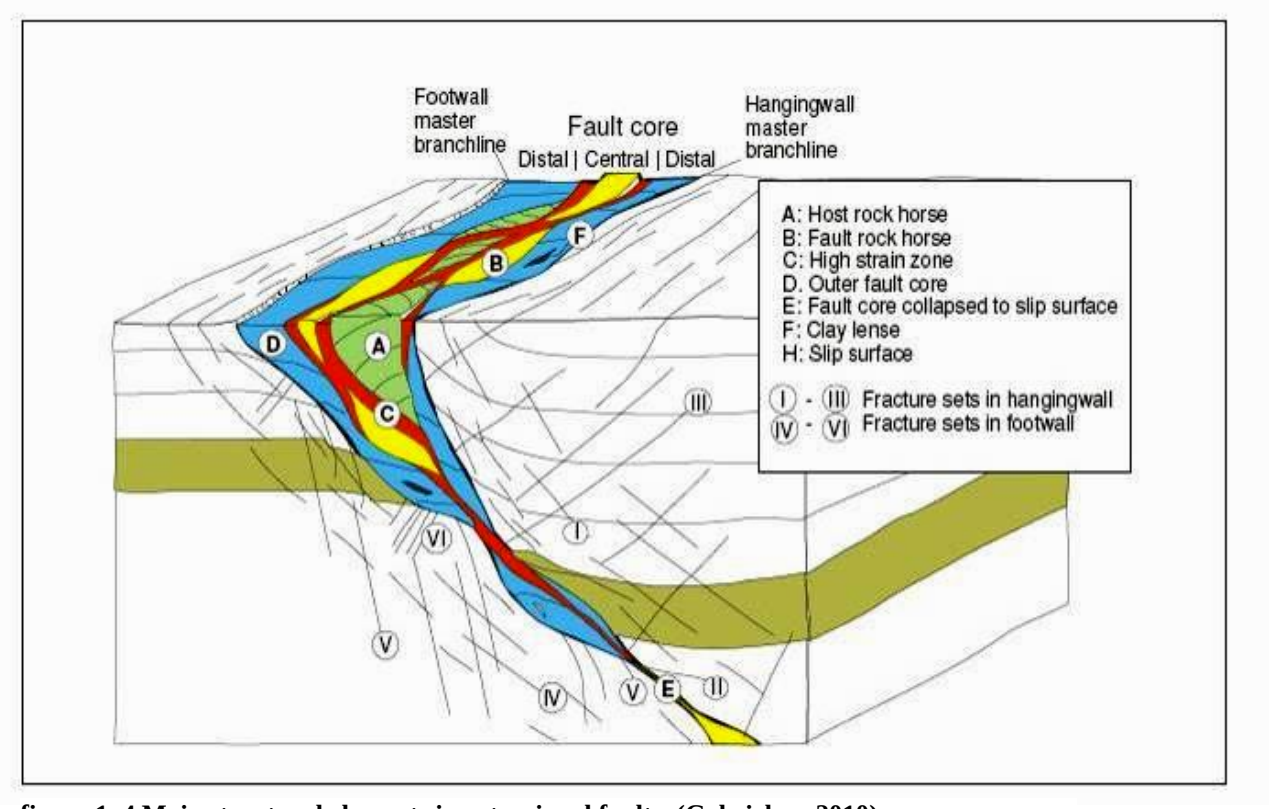

figure 1. 4 Main structural elements in extensional faults (Gabrielsen 2010)

Fractures

Fractures are used as a collective term for faults and joints where a fault has displacement as opposed to a joint (figure 1.5). Fractures, deformation bands, membranes and lenses are the most important structures that together form a fault zone (Braathen et al. 2009). Fractures and deformation bands can be found in the core as slip surfaces or in lenses as discrete structures and can also occur in the damage zone. Membranes and lenses are the major constituents of the fault core. These are therefore most crucial for fault core permeability whereas fractures and deformation bands are most important for damage zone permeability (Caine et al. 1996, Heynekamp et al. 1999, Clausen et al. 2003, Lindanger et al. 2007, Fredman et al. 2008, Braathen et al. 2009).

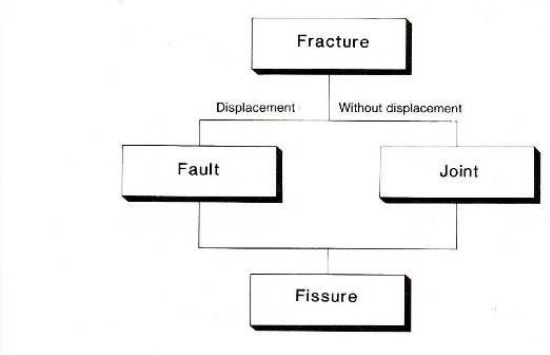

figure 1. 5 Fracture definition (Nystuen 1989)

To get a statistical overview of deformation variation across the faults, fracture frequency diagrams were made perpendicular to the fault trace. Lithological layers were followed across faults as far as possible, however where this proved difficult, layers of similar size and lithology were selected. This was done to exclude variations in fracture frequency due to bed thickness and lithology.

Fault core

Fault cores are defined as the structural, lithological and morphologic portion of a fault zone where most of the displacement has taken place (Caine et al. 1996, Heynekamp et al. 1999, Clausen et al. 2003, Lindanger et al. 2007).

Lenses

Lenses are rhombus-shaped, tectonic rock bodies with margins of slip surfaces and/or zones of concentrated shear, they may occur in isolation as *en echelon* trains or be stacked into duplexes. They consist of undeformed to heavily deformed host rock or fault rocks (Lindanger et al. 2007, Braathen et al. 2009). The original lens is characterised as a *first-order lens* and as this one splits progressively higher order lenses are formed (figure 1.6)(Lindanger et al. 2007)

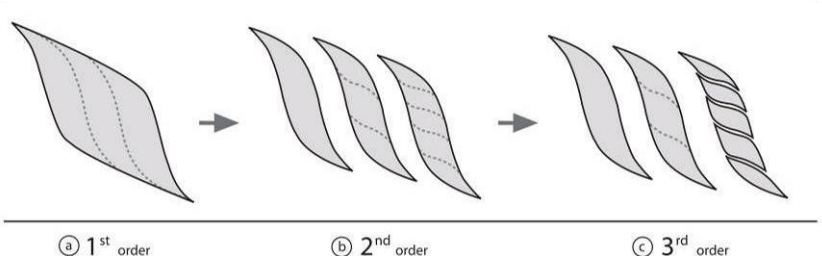

figure 1. 6 Creation of higher order lenses by splitting of existing ones (Lindanger et al. 2007)

In this thesis, as in the study of Lindanger et al. (2007), lenses are considered to be symmetrical. Their three axes, *c* length, *b* width and *a* thickness, corresponds to the axes along strike, dip and perpendicular to both strike and dip. The symmetry ensures that the ratio between these axes remains constant, as long as it is made on a section perpendicular to one of the axes. This simplifies the measurements allowing estimation of the lens' true dimensions if dimensions of half the lens are exposed. There is also no need to make measurements on the centre of the lens other than to get the maximum axes value.

Membranes

Membranes are long and thin layers of fault rock, which often define the fault core and the margin of lenses (Fredman et al. 2008, Braathen et al. 2009). . Membranes consist of fault rocks as cataclasite, breccias, sand gouge, shale gouge, sand smear or shale smear (Fredman et al. 2008, Braathen et al. 2009). Since lenses are often made up of relatively undeformed host rocks there is a large permeability contrast between membranes and lenses (Lindanger et al. 2007, Fredman et al. 2008, Braathen et al. 2009).

Fault rocks

Fault Breccia is a mainly chaotic rock that has been formed during noncohesive deformation in contrast to a *cataclasite* where cohesion has been obtained throughout deformation (figure 1.7) (Braathen et al. 2004). This gives a genetic definition to the terms. In addition to this a geometrical definition is also used in this thesis as it proved difficult in field to determine the cohesion at time of fault rock formation. Mort and Woodcock (2008) define all coarse fault rocks as breccia independent of their cohesion history. Further they divide the breccias into crackle, mosaic and chaotic breccia representing a progressively increasing degree of disaggregation of the original rock (figure 1.8) (Mort and Woodcock 2008).

Brittle ←Deformation style→ Ductile								
Frictional flow ←Dominant deformation mechanism→ Plastic flow								
Non-cohesive			Secondary cohesion		Primary cohesion			% matrix and grain-size
			Cemented HB	Indurated HB		> 50% phyllosilicate	< 50% phyllosilicate	
Hydraulic breccia (HB)	Breccia series	Proto-breccia	Cemented proto-breccia	Indurated proto-breccia	Cataclasite series: Proto-cataclasite	Proto-phyllonite	Proto-mylonite	0-50% matrix
		Breccia	Cemented breccia	Indurated breccia	Cataclasite	Phyllonite	Mylonite	50-90% matrix
		Ultra-breccia	Cemented ultra-breccia	Indurated ultra-breccia	Ultra-cataclasite	Ultra-phyllonite	Ultra-mylonite	90-100% matrix
	Gouge		Cemented gouge	Indurated gouge				Sub-microscopic matrix
			Pseudotachylyte					

Blastomylonite

figure 1. 8 Genetic classification of fault rocks based on deformation style, mechanism and cohesion during formation (Braathen et al. 2004)

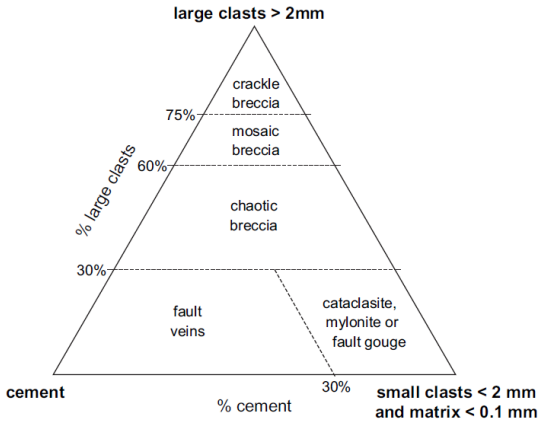

figure 1. 7 Visual classification of fault rocks (Mort and Woodcock 2008)

Damage zone

The damage zone surrounds the fault core on both hanging wall and footwall and is separated from it by fault branches (Lindanger et al. 2007). Referred to as the hanging wall and footwall master branchline (figure 1.4) (Gabrielsen 2010). The damage zone is exposed to less strain but consists of a high frequency of fractures some with drag structures surrounded by undeformed host rock (Caine et al. 1996, Clausen et al. 2003). It is wider than the core and is where most of the thickness variations of the fault zone are accommodated (Heynekamp et al. 1999).

Both the damage zone and the fault core consist of deformation derived structures that in combination form the fault zone (Braathen et al. 2009). The fault core is the most altered part of the fault zone, and consists of several fault structures and more fault rock than the damage zone (Caine et al. 1996, Clausen et al. 2003, Lindanger et al. 2007, Braathen et al. 2009). The fluid flow properties of the two zones are thus governed by different properties. The damage zone permeability is decided by its network and property of fractures, and the fault core permeability by its composition and property of fault rocks (Caine et al. 1996). The structures in the fault core and their arrangement are important in deciding whether the fault acts as a conduit or barrier to fluid flow (Caine et al. 1996). The major heterogeneity direction in a fault is perpendicular to the dip, indicating that most fault structures are oriented parallel to the fault (Fredman et al. 2008).

2. Geological Setting; the Northumberland Basin

The Northumberland Basin is situated north of Newcastle upon Tyne, England (UK), and is bounded by the Alston block to the south and by the crustally high Cheviot block to the north (figure 2.1) (Collier 1989). The basin forming faults within the Northumberland Basin show greatest displacement in late Carboniferous strata and also displace Permian strata to a lesser degree. This indicates that faulting is mainly late Carboniferous in age with some minor reactivation in late Permian and/or later (Leeder 1974, Kimbell et al. 1989). In Britain, Carboniferous basin formation such as the Northumberland Basin is believed to be originating from back-arc extension north of the Avalonia-Amorica collision that created an orogenic belt (Chadwick et al. 1995, Brenchley and Rawson 2006).

The western European chronostratigraphy often divide the carboniferous into two subsystems the older Dinantian subsystem and the younger Silesian subsystem. The transition between these two systems marks the boundary between dominantly carboniferous depositions to terrigenous clastic sedimentation. The carboniferous geological development of England is characterized in several extensional basins (such as the Northumberland and Soloway basins) by prograding deltas and coal swamps which dominated in Upper Carboniferous (Brenchley and Rawson 2006).

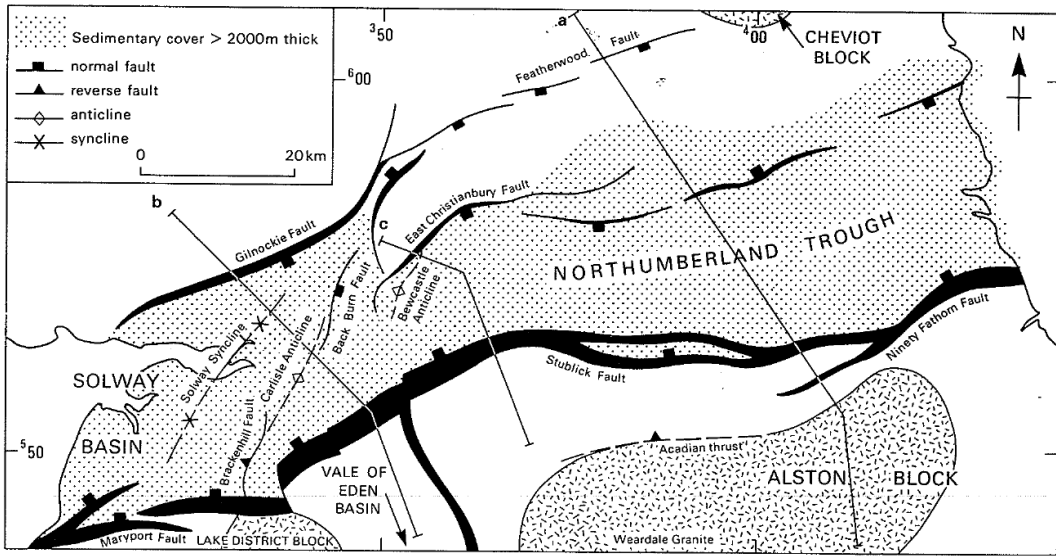

figure 2. 1 The Northumberland Basin and adjacent Soloway Basin (Chadwick et al. 1993)

In the following section the basin origin and margins will be described as well as later deformation affecting the area. Subsequently the depositional environment and their lithostratigraphy for the faulted rock will be described.

2.2 Structural style

The Northumberland Basin is asymmetric, with greatest displacement towards the south where the Ninenty Fathom Fault and The Stublick Fault form the southern boundary towards the Alston block (Kimbell et al. 1989, Chadwick et al. 1995). These are E-W to ENE-WSW trending faults where the system has a throw of between 4000m to 5000m and dip between 45^{o}-60^{o} (figure 2.2) (Chadwick et al. 1995).

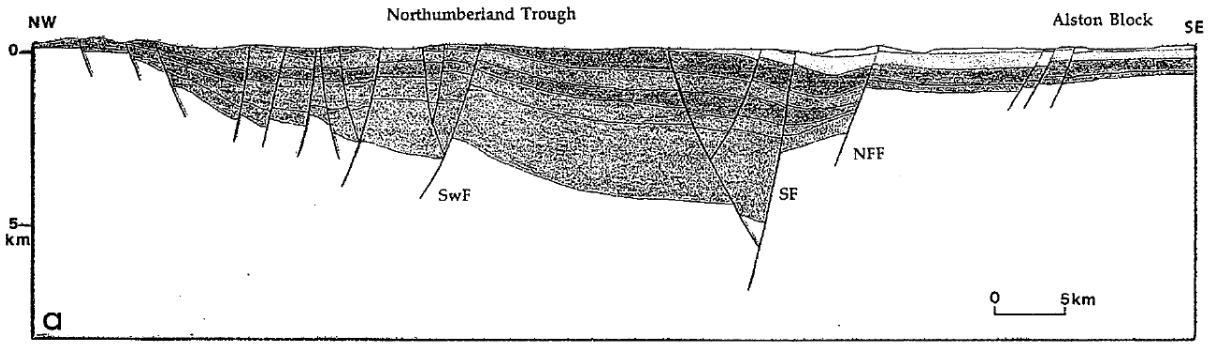

figure 2. 2 Cross section over the Northumberland Basin, illustrating the basin asymmetry. NFF-Ninenty Fathom Fault. SF-Stublick Fault. SwF Sweethope Fault (Chadwick et al. 1993)

The northern boundary of the Northumberland and Soloway basins is formed in a system of several normal faults in a E to ENE-trending axis. The faults are generally planar and dip about 60^{o} to the south with vertical offsets of about 1000m. Within the Northumberland Basin there are syn-depositional faults with vertical offset up to 300m that dip in the same direction (Chadwick et al. 1993).

In the west the Northumberland Basin is separated from the Solway basin by a N-S trending basement high, as a continuation of the Pennine ridge (Johnson 1984). Syn-depositional faulting has taken place along the western margin defining intra-basin highs in a NNE-trending direction (Chadwick et al. 1993). The eastern continuation of the Northumberland basin is the South Dogger Basin in the southern North Sea and its sepaaration from this is poorly defined. In the offshore extension of the Northumberland Basin the basin trend shifts

from NE-SW to NW-SE that is common for basins in the Southern North Sea (Ziegler 1990, Corfield et al. 1996).

The Northumberland Basin started to form in latest Devonian or earliest Tournisian times. Its asymmetry with greater thicknesses of Dinantian strata to the south indicates syn-sedimentary faulting. During early Carboniferous, Dinantian, times dip slip movement transferred from west to east as the Ninenty Fathom Fault succeeded the main movement from the Stublick fault system. The Stublick fault system is the southern basin margin at the western part ending at the western margin of the Alston Block (Kimbell et al. 1989).

The Northumberland Basin is a thick-skinned long-lived-weakness zone as it is a reactivation of the Iapetus convergence zone that is present at crustal levels (figure 2.3) (Leeder 1974, Kimbell et al. 1989). The age of this crustal zone is most likely late Devonian during the Acadian part of the Caledonian orogeny(Chadwick and Holliday 1991). This marks the boundary between Laurentia, Scottish, crust and the underthrusted Avalonia, English crust. At surface level the basin lies within the English, Avalonian, crust (Chadwick and Holliday 1991). Thus the formation of the Northumberland Basin is a reactivation of the Iapetus suture in its hanging-wall block (Kimbell et al. 1989, Chadwick and Holliday 1991).

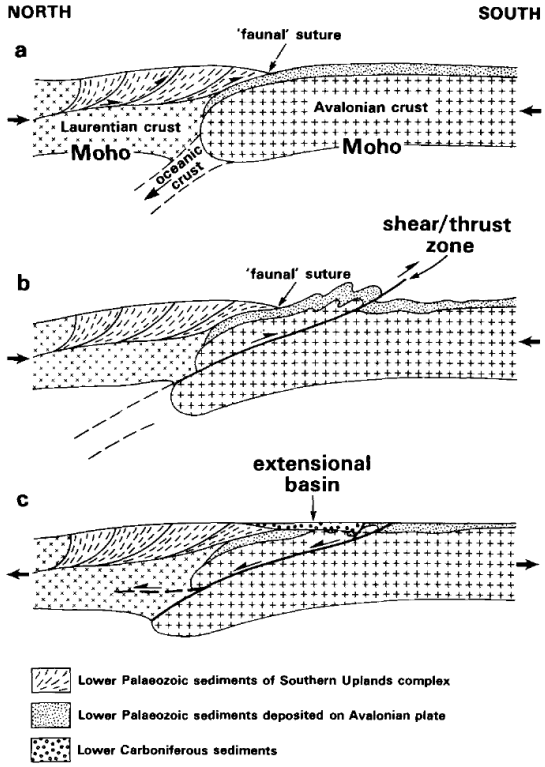

figure 2. 3 Illustration of the Iapetus convergence. A-late Silurian times continental collision. B-early Devonian times subduction of Avalonian crust. C-early Carboniferous times reactivation of shear zone, extensional sedimentary basin formed (Chadwick and Holliday 1991)

Basin formation

The Northumberland Basin was formed in a dominantly N-S extensional stress field as a reactivation of the Caledonian suture formed in the Carboniferous. The E-W trending Ninety Fathom fault created an initial half graben (Kimbell et al. 1989). The E-W trending Stublick-Ninenty Fathom fault system, has a laterally variable vertical offset between 4000 to 5000m and dips at angles between 45-60^{o}. The fault system is thin skinned, not displacing basement, dipping down to the north with an inferred dextral movement of unknown magnitude. On seismic scale the faults are dominantly planar with little tilting of the hanging wall block (Kimbell et al. 1989, Chadwick et al. 1993). Beneath both the Northumberland Trough and adjacent horsts the Moho remains at a constant depth of about 30 km (Kimbell et al. 1989).

The prevailing deformation process in early Dinantian times was rapid subsidence confined to the main through forming faults in the Stublick-Ninenty Fathom Fault system. The following subsidence included a more regional normal faulting with uniform rates representing thermal subsidence (figure 2.4) (Kimbell et al. 1989). The active rifting ceased in the early Namurian whereas thermal subsidence continued into Westphalian times. Facies patterns in the Coal Measures, southern Northumberland, indicate normal reactivation of both the Ninety Fathom fault in the south and the intrabasinal Hartley Station fault suite in the north (Collier 1989).

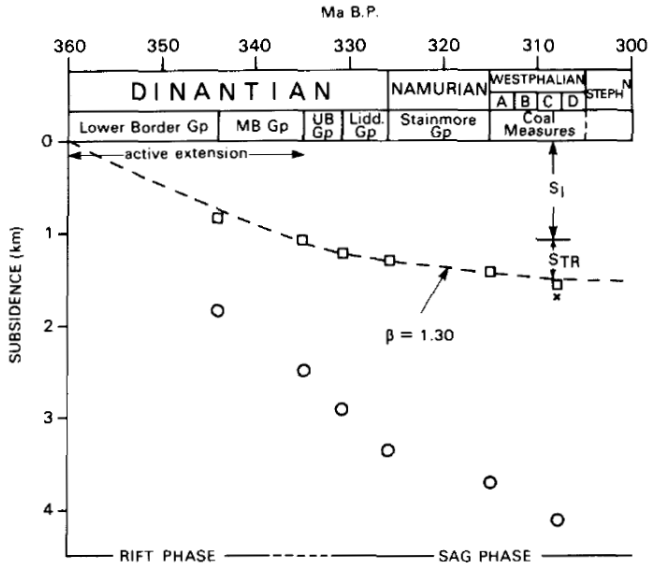

figure 2. 4 Basin subsidence plot for the Northumberland basin. Dashed line show modelled subsidence. S1-active extension. Str- thermal subsidence (Kimbell et al. 1989)

Variscan inversion

Several authors (Collier 1989, Kimbell et al. 1989, Chadwick et al. 1993) argue that the Variscan orogeny, between 311Ma-295Ma, caused a tectonic inversion of the

Northumberland Basin. The main phase of inversion in the Northumberland Basin is younger than 300 Ma (Westphalian) (Kimbell et al. 1989). The Northumberland Basin is in the foreland arc of the orogeny where Avalonia in the north collided with Gondwana to the south. This created thrust faults with a N and NE strike and folds in a NE-SW to NNW-SSE orientation in the north and west of the basin. The absence of thrust faulting in southern and eastern Northumberland suggests that the entire basin (or at least the upper part) may have been transported westwards as a coherent allochthon (Collier 1989). The present day surface breaching Stublick and Ninenty Fathom faults, marking the southern basin boundary, are at many places related to Variscan and later inversion and transpression and do not correspond everywhere to the earlier syn-depositional normal faults (Kimbell et al. 1989). Compared to the nearby Soloway Basin the Northumberland Basin shows less evidence of inversion whereas in the Soloway Basin large scale folding structures are present (Chadwick et al. 1993, Chadwick et al. 1995).

Whin Sill

Towards the end of the Variscan inversion the Whin Sill Complex was emplaced within the system in late Carboniferous to early Permian(Liss et al. 2004). The youngest rocks intruded by this complex are of Duckmantian age (Middle Coal Measures strata). K-Ar analyses on the associated Alnwick Sill emplaced within the Northumberland Basin is of an age ranging between 269 (+/-18Ma) to 316 (+/-13Ma), a late Carboniferous to middle Permian intrusion. Paleomagnetic results might suggest that the Alnwick Sill represents a possible Permian intrusion and a resumption of igneous activity (Liss et al. 2004). Overburden at the time of emplacement of the Whin Sill was between 0,5 and 1km (Francis 1982). There remains disagreement on whether the Whin Sill intrusions occurred during compression or is related to a separate extensional event (Chadwick et al. 1995).

Alternative theory for Late Carboniferous tectonic events

De Paola et al. (2005b) have a different approach to the Late Carboniferous-Early Permian structural development in the area. They propose that the area was not affected by Variscan inversion but instead affected by a partitioned transtension due to a N-S extension related to emplacement of the Whin Sill complex. This simplifies the sequence of events for the Northumberland Basin to a single phase of dextral oblique extension lasting for about 15 Ma (De Paola et al. 2005b), as opposed to two events (Variscan inversion and Whin Sill

extension). The study is based on fieldwork and identifies one extension dominated domain in the south of the Northumberland-Soloway Basin and one wrench dominated domain in the northern part of the basin and in the Cheviot block. The extension dominated domain shows presence of E-W to NNE-SSW extensional faults whilst the wrench dominated domain has ENE-trending dextral faults as well as associated ESE-trending sinistral faults. By combining the two basin domains the regional transport direction for the Northumberland Basin during the Late Carboniferous-Early Permian development is NNE (De Paola et al. 2005b). Seismic data presented by Chadwick et al. (1993) show inversion structures in the form of reverse faults in the southern end of the Northumberland Basin. This is not discussed by De Paola et al. (2005b) who solely considers the surface structures. Their main argument against the Variscan model is the geometrical difference in the E-W shortening of the basin and the NNW direction of the Variscan orogeny in Southern Britain They also point out the contradiction of crustal shortening due to the inversion contemporaneous with lithospheric extension that typically is related to intrusions such as the Whin Sill.

Post Carboniferous development

Later tectonic incidents that might have affected the basin are the uplift of the North Sea Dome in middle Jurassic times creating compression and extension in connection with subsidence of the North sea basin and the opening of the Atlantic Basin in the Lower Cretaceous (Chadwick et al. 1995, Austin et al. 2009). Faulting of Permian strata is known (e.g. at Cullercoats (Collier 1989, De Paola et al. 2005a)) and is suggested to represent early rifting stages of the North Sea Basin in a NE-SW extension (Ziegler 1990, Chadwick and Holliday 1991, Austin et al. 2009). The reactivation of the system is characterized by one set of dextral ENE strike slip faults, one set of ESE sinistral strike-slip faults and N-S trending reverse faults. These structures often cross cut or reactivate late Carboniferous structures (De Paola et al. 2005b). Based on the cross cutting of late Carboniferous structures dextral displacements is calculated to be 10-100m (Collier 1989).

2.3 Stratigraphy and depositional history

The Northumberland Basin saw deposition of sediments throughout the Carboniferous simultaneous with progressively more faulting to the south, creating an asymmetric basin

infill (figure 2.2). The Lower Carboniferous fill of the basin is therefore thickest (up to 4000m) adjacent to the southern margin of the basin (Kimbell et al. 1989).

During most of the basins history the main sediment source, the Caledonian Orogens, was to the north and east of the basin whereas marine influence increased towards the south and west (Leeder 1974, Johnson 1984).

Sedimentary infill commenced at the start of Carboniferous, Dinantian times, with fluvial and lacustrine coastal plain deposits represented by the Lower and Middle Border Group (figure 2.5). The tectonic control was the largest during deposition of these groups creating cyclic sea level fluctuations and a progressive marine transgression. Fluvial systems built out from the east during low sea level, as sea level rose carbonates and lacustrine tidal flat and sub tidal sedimentation dominated (Jones 1968, Chadwick et al. 1993). The Middle Border Group strata tend to, as opposed to the Lower Border Group strata, thicken towards the basin centre and not to the southern margin. This demonstrates the gradual shift in control on sedimentation from active subsidence to thermal subsidence (Chadwick et al. 1993).

By the end of the Dinantian repeated fluctuations from transgression to regression occurred (Johnson 1984, Chadwick et al. 1993). The Upper Border Group had a stronger marine influence from the west and southwest compared to the underlying Middle Border Group. The overlying Liddesdale and Alston Groups (figure 2.5) have an evidently cyclic appearance called the Yoredale cyclothems with repeated sequences of limestone, shale, sandstone and coal (Chadwick et al. 1993). In earliest Silesian age, the early Namurian, the basin experienced regression, represented by the Stanimore Group, with delta progradation and limestone bands becoming progressively rare up-sequence (figure 2.5) (Johnson 1984).

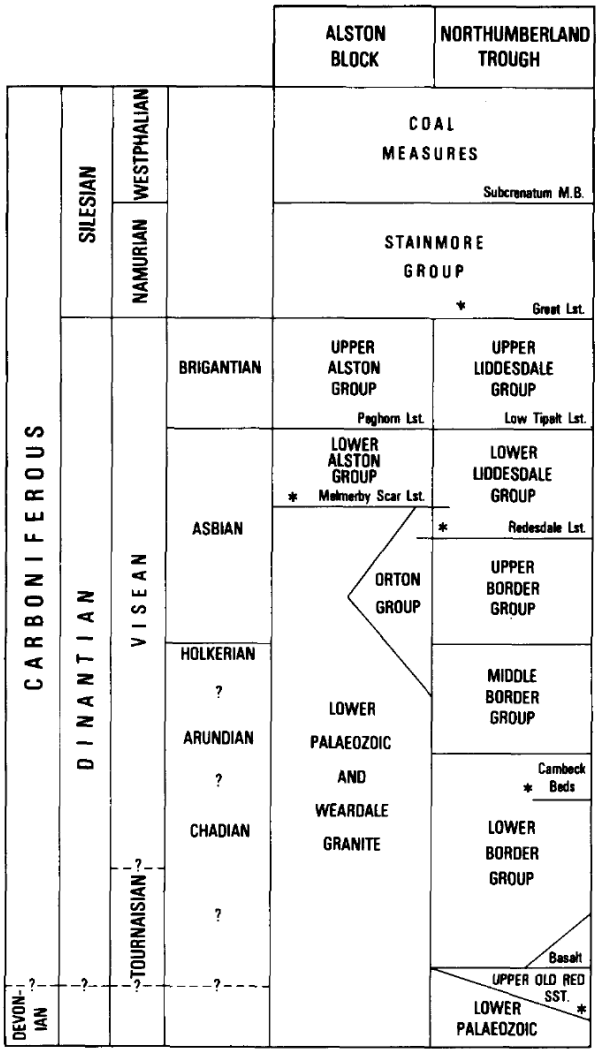

figure 2. 5 Carboniferous sedimentation of northeast England (Kimbell et al. 1989)

In Westphalian times the depositional environment became progressively shallower and was dominated by upper delta plain sedimentation, this formed the Coal Measures strata (figure 2.5). Forest swamps were covering large areas resulting in peat deposition (Johnson 1984, Chadwick et al. 1993). The measured and described faults in this thesis are within these strata where coal is interbedded with sand, silt and mud of fluvio-deltaic origin. The structural control on sedimentation seems to have been thermal subsidence combined with subsidence due to compaction (Chadwick et al. 1995).

Large scale liquefaction structures are present within the basin as a product of the depositional setting. The fluvial or deltaic origin of many of the sedimentary rocks induced faults from processes such as levee collapse or delta front faults in addition to thermal subsidence structures (Collier 1989).

Through vitrinite reflectivity data it is suggested that the Northumberland Basin reached maximum burial during the late Carboniferous from thermal subsidence (figure 2.4) and received limited Mesozoic burial (Fraser and Gawthorpe 1990, Chadwick et al. 1995). Deposition came to an end in late Carboniferous. During early Permian the basin emerged possibly correlated to an eustatic sea level lowering or a Variscan uplift, where it became part of the Grampian High, followed by erosion of the underlying strata (Johnson 1984, Ziegler 1990, Corfield et al. 1996, Austin et al. 2009). Permian deposition in the Northumberland Basin has an uncertain original thickness (Smith 1970, Chadwick et al. 1995). The oldest Permian deposits found onshore in the Northumberland Basin are the Yellow Sands, for example those found at Cullersoats close to the Ninenty Fathom Fault (Collier 1989). Offshore borehole data shows sediments of older Permian age up to Blyth (Smith 1970). There were post-Carboniferous deposits in the nearby regions with a thickness of up to 2000m, such as within the Soloway Basin (Chadwick et al. 1995) At the end of the Permian period and in the beginning of the Triassic northern England went through a transition from marine to continental depositional environment resulting in an erosion of Permian sediments (Chadwick et al. 1995, Austin et al. 2009).

2.4 Stratigraphy for rocks affected by faulting studied in this thesis

The studied areas both consist of Coal Measure strata deposited during the Duckmantian stage of Westphalian B times (Kimbell et al. 1989). These deposits were mainly fluvio-deltaic facies (Collier 1989). The faults of this study are situated within fluvial sand bodies. The sandstones at Crag Point have been studied by several authors such as Jones (1968), Land (1974), Haszeldine (1984) and O'Mara and Turner (1999). In the following section first the Westphalian sedimentation will be described in general establishing the common depositional features for Crag and Snab Point. Thereafter the affected stratigraphy at Crag Point will be described in further detail.

Westphalian B sedimentation in the studied area was a result of deposition in fresh water lakes fed by small deltas. The lakes were possibly surrounded by swamps and peat bogs. They were a few tens of km's across and most of the time free from clastic input (Haszeldine 1984). The channels feeding these lakes were primarily low gradient and draining from the north (Haszeldine 1984, Fraser and Gawthorpe 1990, O'Mara and Turner 1999).

The faults exposed at Crag Point are cutting the Upper and Lower Craig Point Sandstone (Jones 1968, Land et al. 1974) which is a continuation of the Seaton Sluice Sandstone (figure 2.6) (Land et al. 1974, O'Mara and Turner 1999) . That in turn overlies alluvial plain deposits including the Five Quarter Seam (Jones 1968). The section visible in the cliffs below the Five Quarter Seam consists of siltstone with sandy bands. Above the Five Quarter Seam the succession is composed of shale with sandy bands overlain by clay (Jones 1968). The succession below the sandstones represents coastal alluvial plain sedimentation whereas the sandstones represent river systems.

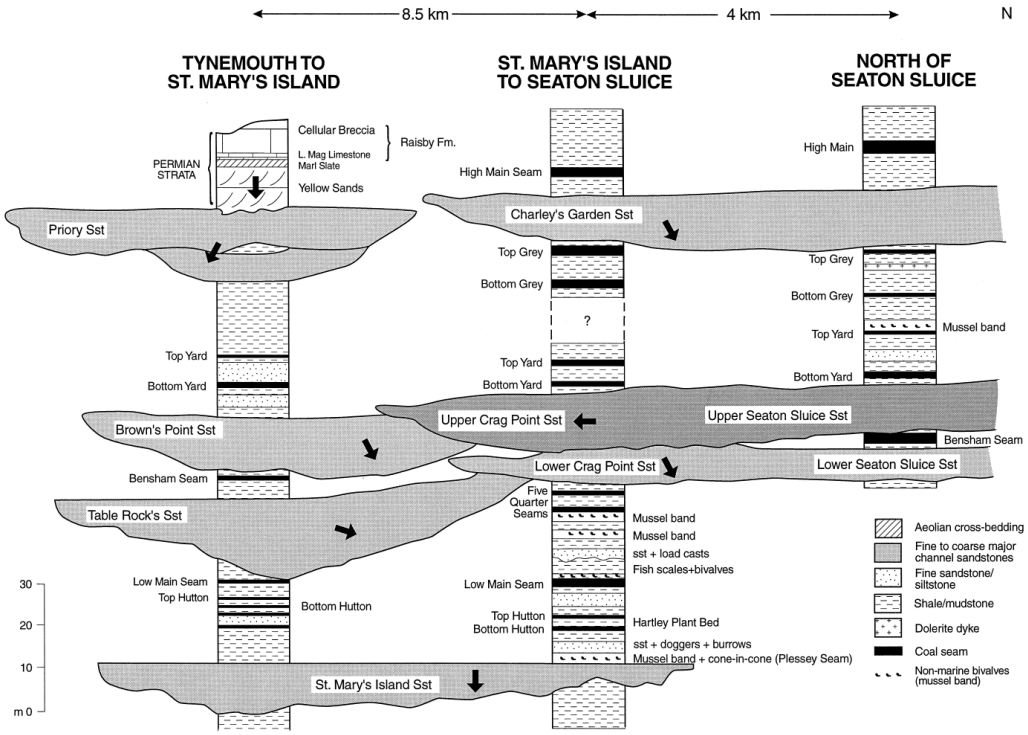

figure 2. 6 Coal Measure stratigraphy between Tynemouth and Seaton Sluice based on data from Jones (1968) and Land (1974) Displaying the Crag Point sandstones placement within the succession . The arrows indicate paleoflow directions. (O'Mara and Turner 1999)

The two sandstones at Crag Point have varying properties in their appearance. The description of their characteristics is here mainly based on O'Mara and Turner (1999). The upper sandstone, the Upper Seaton Sluice and Crag Point Sandstone, is different to other sandstones in the Coal Measures succession drained from the east (figure 2.6). It erodes into the underlying Bensham Seam which at Crag Point is completely eroded and the boundary between the upper and lower sandstone is marked by a conglomerate with coal fragments (Jones 1968, O'Mara and Turner 1999). The sandstone extends over an area of 100 km^2 and is about 15 m thick (O'Mara and Turner 1999). It consists of coarse poorly sorted sheet sands deposited by a braided river complex (Land et al. 1974, O'Mara and Turner 1999). The lower

part of the sandstone, the Lower Seaton Sluice and Crag Point sandstones, is more layered and sorted it is finer grained and more cross stratified compared to the upper part. It has paleoflow directions from NNW similar to the other sandstones in the succession and has an conglomeratic base erosive into the underlying shale beds (Jones 1968, O'Mara and Turner 1999).

3 Results

This chapter provides an overview and descriptional scheme for each locality.

Of the two fault zones studied in detail within the Northumberland Basin, Snab Point is the northernmost field site. One of the faults studied here was part of a study comparing faults with smear (Faerseth 2006). The other faults studied at Snab Point are all subordinate structures belonging to the hanging wall of the master fault described by Færseth (2006), which is characterized by a normal vertical offset of 21 m down to the NW. The other faults present have not previously been described in detail in the literature. This is perhaps due to their minor importance for the regional development of the basin. All faults studied affect Pennine Coal Measures Group strata deposited in Westphalian (late Carboniferous) times. The fault zone mainly described in the present work is the northernmost fault at the site (here referred to as fault 1). It has a normal offset described to be 10 m to the SE (pers.commFærsteth 2010).

The fault described by Færseth in 2006 (here referred to as fault 3) is the southernmost fault, while between this and the main fault there is a subsidiary fault (fault 2). Fault 1 and 2 have mainly been mapped along strike, whereas fault 3 has been mapped in cross-sectional view. The faults at Snab Point will be described according to variations in geometry, core width, fracture systems, presence of mineralization, type of fault rocks and lenses. Each fault and fault segment will be described separately. All these different properties make it easy to compare and organise the faults and fault segments.

The main fault studied at Crag Point was described by Jones (1968) and illustrated by Land (1974) as a description of the geology along the coast section. After these descriptions took place cliff erosion has altered the exposure. The faults affect Pennine Middle Coal Measures Group strata. South of the main fault the section consists of interbedded sand and silt with coal seams in between, deposited as upper delta plain sedimentation. Within these sediments a graben has been described south of the main fault. Cliffs on the north side of the main fault consist of two sandstones, the upper and lower Crag Point Sandstones representing major channels (Jones 1968, O'Mara and Turner 1999). In the cliffs north of the main fault a ~100m wide horst and graben system is described.

The main fault at Crag Point has a normal vertical offset of about 11m to the north (Jones 1968). The fault surface visible today is markedly different to the one described in 1968 and it is not currently possible to determine vertical offset of the fault as a talus slope now covers the cliff base, where Jones described the Five-Quarter Seam to appear.

In the following chapter the chosen main faults of each locality are described first, followed by description of subsidiary structures. It is important to stress that the term *main fault* is a relative term and is given to one fault at each locality based on their importance within the presented window of observation and the emphasis they have been given during fieldwork. The faults regarded as master faults in this study are at both localities subsidiary faults to larger faults on their hanging wall side. Structural maps, cross-sections and statistical data associated with each locality will be presented and described.

3.1 Locality Snab Point

The faults juxtapose fluvial sandstone of the Upper Coal Measures stratigraphic unit of Westphalian (late Carboniferous) age. The northernmost fault, fault 1 (figure 3.1.3), has a normal vertical offset of about 10m to the SE (pers comm. Færseth 2010). The relief of the exposure at Snab Point is therefore less than the vertical offset across the fault on either side of the tidal flat and as such it has not been possible to determine the vertical offset inside the exposure. However the exposed cliffs on either side of the fault give a minimum vertical offset of 5-7m. The more precise vertical offset of 10m has been given by others; Færseth.

The tidal flat at Snab Point displays lineaments representing surface traces of fractures and rock boundaries (figure 3.1.1). Fault traces were mapped in the field together with associated fractures. This was then compared to the aerial photograph (figure 3.1.1) enabling plotting of additional fracture networks and continuation of fault traces (figure 3.1.2). Figure 3.1.2 is a map of structural and topographic features of the Snab Point locality placing individual fault segments into a larger context.

Figure 3 1.1 Aerial Photograph Snab Point (Getmapping© 2010)

Figure 3 1.2 Snab Point tidal flat, brown thick line marking path from parking lot. The parts marked in purple and yellow are lenses mapped in field. The red lines mark master branchlines. The green lines mark fractures. Large scale fractures and the unfilled master

The faults at Snab Point are well exposed for about 100m along strike in the horizontal dimension on the tidal flat as well as in a 3m vertical cross sectional view in the cliffs. This gives an excellent 3D overview of the master fault and subsidiary faults. Access to the faults was determined by the tides. The seafront at low tide was a couple of meters beyond Segment 1.2. At high tide the seafront were situated about where Segment 1.1 is branching (Figure 3.1.3). This set a control on pace and timing of the fieldwork.

For simplicity the main fault, fault 1, has been subdivided into two subparallel segments which are described successively. The segments are soft linked via a fault-ramp (bridge) in a left stepping fashion. Segment 1.1 was mapped for 43m in an ENE direction from the cliff escarpment. Segment 1.2 can be traced over a distance of 40m in a NE direction to the low tide mark (figure 3.1.3). There are two vertical exposures of fault 1 further inland from the tidal flat displaying what probably is the footwall master branchline exposure 0.1 and 0.2.

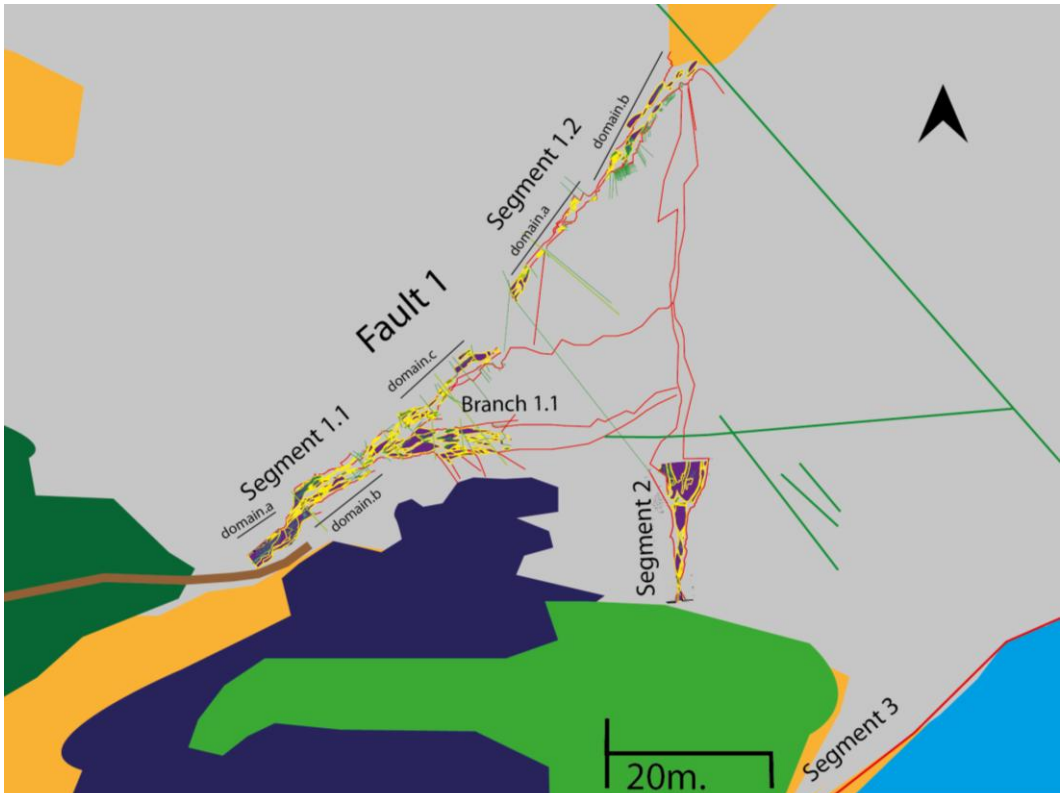

Figure 3.1.3 Snab Point close up with naming and numbering of different fault segments present at the tidal flat.

3.1.1Segment 1.1 description

Segment 1.1 can be traced out along the tidal flat where it has anastomising geometry. Close to the cliff the core is represented by a 2m high lens (domain *a*). The cliff offers a good exposure of the of the master fault footwall. Several amalgamated channel bodies are present in the footwall (figure 3.1.4) that are cut by fault 1 and the lens defining domain *a*. The channel surfaces indicate an easterly flow direction and contain several plant fossils

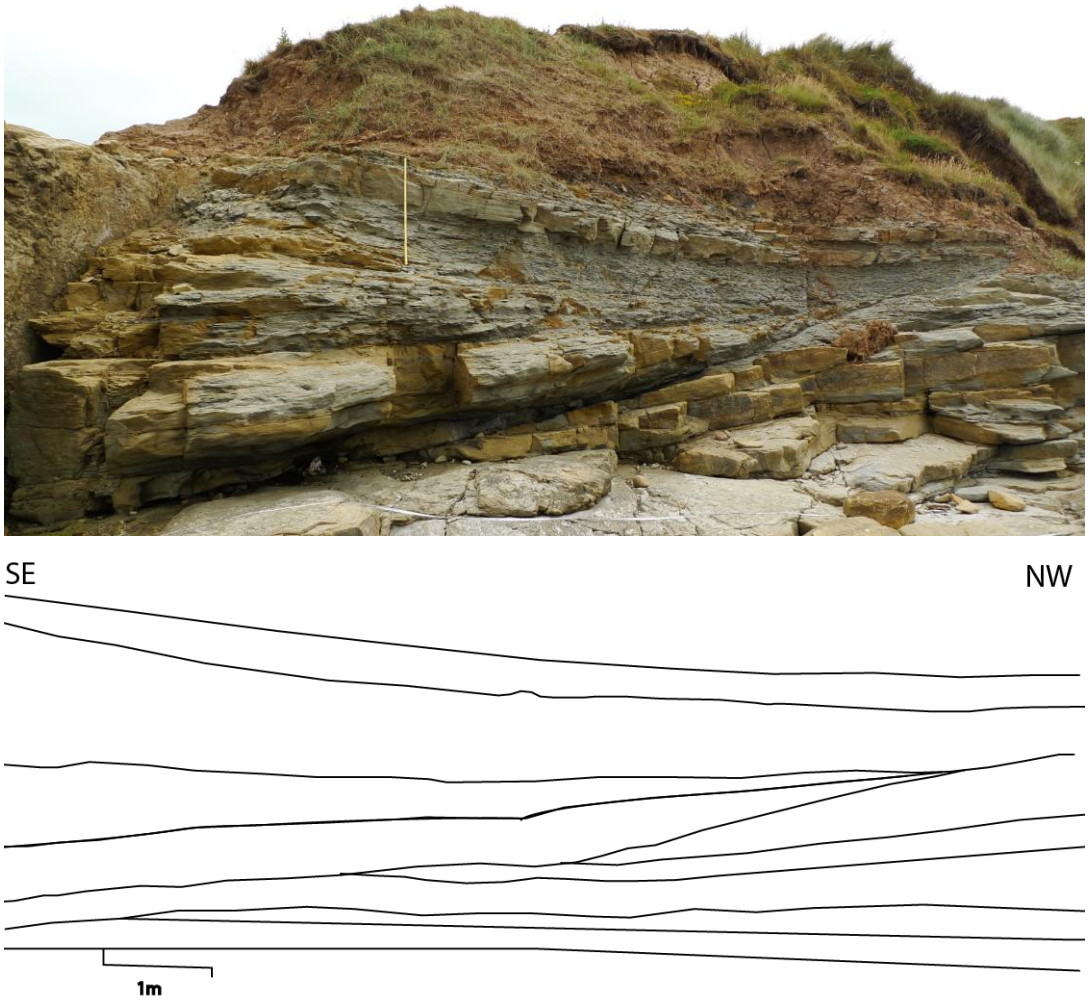

Figure 3.1.4 Upper picture and lower sketch of the same section. Segment 1.1 footwall cliff showing fluvial bedding (see meterstick for scale)

Segment 1.1 has an overall orientation of 66/79, ENE trending (Figure 3.1.5.a), along the original fault trace. Measurements show that the hanging wall master branchline is generally steeper, (85^{o} figure 3.5.c), than that of the footwall master branchline, (77^{o} figure 3.5.b). It is a very steep fault, and both the hanging wall and the footwall show examples of measurements that are over steepened in relation to a normal offset to the SE. The trend is uniform in its direction along the mapped section. Mapping of segment 1.1 from aerial photography revealed a lineament possibly representing the segments continuation in a slightly more easterly direction than that observed in the field (figure 3.1.1).

Approximately 22m from the cliffs, segment 1.1 splits with one branch (branch 1.1) routed south into the hanging wall. Segment 1.1 can be further subdivided into domain *b* close to the cliff and domain *c* which is the branch continuing along the original fault trace to the east.

The core narrows in domain *c*. Branch 1.1 has been mapped for 16 m south from its branch point as shown by figure 3.1.3 shows. At this point the fault borders are less clear as deformation is spread out over a wider area. Unfortunately it was impossible to determine the amount of vertical offset accommodated on branch 1.1.

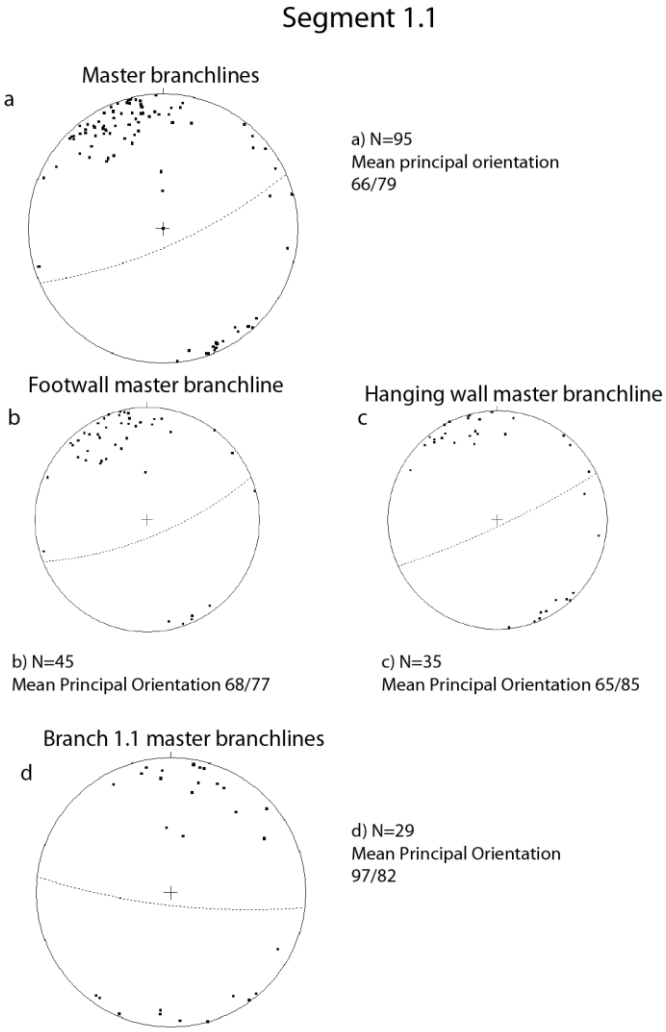

Figure 3.1.5 Stereographic projections from master branchline measurements along segment 1.1 and branch 1.1.
a) Measurements from the segment 1.1s master branchline s
b) and c) displays the splitting of a) into footwall master branchline measurements (b) and hanging wall master branchline measurements (c).
d) Measurements from branch 1.1s master branchlines

Branch 1.1 is directed into the hanging wall with an easterly trending orientation of 97/82 (Figure 3.1.5.d). In an extensional system this indicates a vertical offset down to the south with a southern hanging wall and a northern footwall, however no stratigraphic observations were made to support this. Branch 1.1 is a very steep fault branch and a large proportion of measurements show branchlines trending the opposite direction (i.e. west dipping to the north).

The core of branch 1.1 varies between 3-4m in width along strike (figure 3.1.6 and appendix B). In this domain it is especially clear that the potential master branchlines often follow fractures that are not parallel to fault trend particularly in the hanging wall side. The core of segment 1.1 varies between 3,3m and 0,2m along its strike, being situated 11m and 36m from the coastal cliff respectively. The average width of segment 1.1 is approximately 1,5m (figure 3.1.6 and appendix B).

Domain *b* has a core width variation between 3,3m and 0,8m along its strike, with the thinnest section being situated 18m from the coastal cliff. In some places it is hard to determine where the fault core ends across strike. Several zones mark different styles of deformation such as intensity of lens networks. Domain *c* has core width variation between 2,2m and 0,2 m along strike, the thickest section being situated 42m from the coastal cliff. The thickest section has been recorded where there are two potential hanging wall master branchlines present (figure 3.1.6 and appendix B). The potential hanging wall master branchlines are given by topographical variations marking difference in intensity of deformation. The area between the two potential master branchlines is more deformed than the hanging wall damage zone, by that it later has subsequently been eroded to a lower level.

Figure 3.1.6 Mapped master branchlines along segment 1.1. Horizontal section. Note that the fault core is widest where it is branching and most narrow in segment *c*.

Lenses

The core consists of lenses bounded by zones that at recent times have been eroded. This gives a fault core that is distinguished by its negative topography due to erosion, indicating that the core is mechanically weaker than the unfaulted rocks.

Lenses mainly consist of relatively undeformed rocks derived from the damage zones. Most of the lenses appear to be made up of similar sandstone. However two lenses both close to the branching of segment 1.1 contain parts of darker more coarse grained sandstone.

The lens in domain *a* is the largest measured as having a *b*-axis over 10m and an *a*-axis of 2,3m. This lens consists of relatively undeformed rocks similar to those in the hanging wall. Along the edges on both sides there are breccias present (figure 3.1.7), this is also the case on the edges of some of the smaller lenses present in domain *b* (figure 3.1.8).

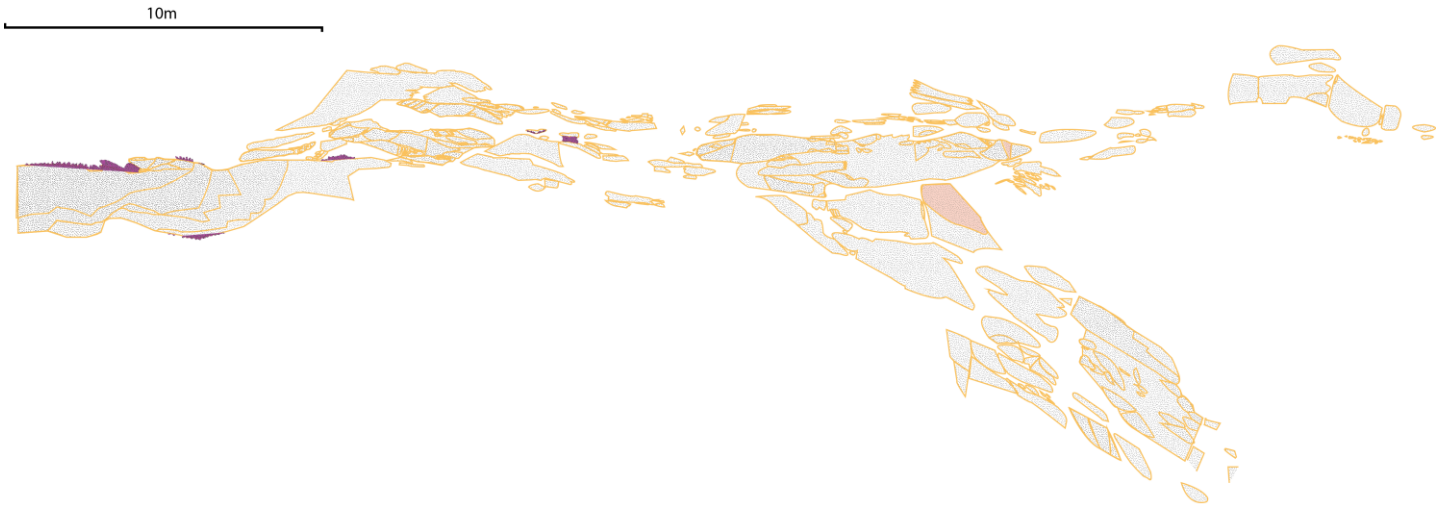

Figure 3.1.7 Horizontal section. Lenses (with yellow borders) and breccias (purple) in Segment 1.1. Note that the majority of large lenses are placed near the junction between segment 1.1 and branch 1.1. The large lenses are placed where the core is wide (appendix B). Most of the lenses are directed in y –direction. (see appendix B for larger figure)

Figure 3.1.8 a) Breccias north side domain *a*
b) Breccias north side domain *a*
(20cm meterstick for scale)

In segment 1.1 domain *c* is the area with the least and the smallest lenses. Close to the branching part there are several large lenses, there are also a high density of lenses in domain *b*. In domain *b* the lenses show an increasing amount of symmetry from the hanging wall towards the core centre (figure 3.1.8). 7 out of 10 large lenses within segment 1.1 have several smaller lenses within. Width(strike)-thickness relations (*b*:*a*) for recorded lenses in segment 1.1, including branch 1.1, are given in figure 3.1.9. Thicknesses vary from 0,03m to 2,60m and widths vary between 0,10m to 10,20m. The best fitted regression line is the power law trend with a confidence factor of 0,58, indicating a strong variation in the dataset. Using the power equation we get an average *b*:*a* ratio of 5,6:1.

The orientation of *b*-axes from 42 of the lenses along segment1.1 gives an ENE trend similar to that from the master branchlines (66/79) with 16,7% of the data within a range of 65^{o}-70^{o}E (figure 3.1.9). 12% of the lens data for segment 1.1 show a somewhat different trend ranging between 45^{o}-50^{o}NE. In general all but one SW trending lens were oriented in an E-NE direction. Along branch1.1 35,7% of the *b*-axes directions show an easterly trend similar to the master branchline (97/82) directions with 14 data-points within a range of 90^{o}-95^{o}E (figure 3.9). 3 of the data points are ranging between 100^{o}-105^{o}E and 2 of the data points are ranging between 75^{o}-80^{o}E. The majority of lenses measured are trending in y direction (figure 3.1.5).

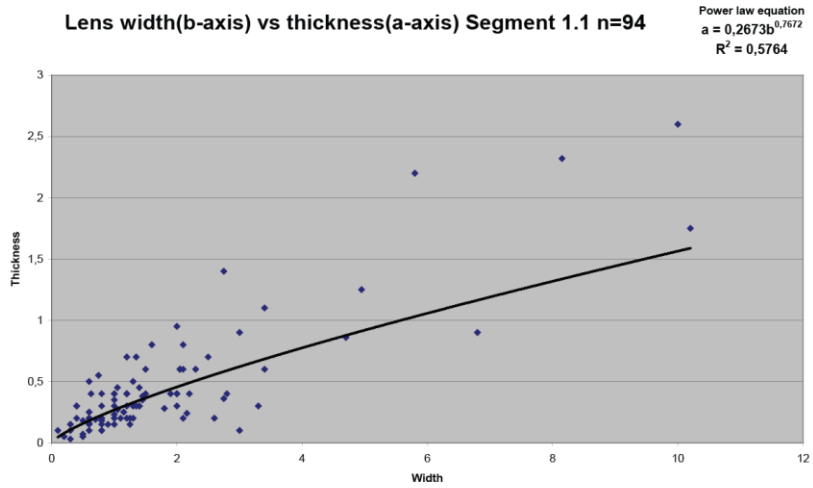

Power law regression line gives best fit b:a=5,58:1

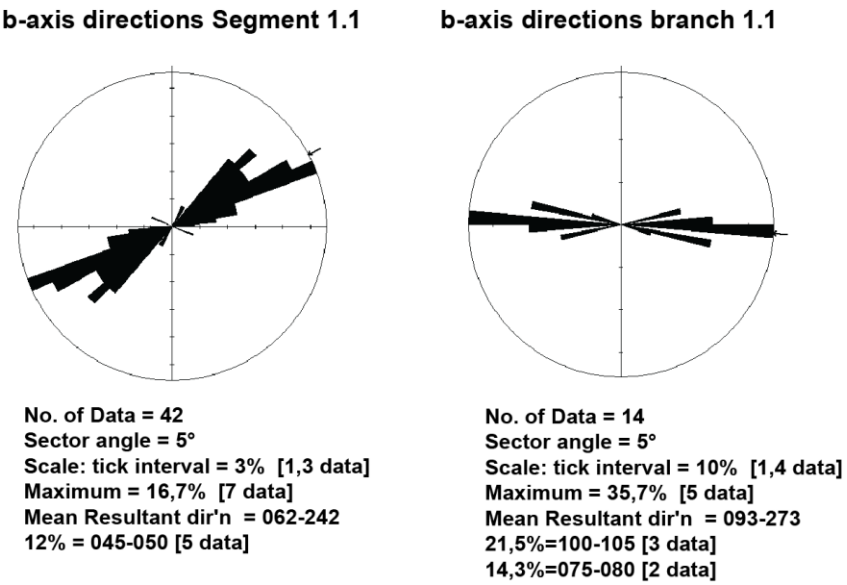

Figure 3.1.9 Lens statistics for segment 1.1 displaying relative lens dimensions and *b*-axes directions for segment 1.1 and branch 1.1 separately

Fracture systems

There are fractures present both in the damage zones and in the lenses (figure 3.1.10 figure 3.1.11 and figure 3.1.12). The core frequently expands or contracts in a stepwise manner following fracture systems with a high angle to the fault trace. In branch 1.1 decrease of deformation intensity was primarily accommodated by fracture networks along the southern core edge. These fractures had directions varying from an ESE-WNW to a SE-NW direction (figure 3.1.10).

Three fracture frequency plots were made across segment 1.1 (Figure 3.10 and 3.11). From figure 3.11 we can see an increasing amount of fractures away from the cliff. Both the frequency plot made 10m from the cliff and the one made 34m away show a trend of increasing fracture frequency towards the core from the footwall side. None of the plots show any clear trend for the hanging wall. Two fracture frequency plots were made perpendicular to branch 1.1 (Figure 3.10 and 3.12). Both diagrams show that the fracture frequency within the core is higher than the one outside. The area south of branch 1.1 had limited accessibility as most of it was covered with water.

Figure 3 10 Horizontal section. Segment 1.1 Green lines mark fractures, pink lines deformation bands and blue lines where fracture frequency plots has been made (see appendix B for a larger figure)

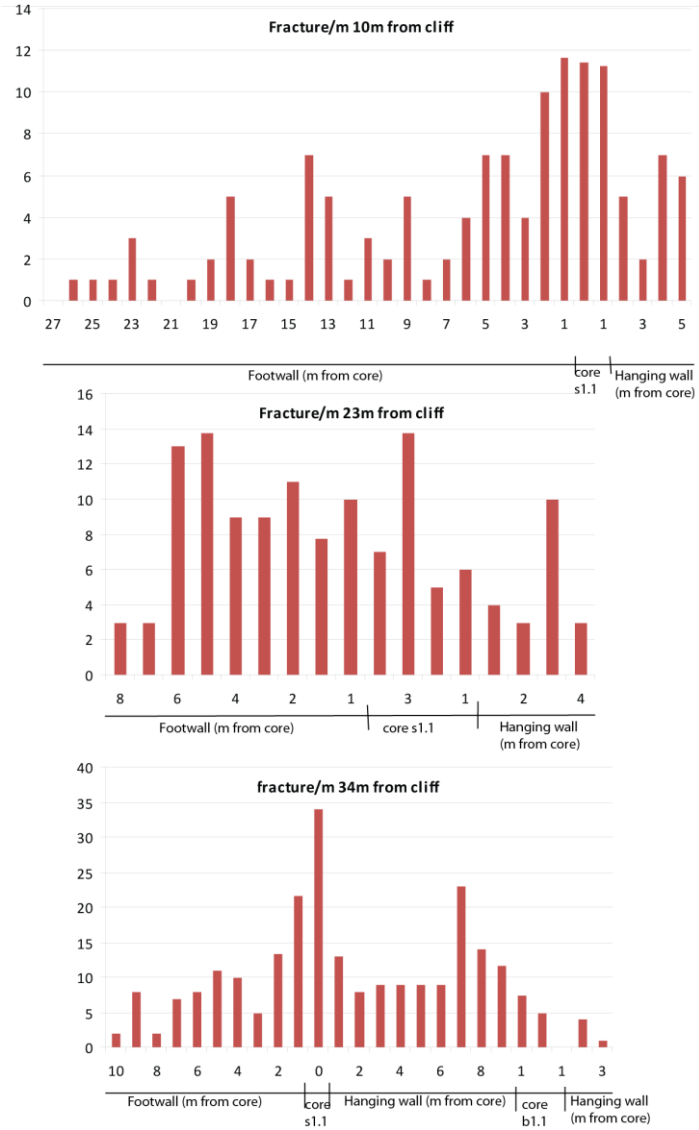

Figure 3.1.11 Fracture frequency plots perpendicular to segment 1.1 (see blue lines in figure 3.10 for exact location)

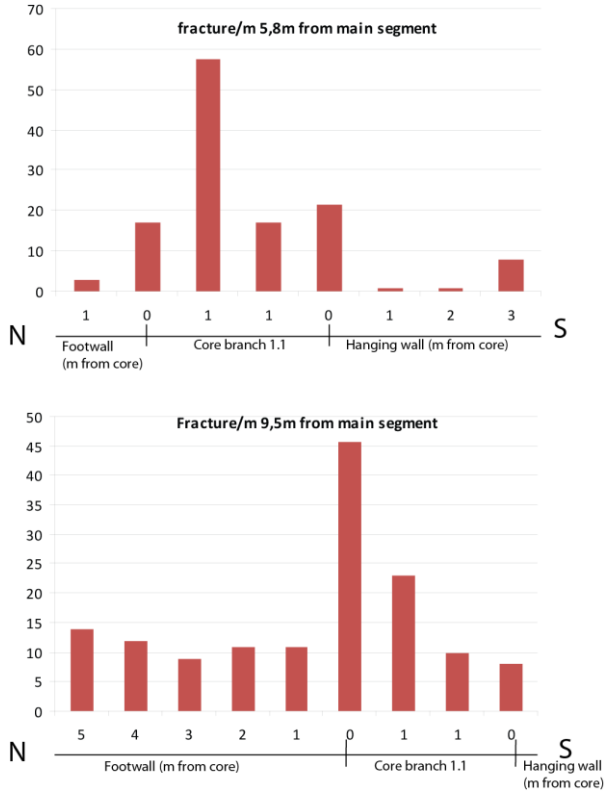

Figure 3.1.12 Fracture frequency diagram for branch 1.1 (see blue lines in figure 3.10 for exact location)

The fractures measured within the core of segment 1.1 are trending in three general directions ENE-WSW (y-direction), NNW-SSE and N-S (figure 3.1.13). Most of the fractures are trending in ENE direction and this is where there is greatest variance in dip from 58^{o} to 90^{o} are found. Fractures recorded to have a NNW direction generally have steepness variations from 75^{o} to 90^{o}.

Some of the fractures in the core had up to 2cm thick calcite mineralisation (figure 3.1.14). Mineralisation was only found on fracture surfaces within lenses close to the branching of segment 1.1, both inside main part of segment 1.1 and in lenses at the start of branch 1.1. Beside the mineralisation in the large lens in segment 1.1 there is also some deformation bands present. In domain *a* no evidence of mineralisation was found but some deformation

bands observed, displacing both a cluster of anastomosing bands and straight ones in y-direction. In domain *c* there are some clusters of short and straight deformation bands (figure 3.1.15).

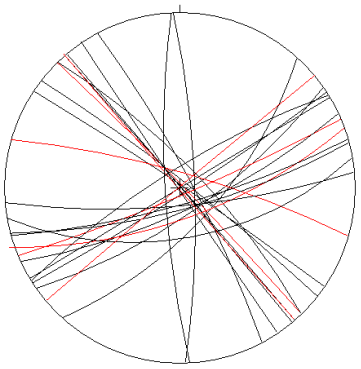

Figure 3.1.13 Fracture directions within core of segment 1.1 (red lines mark measurements from branch 1.1) N=25

Figure 3.1.14 calcite mineralisation (see red arrows), close to branching of segment 1.1 (Compass for scale)

Figure 3.1.15 Deformation band cluster Domain *c* (41m from cliff). 20 cm wide 20 cm long

3.1.2 Segment 1.2 description

Segment 1.2 is a more easterly part of fault 1. It was mapped for a distance of 40m down to the low tide mark from its appearance of the tidal flat. It appears 5,5 m from segment 1.1 following a NNW-SSW (345^{o}) directed fracture (figure 3.1.3). The fault core appears without any major change in topography, but is evident from its lenses and eroded fault core (figure 3.1.16).

Segment 1.2 can be divided into two domains, with the first half of the mapped segment representing domain *a* and the second half domain *b* (figure 3.1.3). These domains are mainly distinguished by damage zone differences.

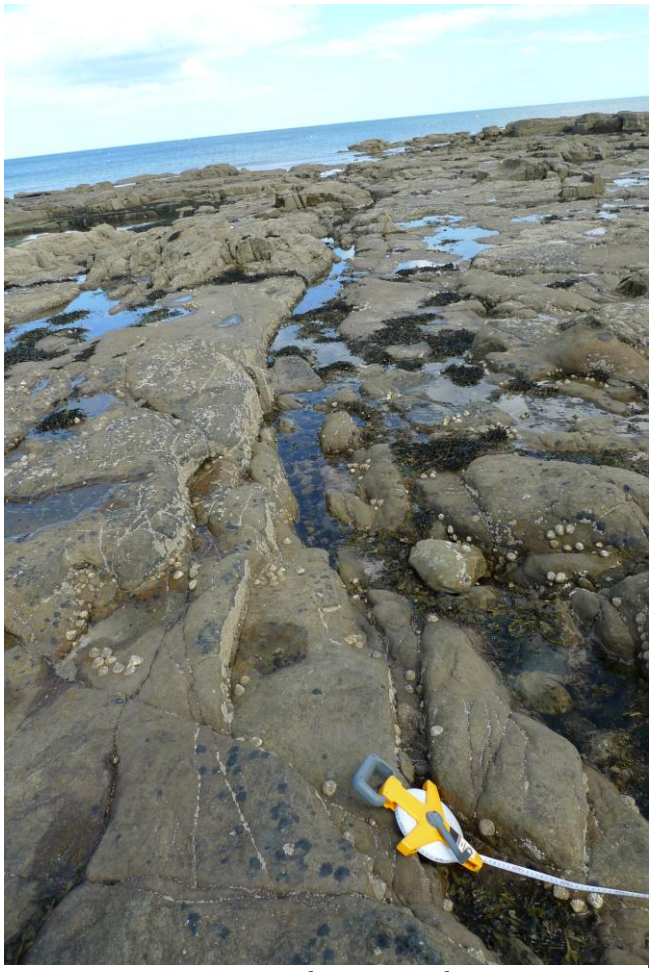

Figure 3.1.16 Segment 1.2 from start of mapping towards sea (measuring tape for scale)

Segment 1.2 has an overall direction of 45/85, NE trending (Figure 3.1.17a). This is a very steep fault, steeper than for segment 1.1 that had an overall dip of 79^{o}. The strike is trending 20^{o} more to the north than the strike of segment 1.1.

There are some differences between the measurements made for the hanging wall and footwall master branchline (figure 3.1.17b and c). They are both very steep, 83^{o} and 77^{o} respectively. The master branchlines are dipping in opposite directions. The southern branchline has a dip towards NNW while the northern towards SSE. This presents a scenario where the fault core acts as a negative flower structure with possible downfaulting from both sides.

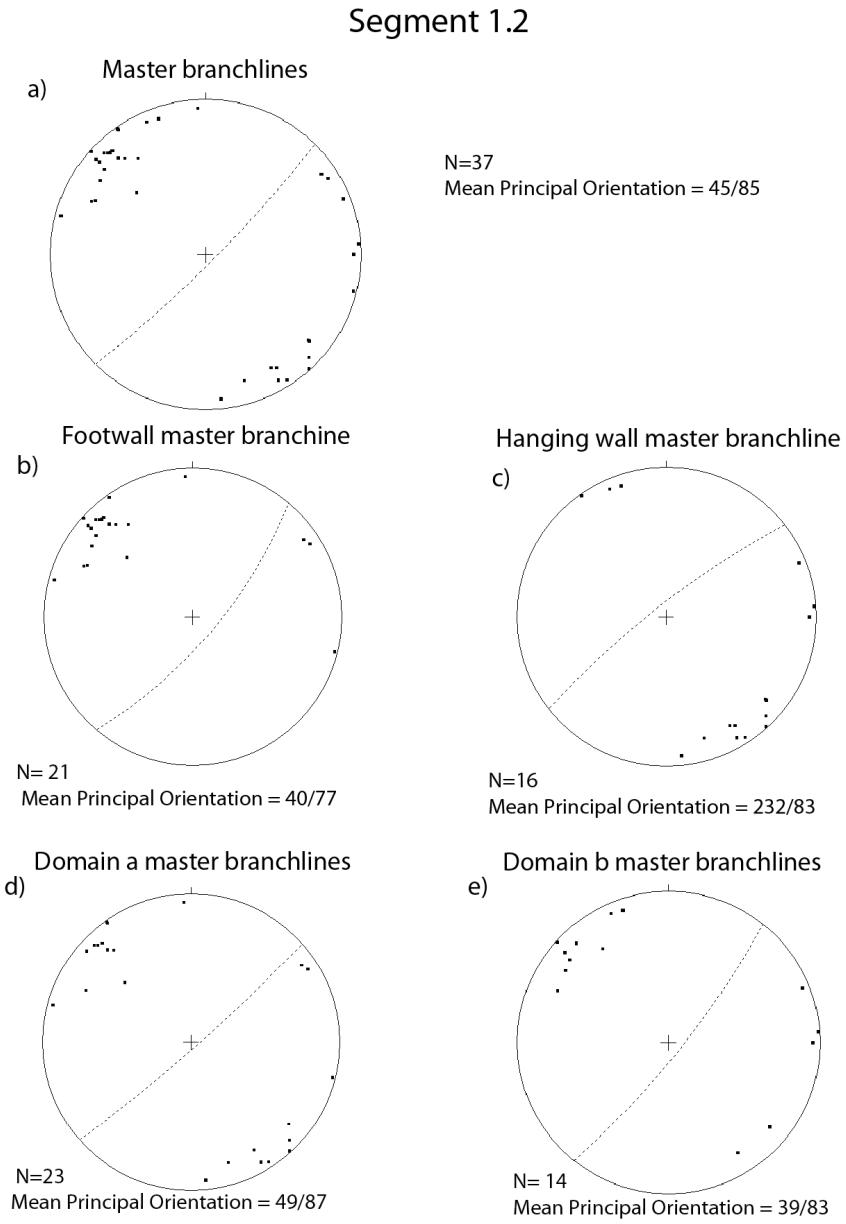

Figure 3.1.17 Stereographic projections from master branchline measurements along segment 1.2

a) All measurements from segment 1.2s master branchlines

b) and c) displays the splitting of a) into footwall master branchline measurements (b) and hanging wall master branchline measurements (c).

d) and e) displays the splitting of a) into master branchlines from domain *a* (d) and master branchlines from domain *b* (e)

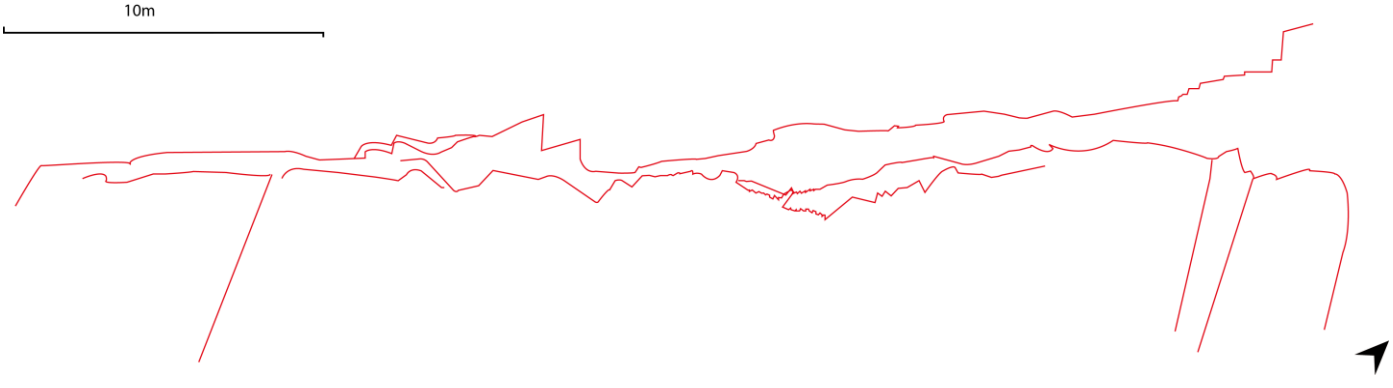

Figure 3.1.18 Horizontal section. Mapped master branchlines along segment 1.2. Note that the fault core is widening towards northeast (See appendix B for larger figure with additional information)

There are several potential branchlines from other segments linking up with segment 1.2 on the hanging wall (southern) side (figure 3.1.18). 6 m into domain *a* (from the appearance of segment 1.2 fault core) a fracture representing a potential master branchline directed from segment 1.1 meets up with the fault core. Approximately 5m from the low tide mark within domain *b*, the fault core of segment 1.2 joins in with Segment 1.1 core with an angle of 188^{o}.

Comparing the orientations for domain *a* and *b* (figure 3.1.17d and e) as well as looking at figure 3.1.18 indicate a slight change in strike along the segment. Domain *a* is in average 10^{o} more easterly directed than domain *b*, 49^{o}NE and 39^{o}NE respectively. The fault core in segment 1.2 is thinner than for segment 1.1. The core width varies between 5m and 0,1m along its strike, the thickest section is placed right at the low tide mark and the thinnest at the delimitation between domain *a* and domain *b* (Figure 3.1.18). Segment 1.2 is similar to segment 1.1. Several zones across strike often mark different style of deformation, both due to topographical variations and change in intensity of lens networks.

Domain *a* has a core variation between 0,1m and 2,0m. The thickest section is situated 24,5m from the low tide mark where the footwall master branchline expand following a fracture with 30^{o} angle to the main fault trace. Domain *a* has a thinner core than domain *b* which varies between 5,0m and 0,1m. The average core width for domain *b* is about 2m, while it is about 1m for domain *a*. The last 5 m towards the low tide mark shows an increasing core width.

Lenses

The core is similar to that of segment 1.1. In domain *b* one lens is partly made up of breccia (figure 3.1.19) other than that lenses are made up of relatively undeformed host rock.

A difference in lens layout is observed in the two domains, domain *a* has less and generally smaller lenses than domain *b* (figure 3.1.20). The largest lens measured in segment 1.2 has a *b*-axis of 5m and an *a*-axis of 0,9m (figure 3.1.20 and figure 3.1.21). The first part of this lens is dominated by conjugated fracture sets (figure 3.1.21a) also present in the hanging wall. The NE end of this lens has been eroded to a low level and is not dominated by the conjugated fracture sets of the hanging wall (figure 3.1.21b). *B*-axes directions measured from 35 of the lenses along segment 1.2 give a NE trend about 10^{o} more northerly than that of the master

branchlines (45/85) with 20% of the data within a range of 30°-35°E (figure 36). 8,7% of the lens data for segment 1.2 show a somewhat different trend ranging between 340°-345°NNW.

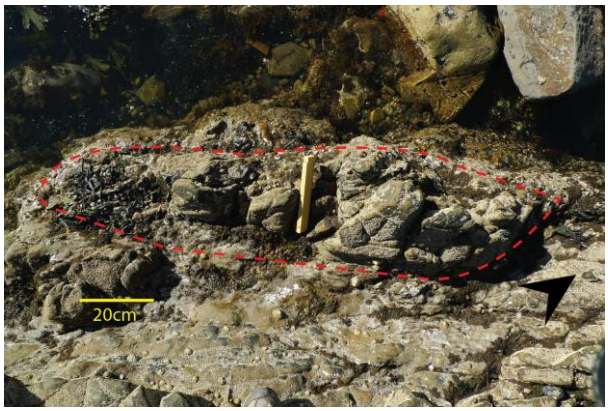

Figure 3.1.9 Lens made up of breccia in domain *b*

Figure 3.1.20 Horizontal section. Lenses (with yellow borders) and breccias (purple) in Segment 1.2. Note that there are more large lenses in domain *b* (figure 3.3).

a)

b)

Figure 3.1.21 Largest lens in segment 1.2 (5m *b*-axis)
a) SW end of the lens dominated by conjugate fracture sets
b) NE end of the lens eroded to a lower level

The largest lenses in domain *a* are situated at the beginning of segment 1.2 where there is 5 lenses of decent size, *b*-axes up to 2m. 3 of the larger lenses within the core in domain *b* have several smaller lenses within (figure 3.1.20). In the two lenses pictured in figure 3.1.22 it is clear that the *b*-axes direction differs from the low order lenses to the higher order ones. The low order lens has a *b*-axis direction similar to the fault trace while the higher order lenses has *b*-axis directions in a higher angle to the fault trace. For lens 1 the six higher order lenses

within have *b*-axis varying from 19^{o} to 56^{o} degrees different to the main trend. For lens 2 the four higher order lenses within have *b*-axis vary from 12^{o} to 38^{o} different to the main trend.

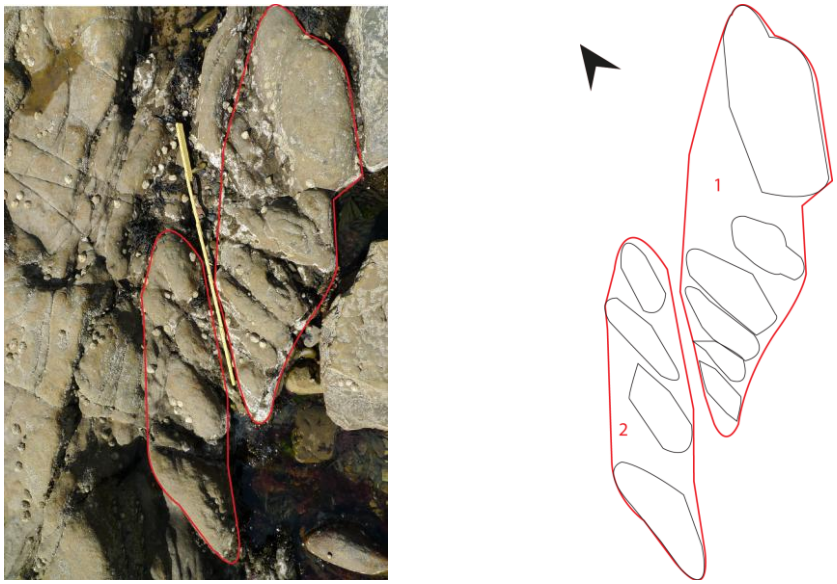

Figure 3.1.22 Picture and schematic sketch of two lenses NW of the lens pictured in figure 3.21. Low order lenses (red) with several higher order lenses within (black). (meterstick marks 1m)

Width(strike)-thickness relations for all recorded lenses in segment 1.2 are given in figure 3.1.23. Thicknesses vary from 0,06m to 0,9m and width from 0,2m to 5m. The best fitted regression line is the logarithmic trend with a confidence factor of 0,5, indicating a strong variance in the dataset. Using the logarithmic equation we get an average *b*:*a* ratio of 32,5:1 while using power equation(R^2=0,4617) we get an average *b*:*a* ratio of 10,6:1.

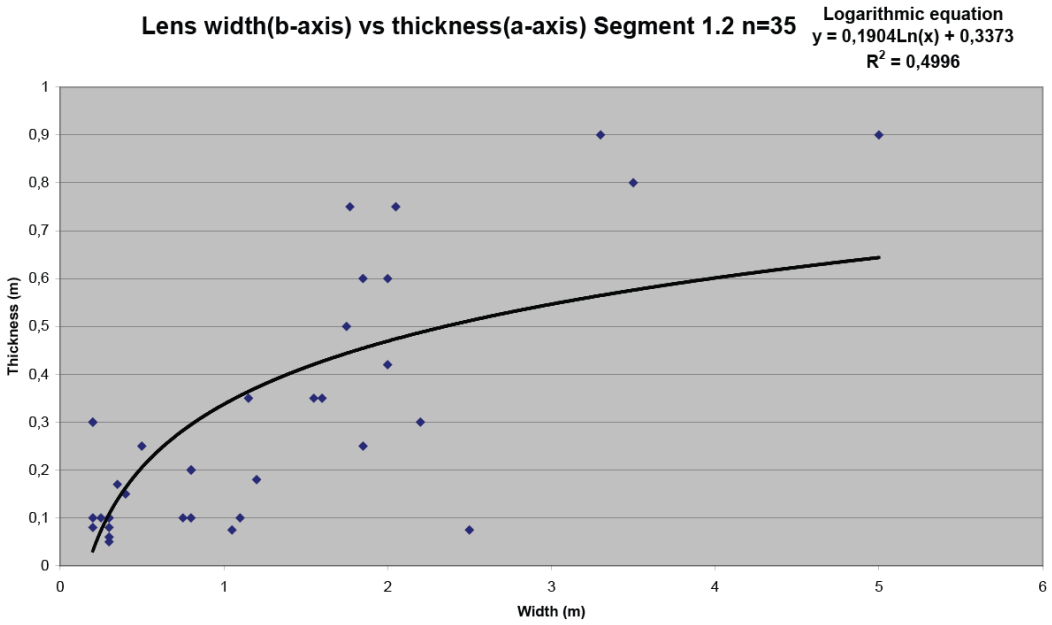

Logarithmic regression gives best fit b:a=32,5:1

b-axis directions Segment 1.2

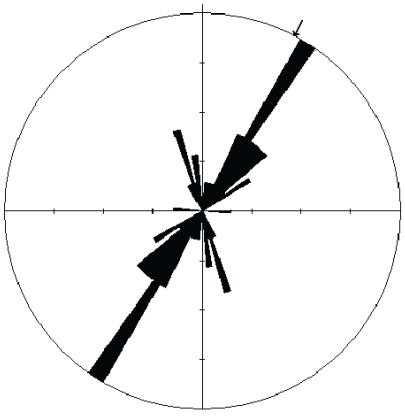

No. of Data = 35
Sector angle = 5°
Scale: tick interval = 5% [1,8 data]
Maximum = 20% [7 data]
Mean Resultant dir'n = 028-208
17,4%=035-050 [6 data] (15o sector angle!)
8,7%=340-345 [3 data]
5,8%=350-355 [2data]
5,8%= 055-060 [2 data]

Figure 3.1.23 Lens statistics for segment 1.2 displaying relative lens dimensions and *b*-axes directions

Fracture systems

The footwall and hanging wall are similar along domain *a* with a discrete, relatively randomly, spaced fracture network. For domain *b* the hanging wall is dominated by high frequency conjugated fracture sets while the footwall is similar to what previously recorded. The hanging wall side in domain *b* generally has a higher relief compared to the footwall and domain *a* (figure 3.1.24). Lenses close to the hanging wall and typically with a high relief tend to be similar to the hanging wall. Bounded and dominated within by conjugated fracture sets creating angular lens boundaries, such as the lens in figure 3.1.20.

One fracture frequency plot was made across segment 1.2 (figure 3.1.24 and 3.1.24). The fracture frequency is much higher in the fault core compared to the damage zones. There is no clear trend or signs of decreasing fracture frequency along the 20m of the hanging wall that's been plotted.

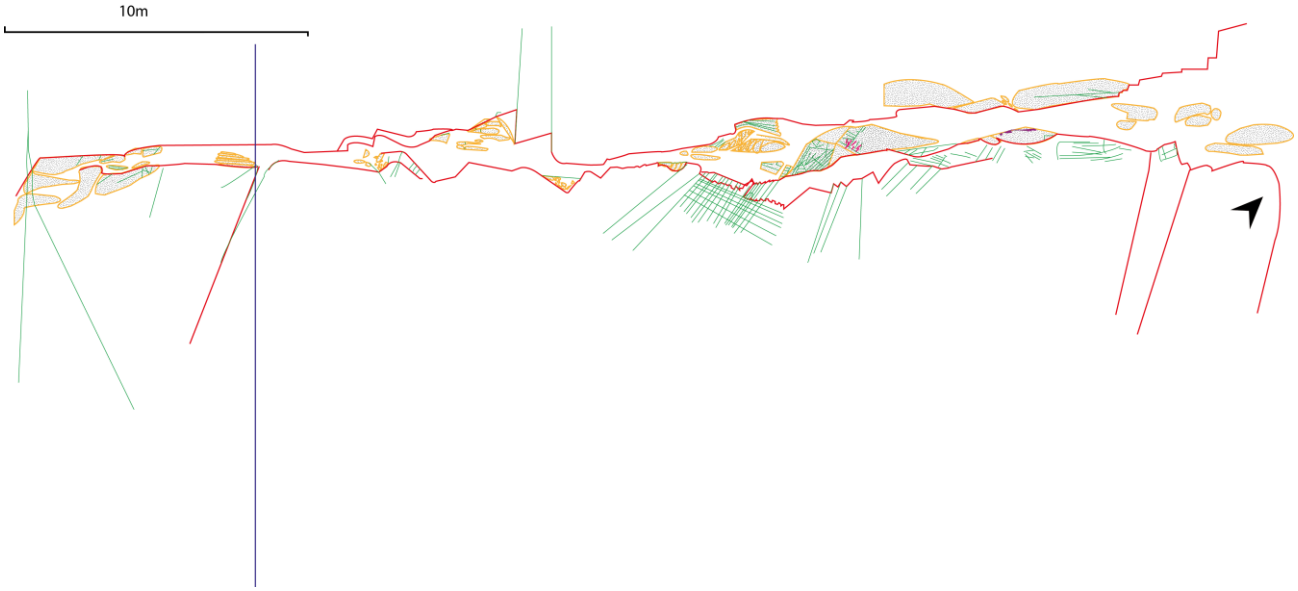

Figure 3.1.24 Horizontal section. Segment 1.2 Green lines mark fractures, pink lines deformation bands and blue line where fracture frequency plot has been made. Note conjugate fractures in hanging wall of domain *b* (see appendix B for larger figure)

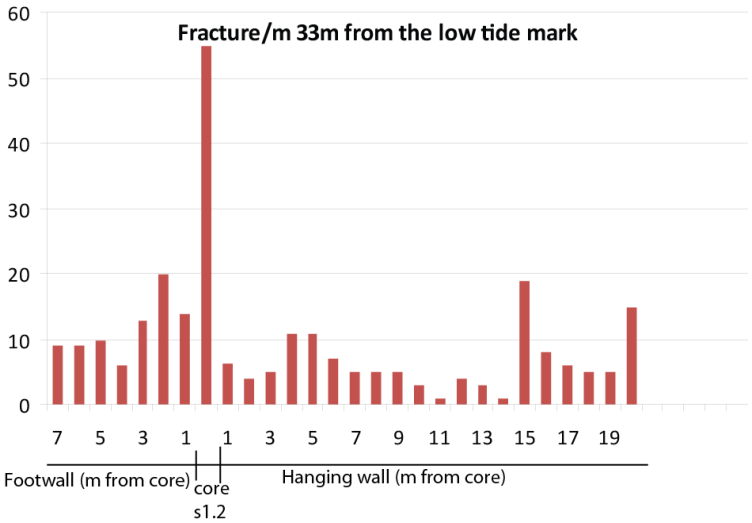

Figure 3.1.25 Fracture frequency plot perpendicular to segment 1.2 (see blue line in figure 3.24or exact location)

3.1.3 Continuation of fault 1 farther inland of segment 1.1

The two vertical exposures of fault 1, 0.1 and 0.2, are further inland from the tidal flat and segment 1.1. They are exposing what probably is the footwall master branchline (figure

3.1.26 and 3.1.27). Neither of the exposures gives a large window of observation, exposure 0.1 being the largest with a 1,5m height of exposure.

Exposure 0.1 have an orientation of 215/79 (figure 3.1.26) and exposure 0.2 have an orientation of 230/74(figure 3.1.27). Both show an over steepened fault surface, in relation to a normal offset to the SE, with slip surface dipping towards NW. Both slip surfaces are close to the average value for footwall master branchline dip from segment 1.1 at 77^{o} (figure 3.1.5)

a)

b)

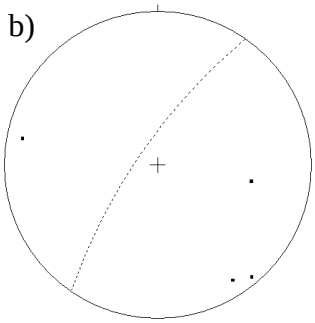

c)

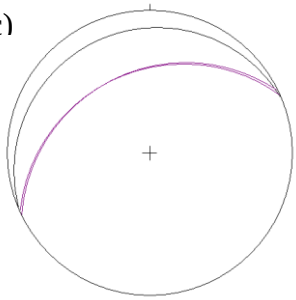

Figure 3.1.26 Exposure 0.1
a) picture taken towards the sea (20cm meterstick for scale)
b) Slip surface exposure 0.1
No. of Data = 4
Mean Principal Orientation = 215/79
c) Bedding planes exposure 0.1
Undragged part (black): No. of Data = 1
Mean Principal Orientation = 247/14
Dragged part (purple): No. of Data = 2
Mean Principal Orientation = 245/42

a)

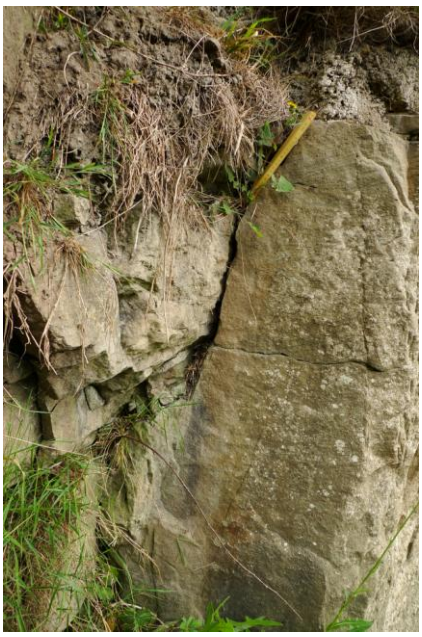

b)

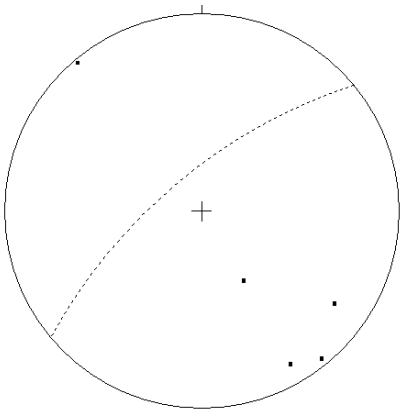

Figure 3.1.27 Exposure 0.2
a) Picture taken towards the sea (20cm meterstick as scale)
b) slip surface exposure 0.2
No. of Data = 5
Mean Principal Orientation = 230/74

Fault rocks

Close to the slip surface at exposure 0.1 there is a unstructured membrane that are softer than the surrounding rocks Adjacent to the membrane there is a part where bedding planes appear to have been dragged (figure 3.1.26). The bedding planes in the dragged part have the same strike as that measured in the undragged section but with a higher dip. 42^{o} compared to 14^{o} (figure 3.1.26).

Exposure 0.2 has on the southern side of its slip surface medium grain sized sandstone with cross bedding towards the top overlain by a siltstone and red sandstone. On the northern side there is massive sandstone overlain by more bedded sandstone.

3.1.4 Segment 2 description

The fault of segment 2 juxtaposes sediments within the hanging wall of fault 1. It is a small subsidiary fault with an estimated normal vertical offset of 40cm that has not previously been mapped.

Segment 2 is exposed as an erosional track along the tidal flat from a grassy hill towards the sea, where it can be viewed in cross section close to the grassy hill (figure 3.1.28 and figure 3.1.29). Further inland from the tidal flat no traces of the fault was detected. It is easily accessed on the tidal flat adjacent to fault segments from fault 1.

Segment 2 was only mapped in detail for 17m along its fault trace. The continuation of the master branchline traces were mapped from lineaments evident from the aerial photograph (figure 3.1.1 and 3.1.2). It was noticed both in field and from the aerial photograph that the fault trace of segment 2 meets up with Segment 1.1 (figure 3.1.3 and chapter 3.1.2).

Segment 2 has mainly been mapped along strike but a one meter high section was mapped vertically near the grassy hill so that figure 4 shows a chair view of the fault. Strike of the fault indicates that it links up with Segment 1.2 down by the low tide mark, which is confirmed, and possible segment 3 further inland.

It is a synthetic subvertical (87^{o} dipping) fault with a vertical offset of 40cm down towards West and has an overall strike of 188^{o} to the SSW (figure 3.1.30). The overall dip to the east

(figure 3.1.30) doesn’t fit with the observed vertical offset. This is most likely due to the steepness of the fault and possibly the limited amount of measurements along strike.

The fault core varies in size from 10cm to 8m being situated at the cross-section to map view transition at the end of the mapped section respectively. It has an even widening tendency throughout the mapped section (figure 3.1.30).

Figure 3.1.28 Segment 2 viewed towards the sea. Red lines mark master branchlines

Figure 3.1.29 mapped cross section of segment 2 with breccias (1m meter stick for scale)

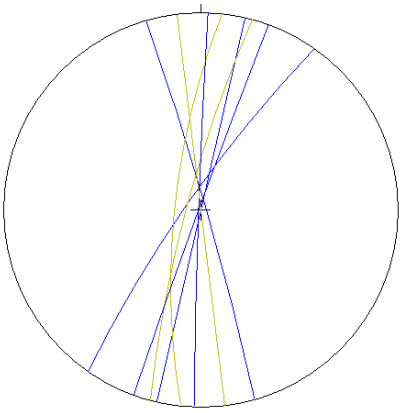

Figure 3.1.30 The fault core varies in size from 10cm to 8m being situated at the cross-section to map view transition at the end of the mapped section respectively. It has an even widening tendency throughout the mapped section (figure 3.31).

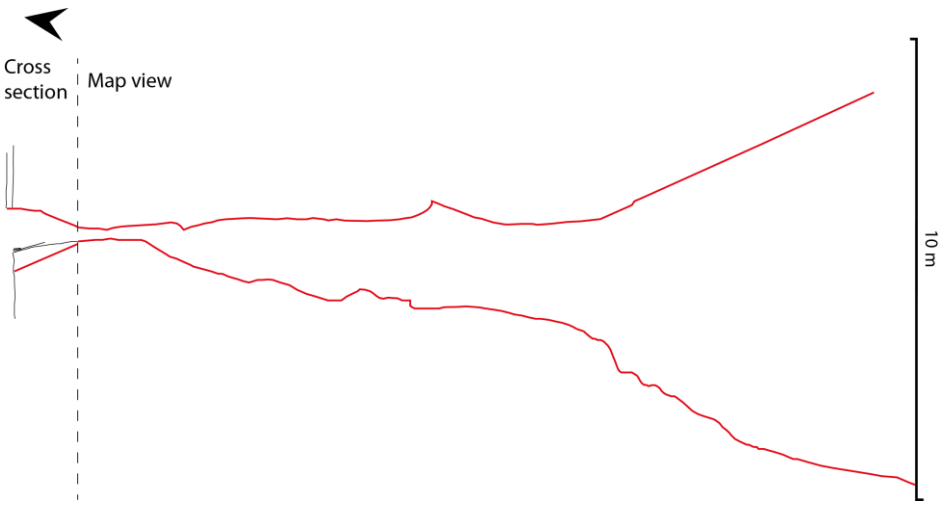

Figure 3.1.31 Segment 2 master branchlines. The core is widening towards the end of the mapped section.

Lenses

The core consisted of lenses bounded by zones that at recent times have been eroded in map view, similar to the segments of fault 1. The cross section that has been mapped consists of faulted rock probably part of lenses bounded by slip surfaces and breccias (figure 3.1.29). The breccia photographed is clast supported with about 10% matrix.

Lenses mapped from segment 2 are given in figure 3.1.32. The largest complete lens measured from segment 2 has a *b*-axis of 3,7m and a-axis of 1,7m. There is a low degree of symmetry in the lenses mapped in segment 2. *B*-axes directions measured from 16 lenses along segment 2 give the plot of figure 3.1.33. The directions are mainly spread in the same manner as the master branchline directions (188/87) with 14,8% of the data within a range of 360^{o}-10^{o}N (figure 3.33). 12,4% of the lens data for segment 2 show a trend ranging between 335^{o}-340^{o}NNW oriented 30 to the west of the most dominating trend.12,4% a trend ranging between 15^{o}-20^{o}NNE.

The largest lens has several lenses within. It comes to an abrupt end 16m from the hill where a fracture is marking level change in the tidal floor with the part mapped being on a higher level. Width(strike)-thickness relations for the lenses measured in segment 2 are presented in figure 3.34. Thicknesses vary from 0,08m to 1,7m and widths vary between 0,3m to 5m. The best fitted regression line is the power law trend with a confidence factor of 0,55, indicating a strong variance in the dataset. Using the power equation we get an average *b*:*a* ratio of 6,4:1.

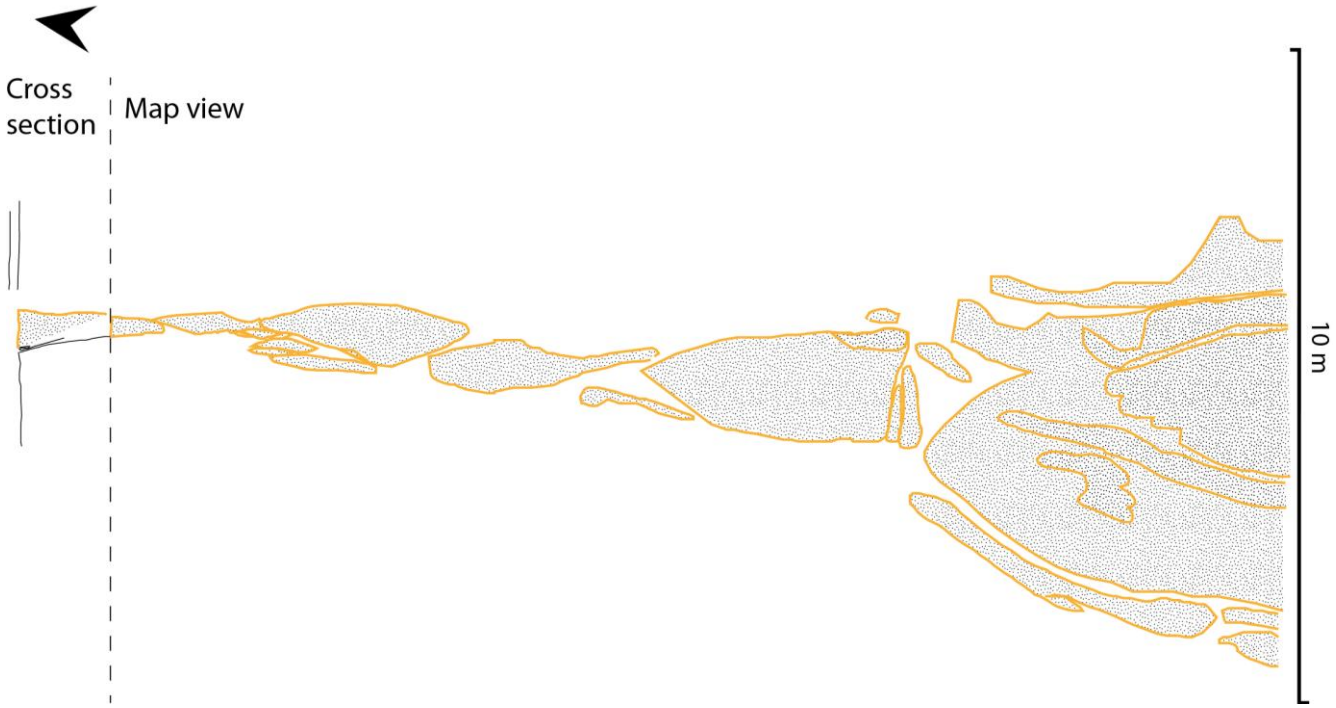

Figure 3.1.32 Lenses in segment 2. The largest lens is located in the widest part of the core and has several smaller lenses within.

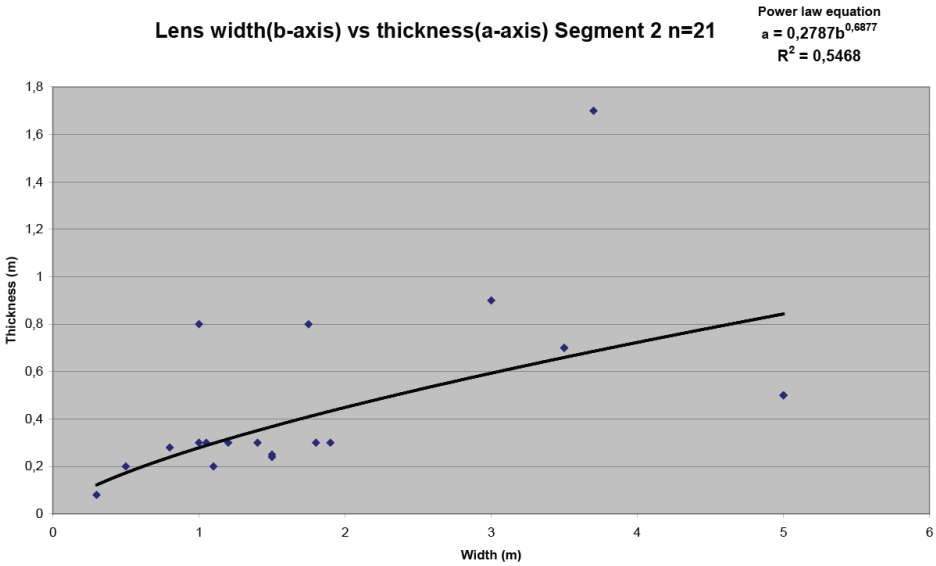

Power law regression gives best fit b:a=6,41:1

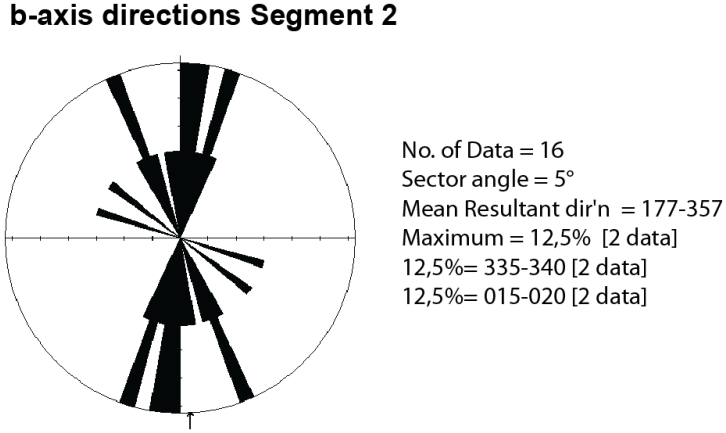

Figure 3.1.33 Lens statistics for segment 2 displaying relative dimensions and *b*-axis directions

Fracture systems

There were several fractures within lenses and on the sides of the fault core of various extents (figure 3.1.34). One fracture splays of the western master branchline, directed 320^{o}NW, and goes towards the innermost part of segment 1.2 (figure 3.1.3). No mineralization was observed except along the eastern master branchline of the cross section where there is some calcite mineralization.

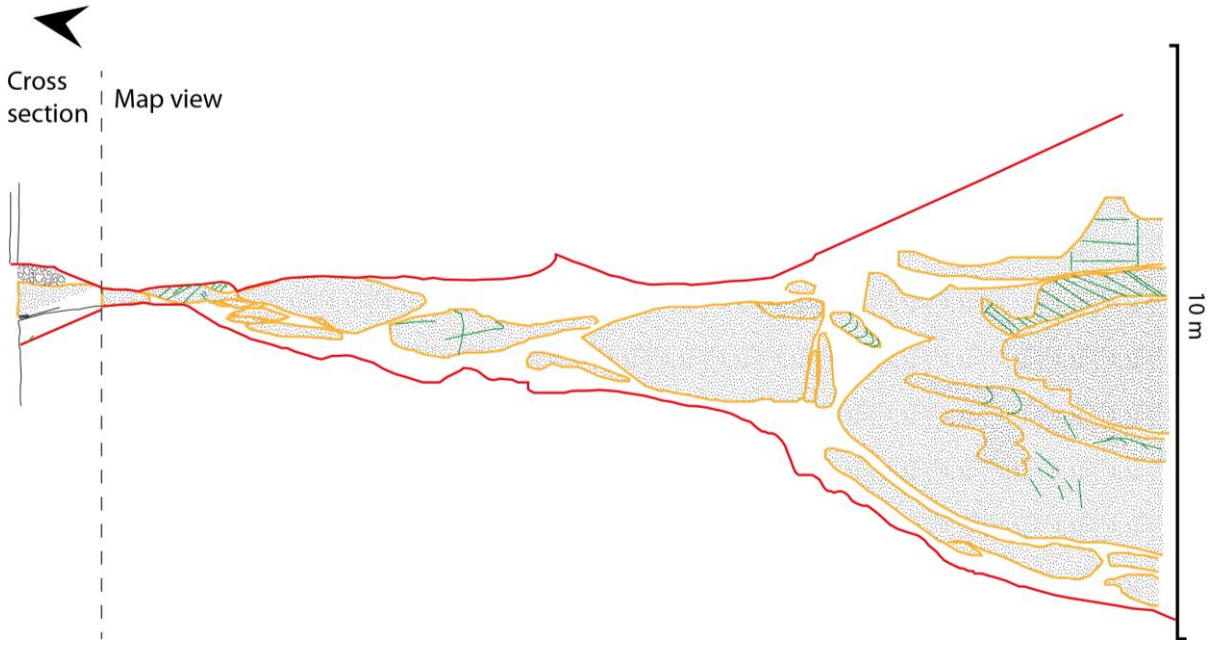

Figure 3.1.34 Horizontal section. Segment 2 (green lines represent fractures)

3.1.5 Segment 3 description

Segment 3 was described in 2006 by Færseth as part of a study comparing faults with smear. It has normal vertical offset of 21m to the north where two 0,15 and 0,35m thick coal beds have been smeared along the fault core at least 3,5m to the base of the exposure where the smear remains continuous (Faerseth 2006).

Segment 3 is about 20-30m SE of fault 1 (figure 3.1.3). And has not been mapped in great detail in this study as a large part of the fault now is covered up by constructions from nearby cabins, but one simplified profile of the components that are visible has been made. It is

because of the construction only possible to see the thinnest coal bed described by Færseth (2006).

From the aerial photograph it is possible to detect the fault trace of segment 3 (figure 3.1.1 and figure 3.1.3) as it marks a difference between rock floor and sand. On figure 3.1.2 the fault is marked as a single red line at the SE edge between sea and tidal flat. Segment 3 and fault 1 are forming a graben.

There was made a profile of segment 3 showing the part that still is exposed (figure 3.1.35). The lineament along strike to sea was only mapped from the aerial photograph and measurements were taken from the mapped profile.

The orientation of segment 3 is 253/60, measured from two slip surfaces one along the smeared coal and one within the fault core (figure3.1.36). The slip surface along the coal membrane is representative for footwall master branchline. The other slip surface is between the two sandstones outlined in figure 3.1.35 and has about the same direction but with larger variance.

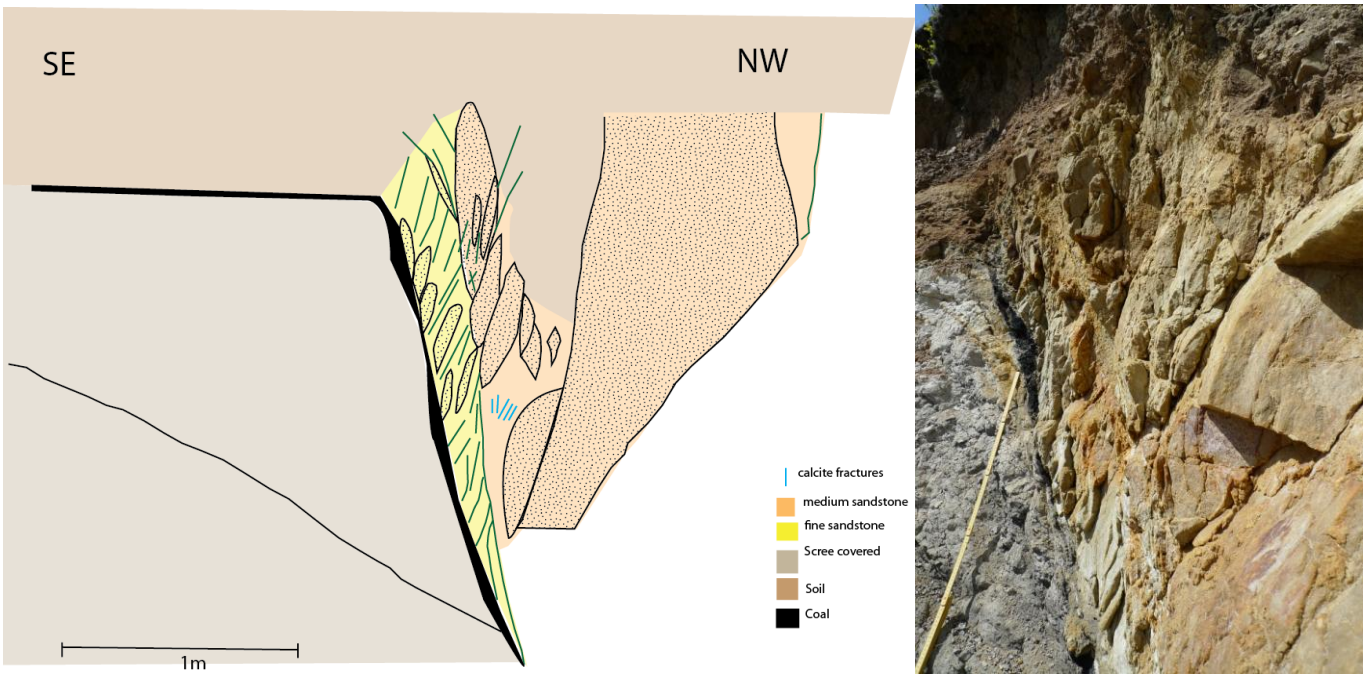

Figure 3.1.35 Vertical section. Segment 3, Sketch to the left and picture to the right. Picture showing close up of fault core (meterstick marks 1m). The area close to the footwall consists of finer grained sandstone and generally smaller lenses.

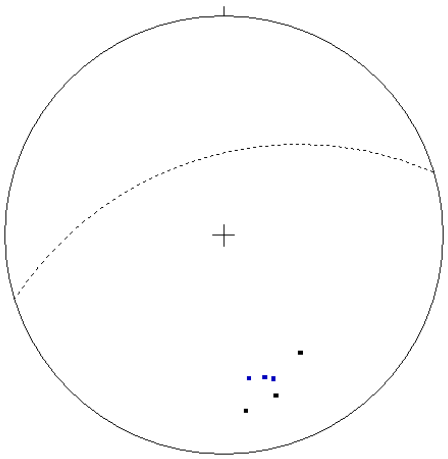

Figure 3.1.36 Slip surfaces segment 3. Black points mark footwall master brancline (coal membrane) blue point marks the interface between medium to fine sandstone.
No. of Data = 6
Mean Principal Orientation = 253/60

The hanging wall master branchline has not been identified but the amount of lenses and fractures are decreasing to the north of the footwall master branchline indicating that most of the deformation is accommodated near this. Thickness between the two slip surfaces described above is increasing from 0cm at the base of exposure to 30cm at the top (figure 3.1.35). The smeared coal is varying in thickness along the footwall side of the fault core from 20-2cm. It is smeared from the footwall 3,5m to the base of the exposure (figure 3.1.35).

Lenses

The lenses closest to the footwall are paler and consist of finer grained sandstone than the ones closer to the hanging wall (figure 3.1.35 and 3.1.37). Rocks in the footwall are shaly and easily erodible which make them prone to be scree covered. The fault is cutting bedding with orientation of 248/27 possibly representing a channel. Rocks in the hanging wall are the ones faulted in segment 2 and fault 1 and consist of medium grained sandstone.

There appear to be two lens sections defined by sandstone type. The lenses in the pale sandstone are smaller and thinner than the ones towards the hanging wall with a *c*:*a* ratio of about 1:6 while the ones in the more coarse grained sandstone have a *c*:*a* ratio of about 1:4 (figure 3.1.35 and 3.1.37). The largest lens there's made measurements on have an *a*-axis of 0,9m and a possible *c*-axis based on symmetry of about 13m giving an *c*:*a* ratio of 1:14.

As figure 3.1.35 displays a vertical section it was impossible to measure *b*-axis directions on the lenses but strike and dip measurements were made around them (figure 3.1.37). Most of the lenses measured are oriented in the same direction as the slip surfaces (Figure 3.36) with an average of 64/78 as opposed to 253/60 for the slip surfaces. Majority of the lens measurements have antithetic dip and they are generally steeper than the slip surfaces. This can either reflect axial variations or be due to variations in lens measurements. Based on the sketch in figure 3.1.35 it is seems likely that most lenses have antithetically dipping *c*-axis. As the hanging wall master branchline has not been identified it is impossible to see if this trend is representative only close to the footwall or across the entire core.

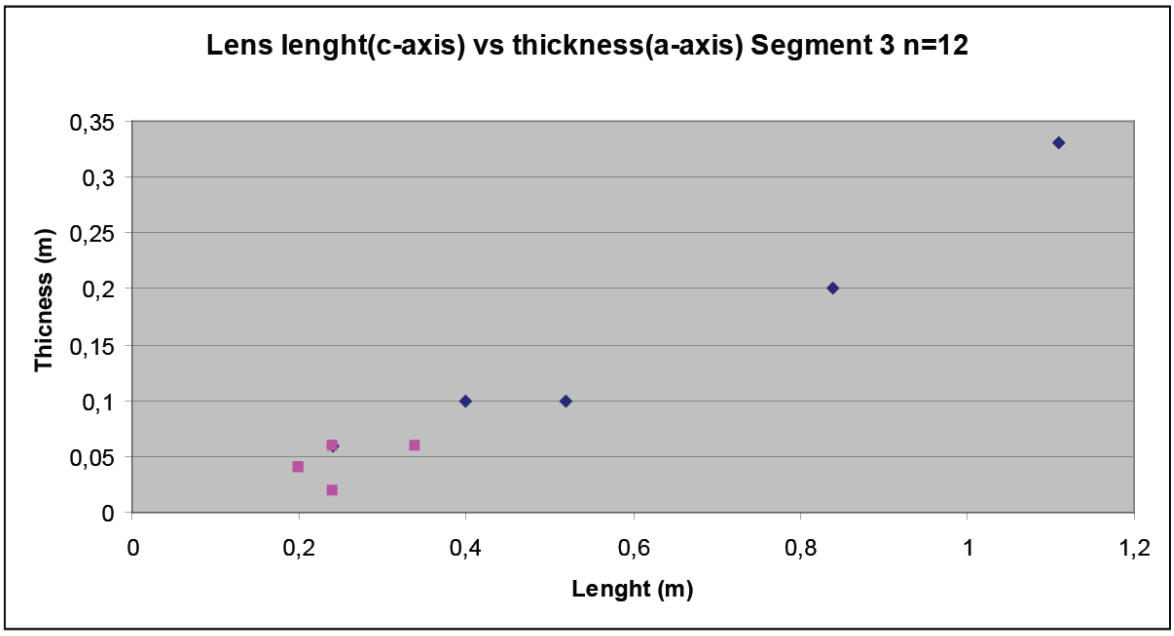

Pink points represent lenses in fine grained sandstone between the two slip surfaces, blue represent lenses in the coarse grained sandstone towards the hanging wall

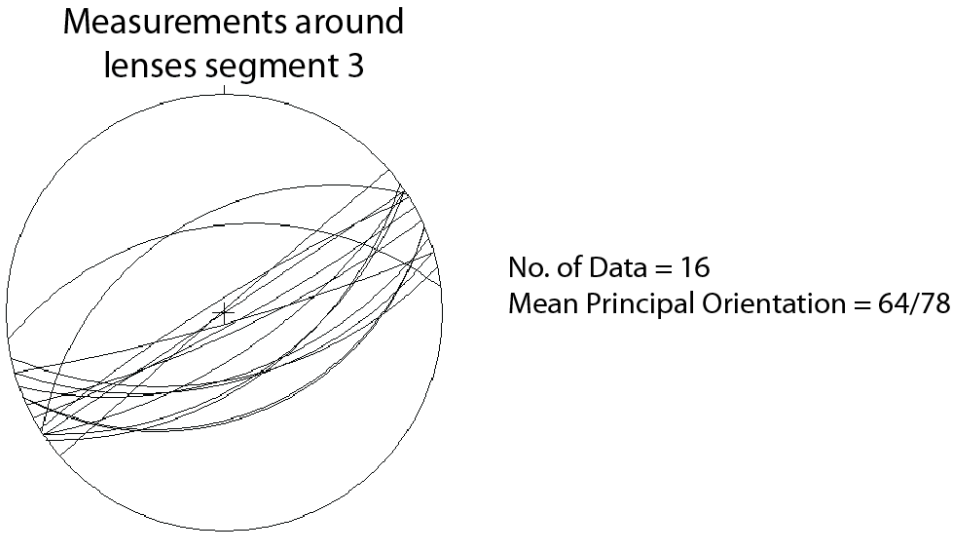

Figure 3.1.37 Lens statistics for segment 3 displaying relative dimensions and measurements made around lenses

Fracture systems

The pale sandstone is dominated by a discrete fracture network oriented in a 20-30^{o} steeper angle than the footwall master branchline. There are several fractures in the more coarse grained sandstone but not with a clear orientation trend.

Figure 3.1.35 show a set of calcite fractures in the coarse grained sandstone clustered in a small area. They all have similar length of about 40cm each. They are steeply dipping from 82^{o} to 90^{o} with a strike varying from 55^{o} to 97^{o} direction (figure 3.1.38) which is similar to the footwall master branchline.

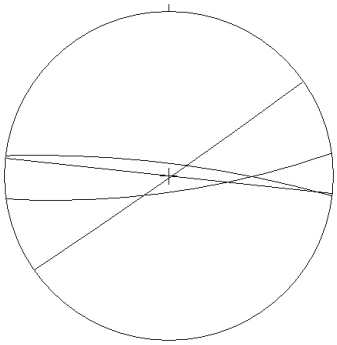

Figure 3.1.38 calcite fractures segment 3
No. of Data = 4
Mean Principal Orientation = 83/89

3.1.6 Overall characteristics of Snab Point locality

The different segments of the main fault (fault 1) share some overall characteristics such as steep master branchlines measures for normal faults. Fault 1 is striking in an ENE-WSW to NE-SW direction. Heavily deformed fault rocks are scarce along the fault trace as area of most intense deformation has been eroded. The core width varies along the fault trace, as indicated by the presence and varying size of lenses. Large lenses are present in the widest part of the core, while in thinner parts lenses are small/non-existent. Most of the large lenses have several smaller lenses within themselves. Fractures are present both in the damage zones and in the core and often coincide with changes in the core width.

At Snab Point the lenses generally show a low degree of symmetry with varying sides and rough ends. However there are examples of very symmetric four sided lenses both along the southern master branchline of branch 1.1 (figure 3.1.7) and in the core of segment 1.2 (figure

3.1.22). Overall segment 1.2 was dominated by a more symmetric lens population than both segment 1.2 and segment 2. This is the fault segment with smallest range of lenses and the lowest lens density thus having a more homogeneous lens population

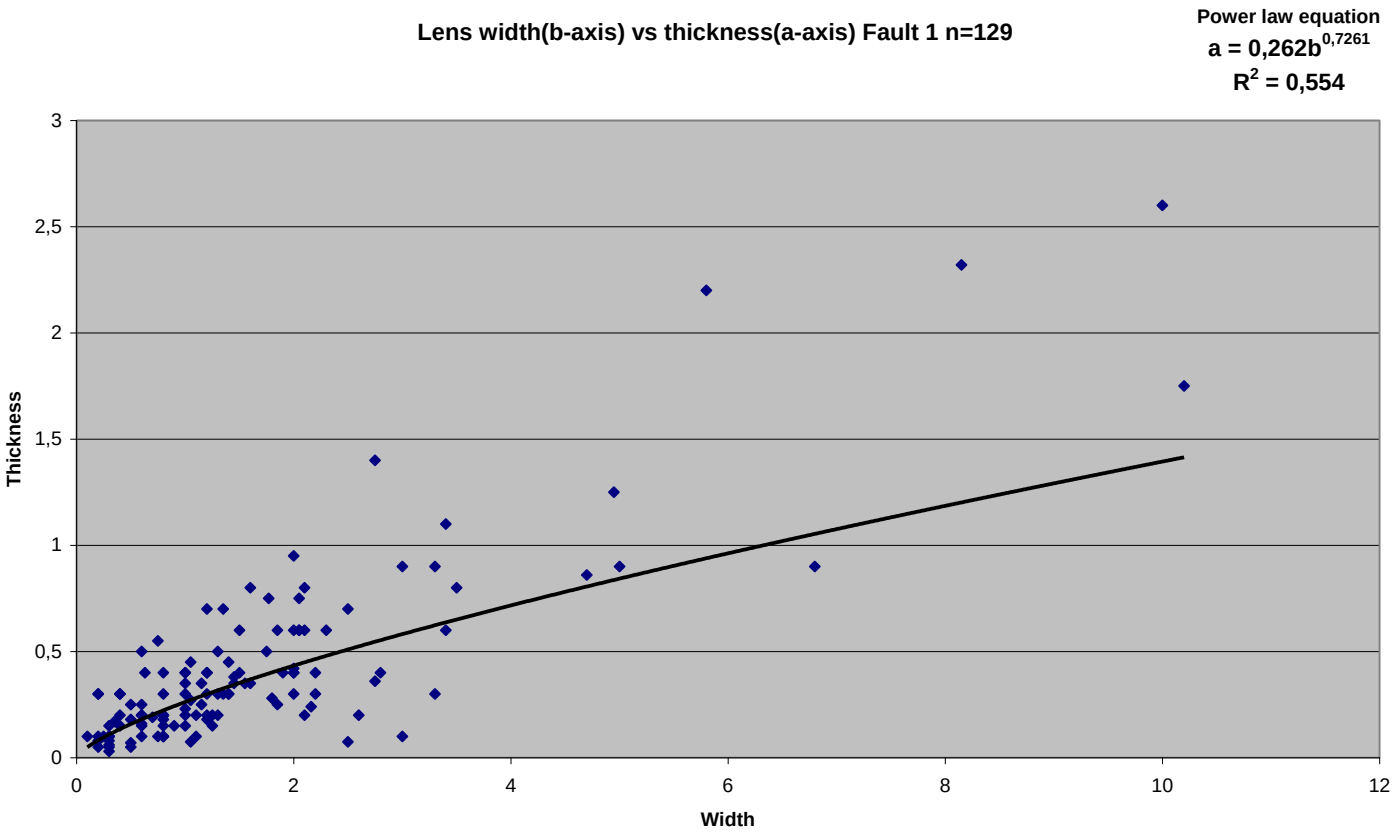

Figure 3.1.39 relative dimensions for all lenses in Fault 1. Power law giving best fit. b:a=6,33:1

Width(strike)-thickness relationships for all recorded lenses in fault 1 are given in figure 3.1.39. Thicknesses vary from 0,03m to 2,60m and widths vary between 0,10m to 10,20m. The best fitted regression line is the power trend with a confidence factor of 0,55, indicating a strong variance in the dataset. Using the power equation we get an average *b*:*a* ratio of 6,33:1.

Fault 2 has relatively similar characteristics to fault 1.It is a very steep fault with a fault zone that appears to widen according to lenses present in the core. As opposed to fault 1 segment 2 is representing a fault with a minor vertical offset. Segment 2 is striking in a different direction compared to the other segments at Snab Point 188^{o}SSW, 58^{o} north of segment 1.1 and 37^{o} north of segment 1.2 (without regard to dip). Compared to Segment 3 it is striking 65^{o} to the south.

Fault 3 is opposed to the other faults at the site displaying a shallower dip of 60^{o} compared to the near vertical dip of all the other segments. It also differs in that this fault has cut through beds of different lithology and that the hanging wall and footwall thereby have different mechanical properties. The direction of segment 3 (253^{o}NNW) is 67^{o} to the west of segment 1.1 and 52^{o} to the west of segment 1.2.

3.2 Locality Crag Point

The Crag Point Fault is accessed from the top of a talus slope about 9m above sea level (figure 3.2.1 and 3.2.3). It is possible to view the Crag Point Fault in cross section along dip for about 12m. The soft, shaly rocks of the footwall have been preferentially eroded, extending the visibility of the footwall master branchline by several metres along strike. A rope was hanged from the cliff top, making it possible to climb up along the footwall master branchline to the point where the lower Crag Point Sandstone is outcropping in the footwall.

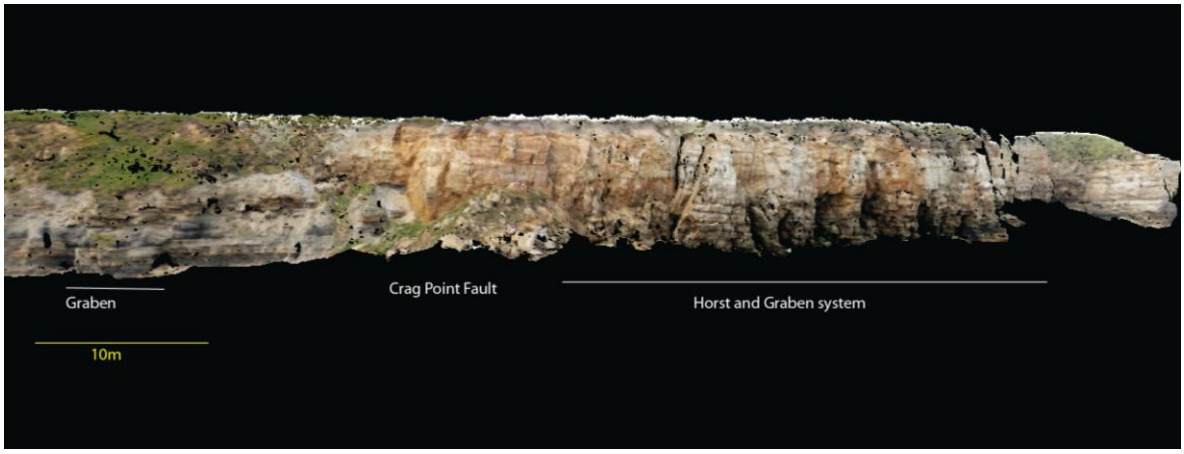

Figure 3.2. 1 LiDAR scans of segments studied at Crag Point (See appendix B for the image in A3 size)

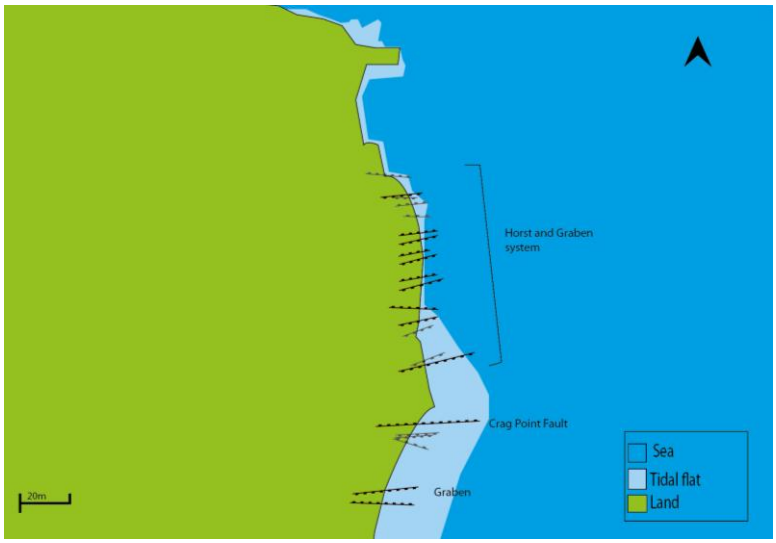

Figure 3.2. 2 Overview of all studied faults at Crag Point in map view. The length of the faults are illustrative as the along strike fault trace has not been mapped

The main fault at this location is the Crag Point Fault, and subsidiary structures close to it have been described by Jones (1968) and illustrated by Land (1974) where the main fault is described as a normal fault dipping towards north. The Crag Point Fault is a subvertical fault with a vertical offset of 11m down to the north. In our window of observation the fault has the

Upper Craig Point Sandstone on the hanging wall side and delta plain deposits with the lower Craig Point Sandstone on top at the footwall side (Jones 1968, Land et al. 1974). The vertical offset was measured by Jones on the basis of outcrops on both sides of the fault core of the coal bearing Five Quarter Seem. At the present time it is not possible to determine the vertical offset of the fault as Jones did as a talus slope covers the base of the cliff, where Jones (1968) reported the Five Quarter Seam to appear. On the hanging wall side of the main fault there is a 100m wide horst and graben system, described separately (figure 3.2.1 and 3.2.2). On the northern side of this system there is a fault of 52m vertical offset towards the south(Jones 1968), however this fault is not described in this study. On the footwall side of the main fault there is a graben which is described separately in the following chapter (figure 3.2.1 and 3.2.2).

All faults at Crag Point have been mapped in cross sectional view. The faults will be described according to variations in geometry, core width, fault core lenses, fracture systems within the fault zone, presence of mineralization and type of fault rocks. The following section provides a detailed description of the Craig Point Fault, beginning with fault zone overview. Thereafter the master branchlines and core will be described, followed by accommodation structures in the immediate 10m of both the footwall and hanging wall. Subsequently, descriptions of the graben south of the main fault and the 100m wide horst and graben system are provided.

The faults at Crag Point are not detectable on aerial photographs however they are visible from the tidal flat (figure 3.2.1). From figure 3.2.1 and figure 3.2.3 we can see that Crag Point Fault is identifiable from a distance by change in stratigraphy from upper delta plain deposits in the footwall to channel sandstones in the hanging wall. Figure 3.2.2 shows the position of faults studied at Crag Point in map view based on field measurements. The faults at Crag Point are well exposed in vertical sections of the cliffs. The variable steepness and relief of the cliffs provide good 3D images of the faults at Crag Point. The exposed section is limited representing only part of the fault segment.

3.2.1 Crag Point Fault description

The fault zone has a width of 30-160m. The proximal 17m of the hanging wall is intensely fractured adjacent to this is a c.100 meter wide horst and graben system. Thus the hanging

wall damage zone is between 17-120m depending on how it is defined. On the footwall side there are subsidiary faults for c.12m from the footwall master branchline. The transition between the footwall damage zone and the southern graben fault zone is unclear. The latter may be included into the main faults damage zone, which would be about 40m on the footwall side.

Figure 3.2. 3Picture of Crag Point Fault where the main fault trace is apparent from a change in lithology (photo courtesy Simon Bucley)

Figure 3.2. 4 To the left: picture of coal striations on cataclasite along footwall master branchline indicating horizontal slip of 14m in a dextral sense..
To the right stereographic plot of pictured (1) and another set of coal striations on slip surface close to the footwall(2)

1. **Strike 79 Dip 87 Pitch 38E**
2. **Strike 253 Dip 80 Pitch 34E**

No. of Data = 2
Mean Principal Orientation = 256/85
Mean Pitch = 36E

From the juxtaposition of upper delta plain deposits against major channel deposits of the upper Crag Point Sandstone the vertical offset across the Crag Point Fault is estimated to a minimum of 8m using LiDAR imagery. Two diagonal slickenlines of coal streaks were found across breccias along the footwall master branchline (figure 3.2.4) the horizontal component was calculated from these. Using the average angle of the coal striations measured compared to the vertical offset of 11m given by Jones (1968), trigonometric functions give a horizontal offset of 14m in a dextral sense.

The Crag Point Fault has an overall orientation of 79/89. It is a very steep fault (dip varying from 70^{o} to 90^{o} (figure 3.2.5 a) with vertical displacement predominantly down to the north. Along the hanging wall master branchline there is an offset of 0,55m down to the south. Figure 3.2.5 c and d show that the hanging wall and footwall master branchlines are trending in opposite direction in compliance with the dip direction on both sides. This implies that the Crag Point Fault core acts as a negative flower structure. The strike and dip measurements for the hanging wall master branchline are more scattered than the footwall ones. There is a swarm of slip surfaces near the hanging wall all of which are branchline candidates. The dominant surface at the position of measurement was considered to represent the hanging wall master branchline. Both the footwall master branchline and the hanging wall master branchline are steep, with average dip gradients of 86^{o} and 79^{o} respectively. There is a 23^{o} difference in strike regardless of dip direction in the footwall and hanging wall measurements 63^{o}ENE and 266^{o}WSW respectively.

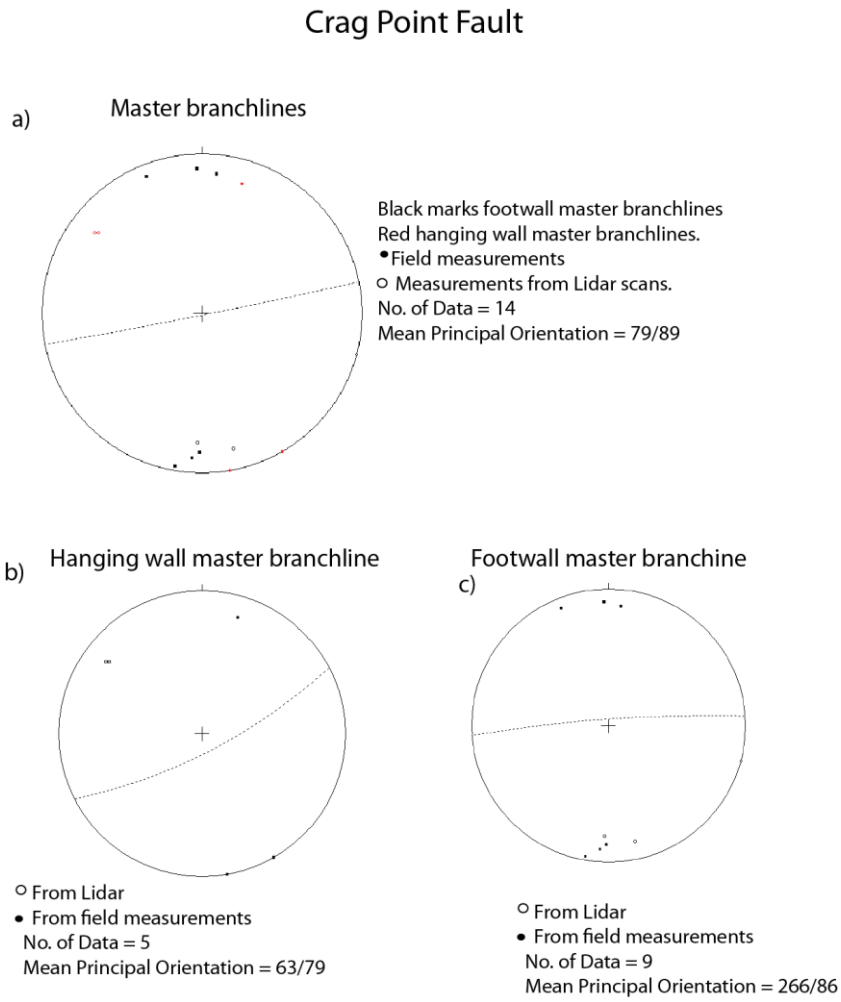

Figure 3.2. 5 Stereographic projections from master branchline measurements from Crag Point Fault
a) Measurements from the Crag Point Faults master branchlines compromising both field measurements and measurements extracted from LiDAR scans
b) and c) displays the splitting of a) into footwall master branchline measurements (b) and hanging wall master branchline measurements (c).

Core of the Crag Point Fault

The width of the fault core varies between one to seven metres along dip in relation to number and width of lenses present in the core. It is thinnest at the bottom of the exposure, 0.4m, and thickest at the top, 7m (figure 3.2.6), with an average core thickness of *c*.1.2m.

The lenses measured vary over four orders of magnitude from cm scale to the largest with *c*-axis of 10m and *a*-axis of 1,8m. The larger ones form the major constituents of the core (figure 3.2.6) whereas smaller ones are located in zones with multiple slip surfaces (figure 3.2.7b). The following section describes the largest two lenses as these are major constituents of the core in our window of observation, potentially exercising great control on fault core

width. The lenses are described according to their size, bounding surfaces, shape, lithology and degree of internal deformation.

Figure 3.2. 6 Crag Point Fault from LiDAR imagery. Red lines mark master branchlines White number and lines reefer to lenses described in the text

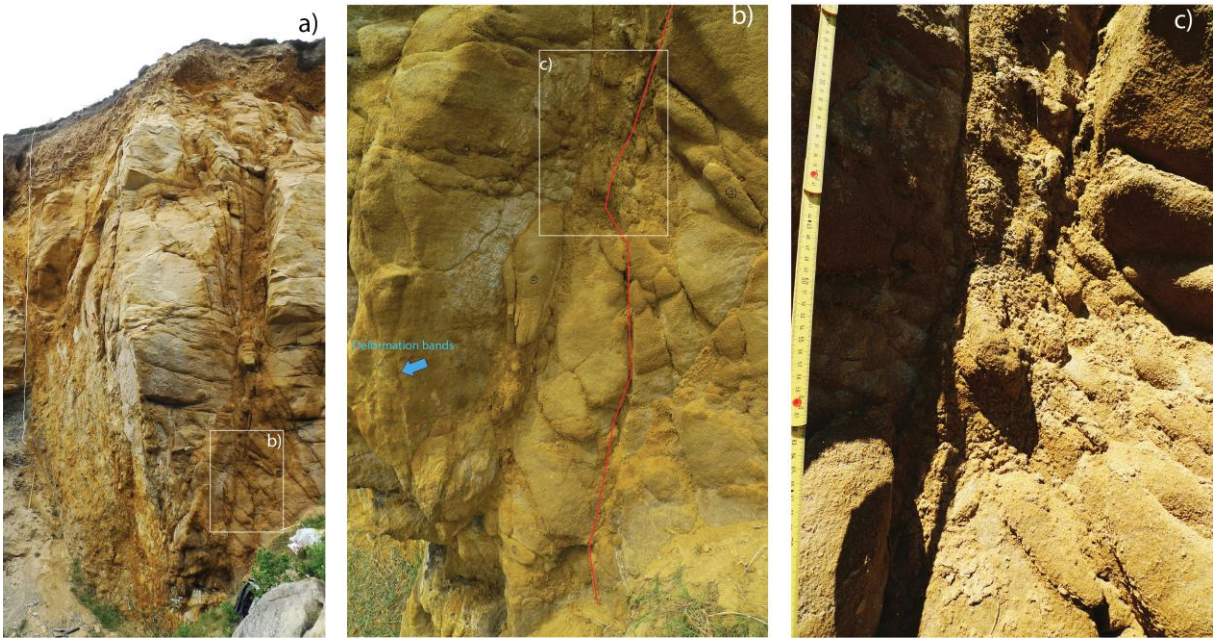

Figure 3.2. 7 Pictures of hanging wall master branchline
a) overview of Crag Point Fault core (see backpack for scale).
b) Small lenses as part of a proto-cataclasite Picture is about 2m high.
c) 3 slip surfaces towards top of picture and proto-cataclasite near the bottom (see meterstick for scale).

The largest lens (lens one) has a sub-vertical *c*-axis and is a central feature in the core (figure 3.2.6). In its lower parts the northern boundary is made up of slip surfaces close to the hanging wall master branchline and in the upper part consists of fractures radiating from the master branchline. The southern boundary consists of slip surfaces that, in the lower part separate the lens from breccia and in the upper part from another lens (lens two figure 3.2.6). Lens one has a prismatic shape with four sides. There are some fractures present in the lens mostly in the northern side radiating from the hanging wall master branchline. It has some deformation bands, particularly on its southern side. The lens consists of relatively undeformed sandstone derived from the hanging wall. Lens two (figure 3.2.6) is only partially exposed in our outcrop, where 5m*1,5m is visible. Only a minimum estimate for its size can be given because less than half of the lens is visible. Lens two is more fractured than lens one, with an evenly distributed open network of discrete fractures. Lens two is bounded on both sides by slip surfaces, which on the south side coincide with the footwall master branchline. The lower tip of the lens is characterized by proto-cataclasite of rounded clasts and several slip surfaces similar to the lower part of the northern Crag Point Fault core boundary. Towards the tip-edges there is a fully developed cataclasite with smaller and more angular clasts.

The difference in strike on the footwall and hanging wall master branchlines suggest that there is a variance in width along strike, widening west and thinning east (figure 3.2.5). This strike difference may reflect branchline undulations representing a lens on 100m scale, thus being larger than our window of observation**.**

Fault rocks

The cluster of small lenses near the hanging wall master branchline (figure 3.2.7b) is fractured into progressively smaller pieces constituting a proto-cataclasite (figure 3.2.7c). These lenses remain *in situ* and there is no indication that cohesion has been lost.

Close to the footwall master branchline there are several breccia bodies separated by slip surfaces with fault gouge or coal membranes. Some slip surfaces are observed to be filled with hematite mineralisation. In table 3.2.1 the breccia bodies have been numbered from one to six, where number one is closest to Lens one and number six is closest to the footwall master branchline. It is not entirely clear whether cohesion was obtained during deformation or indurated later. From field observations it looks as if the breccia bodies have a dominance

of fine grained matrix produced during faulting opposed to crystalline cement, further mineral studies need to be done to determine degree of cementation (appendix A). The breccias are very brittle making sampling difficult as they tend to disintegrate which suggests a low degree of cohesion.

Figure 3.2.8-1 shows part of a membrane at the bounding surface between breccia six and the footwall. The membrane mainly consists of clay. From the preserved part it seems that the membrane is continuous over most of the matrix but discontinuous where there are clasts. It is impossible to say whether this is due to recent erosion or if it is a primary quality of the membrane. Similar gouge material was found when sampling other breccia boundaries (figure 3.2.8-2).

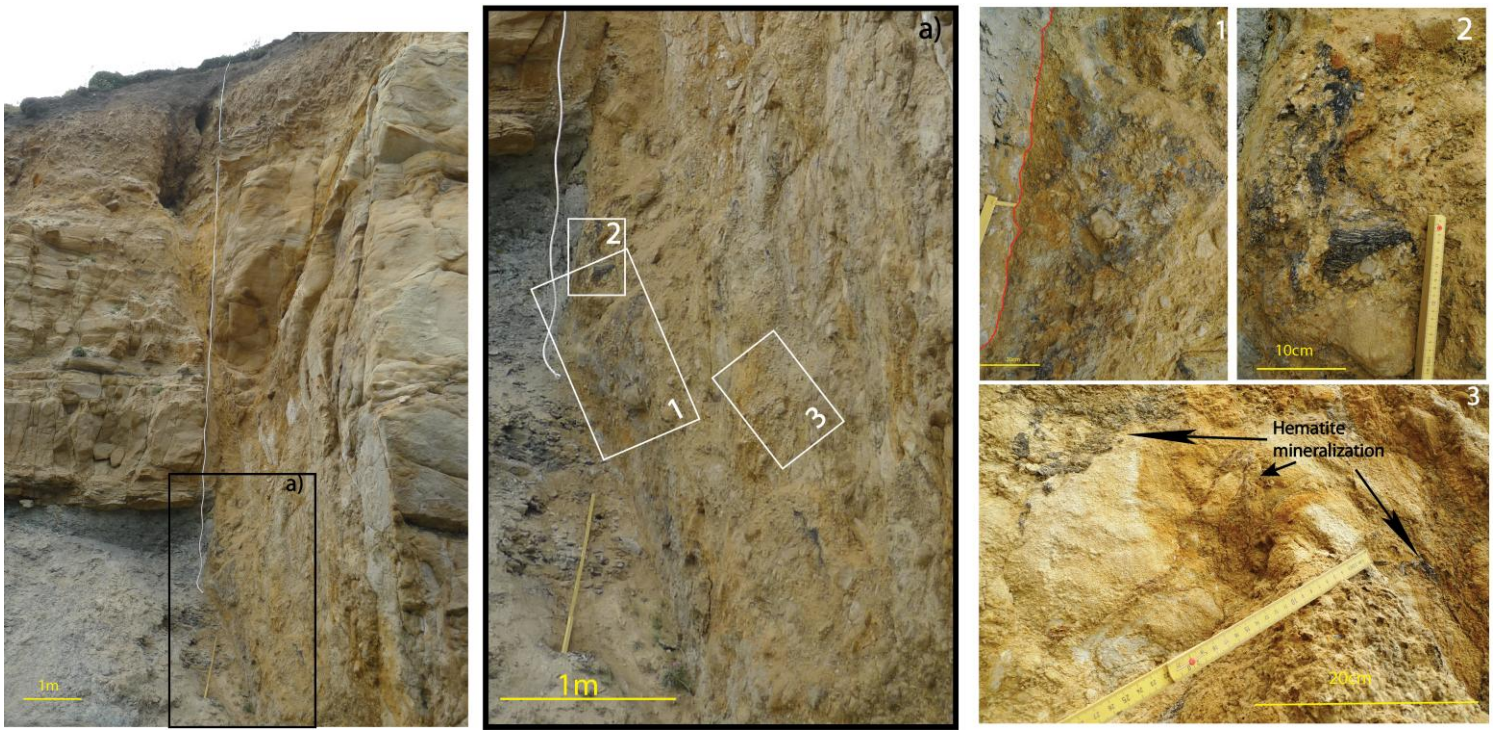

Figure 3.2. 8 Picture taken along the footwall master branchline. figure
a) displays a close up of an area with several breccias. Picture 1 to 3 show details from the breccia-layers;
Picture 1: Breccia 7 with clay membrane at footwall master branchline (red line marks footwall master branchline).
Picture 2: detail of coal bearing strata that has been incorporated into a breccia
Picture 3: Hematite mineralization at slip surface between breccia 1 and breccia 2.

Breccia #	Roundness clasts	Largest clast	N	Median clast	Composition Clasts	Composition matrix	%matrix (clast/matrix supported)	Breccia class (Mort and Woodcock 2008)	Description
1	Rounded Lensshaped	20*18	4	19*13	Medium sandstone	Medium sandstone	<10% (clast supported)	Crackle breccia	Can probably be argued that it is a lens with dimensions of 130*20cm. Larger clasts towards lens 1. Hematite mineralization towards lens one.
2			0		Medium sandstone	Several small (2mm) quartz grains interbedded in medium sandstone	>70% (matrix supported)	Chaotic breccia	The eroded surface has a rusty-red colour. (out of measuring reach)
3	Rounded	20*14	10	10*7	Sandstone	Sandstone	70-80% (matrix supported)	Chaotic breccia-cataclasite	Thin breccia-layer. (Figure 3.2.9) Coal striations on slip surface between #3 and #4 Pitch 34°NE Strike 253° Dip 80°
4	Rounded-subangular	20*15	15	15*5	Sandstone	Sandstone (with pebbles (mm size) near #3)	From 15-30% (clast supported) near #3 to 70-75% near #5	Mosaic breccia	Increasing degree of clasts, angularity and pebble content in matrix towards breccia#3
5	Rounded	15*10	8	9*8	Medium grained sandstone	Medium Sandstone with pebbles (mm size)	60% (matrix supported)	Chaotic breccia	Several clasts show indication of fractionation (figure 3.2.10)
6	subangular	18*7	6	11*6	Medium sandstone	Pebbles up to 1cm in size	85-90% (matrix supported)	Cataclasite	Quite well cemented (see appendix), white erosional surface. Coal –striations towards footwall pitch 38°NE Strike 79° dip 87°

Table 3..1 Breccias near footwall master branchline Crag Point Fault. N is number of clasts measured, clasts are measured in cm. # refers to breccia

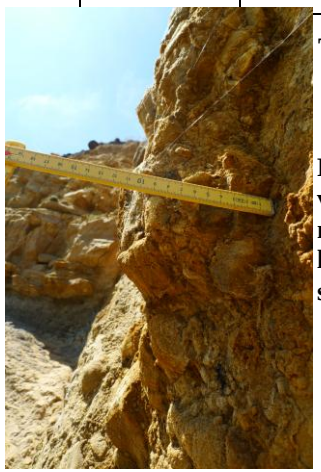

Figure 3.2. 9 Breccia 3 viewed along footwall master branchline towards land (see meterstrick for scale)

Figure 3.2.10 Fractured clasts within breccia 5

Fracture systems

There are fractures several places within the core, which can be sorted related to where they are: fractures near the master branchlines (h w 63/79 f w 266/86), along the lens margins and inside lenses. Fractures along the master branchlines and lenses tend to be shear fractures whereas tensile fractures are present in breccias described in table 3.1, inside lenses and in the proto-cataclasite close to the lower part of the hanging wall master branchline. Figure 3.2.10 show clasts inside breccia 5 containing tensile fractures. Figure 3.2.8 shows the proto-cataclasite where there are tensile fractures as well as slip surfaces.

The most evident shear fractures inside the core are the ones close to the footwall where there are slip surfaces between the brecciated layers. Figure 3.2.11 shows field measurements taken from the two slip surfaces closest to the master branchline with an average direction of 89/87. Figure 3.2.12 shows measurements extracted from LiDAR scans, generally a bit further into the core than figure with an average direction of 206/90.

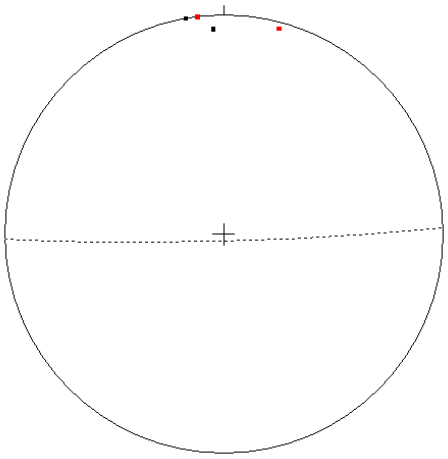

Figure 3.2.11 Field measurements of slip surface between breccia 5 and 6 in black and between breccia 5 and 4 in red
No. of Data = 4
Mean Principal Orientation = 89/87

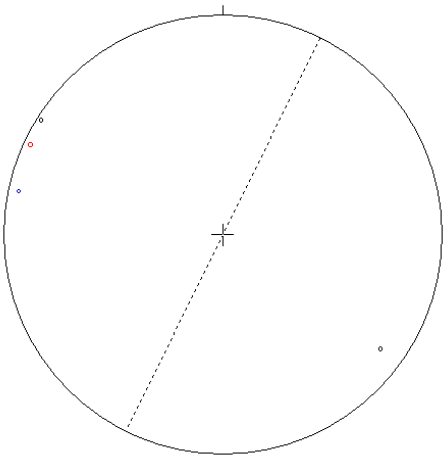

Figure 3.2.12 Measurements made from Lidar scans from the Crag Point Fault core on slip surfaces close to the footwall mostly taken from surfaces too high to reach in the field.
Red point between breccia 5 and 4
Blue point between breccia 4 and 3.
Black point between breccia 3 and 2
No. of Data = 4
Mean Principal Orientation = 206/90

Close to the hanging wall measurements were made using LiDAR on several fracture surfaces that are radiating from the master branchline (figure 3.2.13, figure 3.2.6 and figure 3.2.7c). These are steeper than the master branchline with an average 90^{o} dip compared to 79^{o} for the

master branchline. The fractures are oriented in an average 20 NNE direction, 40 degrees more to the north compared to the hanging wall master branchline.

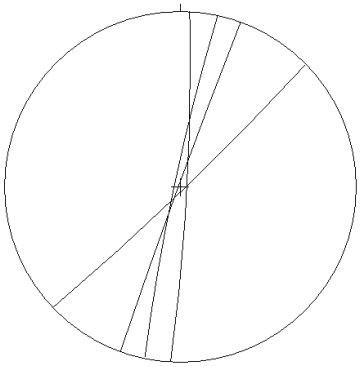

Figure 3.2.13 fractures measured with Lidar close to hanging wall master branchline
No. of Data = 4
Mean Principal Orientation = 20/90

Measurements around lenses within the core reveal 3 main distinct directions (figure 3.2.14). The mean trend was in an E-W direction. 11,7% were trending between 075-080^{o}E similar to that of the master branchlines which had an orientation of 79^{o}E for the Crag Point Fault, 8,9% were trending between 035-040^{o}NE. Consequently the most dominant direction was 10^{o} more to the east compared to the average direction of the main fault.

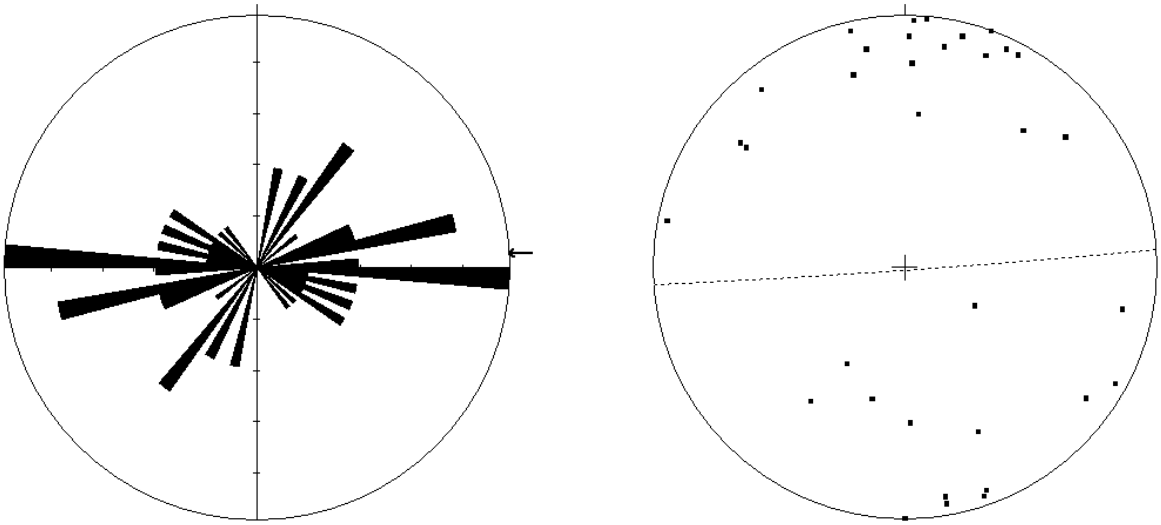

Figure 3.2.14 Measurements on lens boundaries from the core of Crag Point Fault. Three distinct trends which contain respectively 14,7%, 11,7% and 8,9% of the measurements (se below for directions)
No. of Data = 34
Mean Principal Orientation = 86/89
Sector angle = 5°
Scale: tick interval = 3% [1,0 data]
Maximum = 14,7% [5 data]
Mean Resultant dir'n = 087-267
11,7% = 075.-080 [4 data]
8,9% = 035-040 [3 data]

The fractures near the footwall are on average steeper that the ones near the hanging wall. They are striking in more or less the same direction, with exception of the field measurements close to the footwall. The measurements from the lens boundaries are more variable in trend compared to the other fracture measurements in the core. The lens measurements are directed more towards the east compared to the average fracture measurements.

Some of the slip surfaces have sign of mineralization of calcite or hematite. The hematite was observed on slip surfaces between breccias (figure 3.2.8-3), whereas the calcite was at slip surfaces where the breccia had been eroded. This suggests that the hematite mineralization is more erodible than the calcite and that more hematite may have been present at previous times. None of the mineralization has been observed cutting any layers or each other. Both the calcite and hematite are only found along dip on slip surfaces and only along very deformed (breccia) fault rocks.

Hanging wall

The hanging wall of the main fault has for the proximal 17m no subsidiary faults. From thereon it is a 100m wide horst and graben system to be described in its own section. The proximal part of the hanging wall is characterized by its high fracture frequency.

Fractures

In order to investigate fracture frequency, statistical data was gathered from the fractures in the area between the hanging wall master branchline and the horst and graben system to get an impression of the fracture frequency. Two fracture diagrams were made representing different levels in the upper Crag Point sandstone (figure 3.2.15). Both diagrams show a similar trend with an average fracture frequency for the proximal 17m at about 5fractures/m. It can be argued that the fracture frequency is increasing towards both the hanging wall and the horst and graben system with a decreased and lower fracture frequency 6-11m from the hanging wall. The lower of the two diagrams was continued into the southernmost graben of the horst and graben system displaying an increased fracture frequency within the graben.

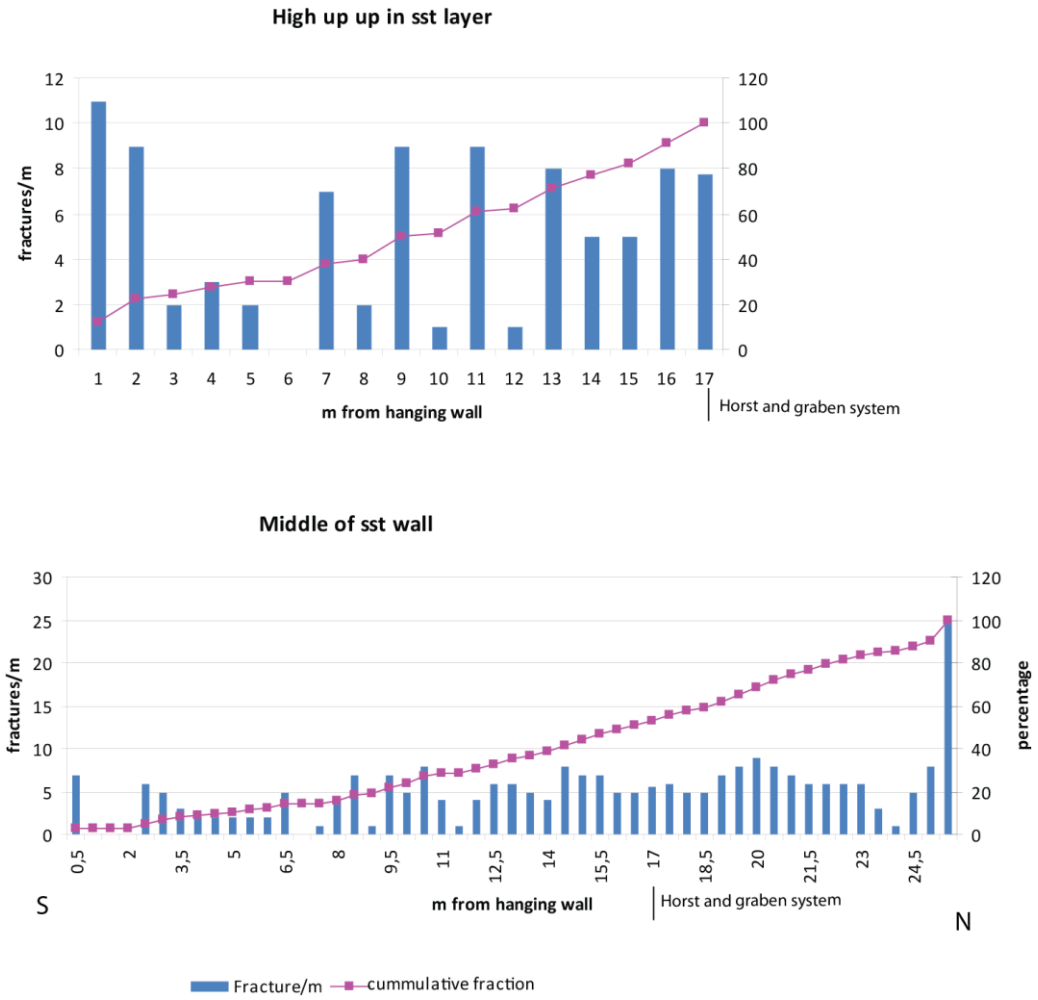

Figure 3.2.15 fracture frequency diagram from the hanging wall of Crag Point Fault

The fracture direction was on average 93/88E (figure 3.2.16), which makes the angle of 14^{o} east of the strike of the main faults orientation (figure 3.2.5). The dip of the fractures varies from 21^{o} to 90^{o} and the fractures are mainly striking east-west . 13% of the fractures are striking between 100-105^{o}E, whereas 9% are within a sector representing the main faults direction (figure 3.2.16).

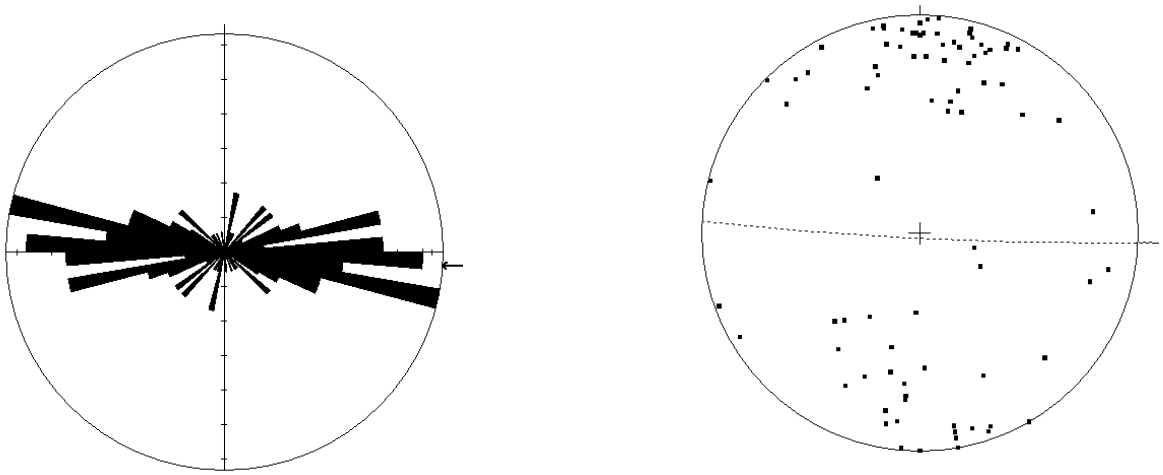

Figure 3.2. 16 fractures in the first 17m of Crag Point Fault hanging wall

No. of Data = 87

Mean Principal Orientation = 93/88

Sector angle = 5°

Scale: tick interval = 2% [1,7 data]

Maximum = 12,6% [11 data]

Mean Resultant dir'n = 093-273

11,6% = 090-095 [10 data]

9,2%= 085-090 [8 data]

9,2%= 075-080 [8 data]

Footwall

The footwall side of the main fault has several subsidiary faults, dipping both north and south (figure 3.2.17). This section first describes the general fracture distribution for the proximal 17m of footwall, similar to that of the hanging wall, followed by a description of some of the subsidiary faults.

Figure 3.2.17 Footwall side of main fault. See the footwall master branchline to the right in the picture. Blue lines mark southwards dipping slip surfaces and red northwards dipping slip surfaces

Fractures

One fracture diagram was made for the footwall area, where the fracture frequency was recorded from the Lower Craig Point Sandstone (figure 3.2.18). This shows a very high fracture frequency for the proximal four metres of about 20 fractures/meter. From thereon it is a much lower frequency of c.2fractures/meter as can be seen from the cumulative fraction that flattens.

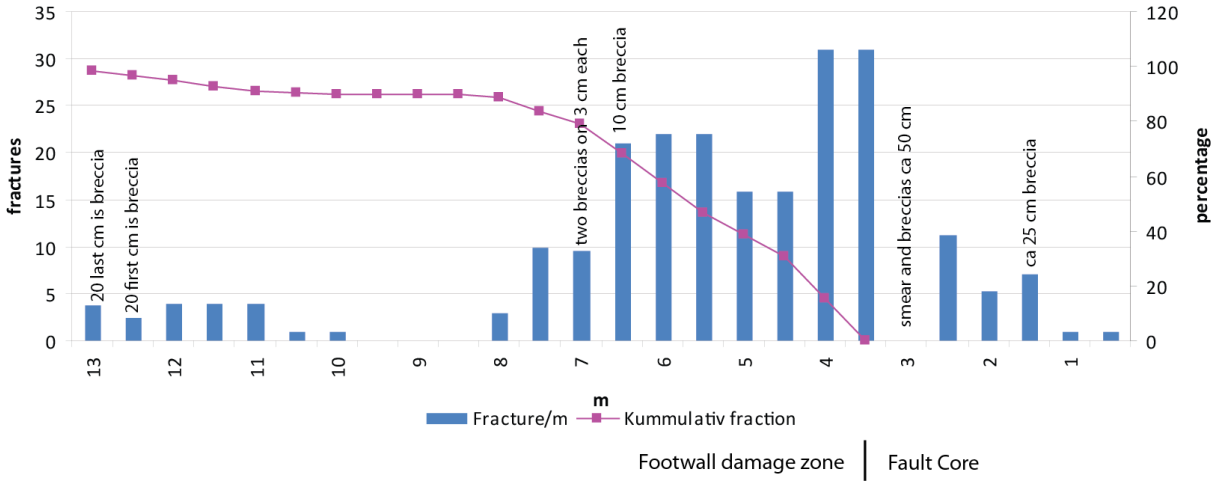

Figure 3.2.18 fracture frequency diagram from the footwall of Crag Point Fault

Fractures in the proximal 10m of the footwall have an average orientation of 87/88. This is a bit more to the east compared to the main faults orientation which is 79^{o}E (figure 3.2.19). Figure 3.2.19 show that most fractures are striking in an east-western direction with various degree of dip, varying from 12^{o} to 90^{o}. 12% of the fractures are in a sector with strike varying between 90-95^{o}E.

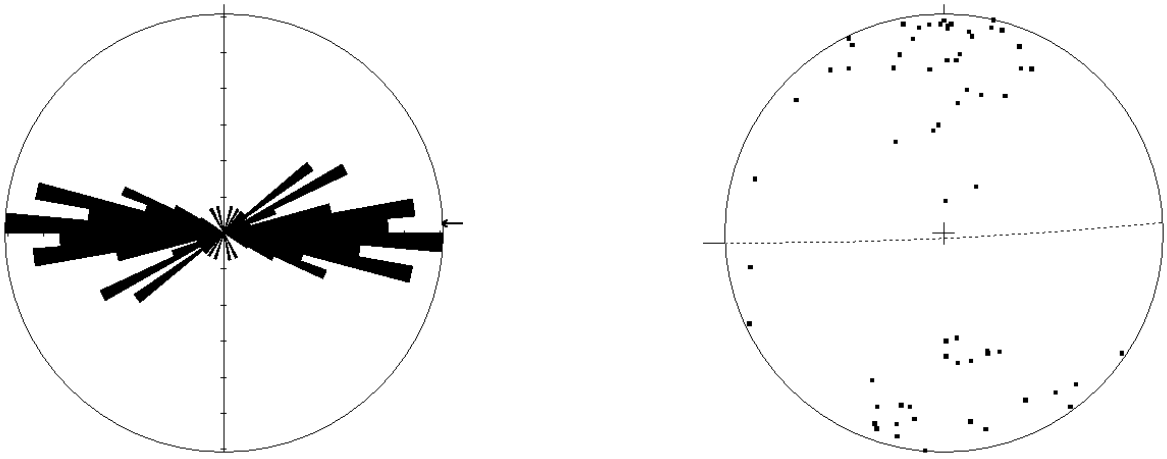

Figure 3.2.19 Fractures in the first 10m of Crag Point Fault footwall
No. of Data = 66
Mean Principal Orientation = 87/88
Sector angle = 5°
Scale: tick interval = 2% [1,3 data]
Maximum = 12,1% [8 data]
Mean Resultant dir'n = 088-268
10,6%= 080-085 [7 data]
10,6%= 100-105 [7 data]
7,5%=060-065 [5 data]

Subsidiary faults- dipping south

The Lower Craig Point Sandstone has two slip surfaces just where the fracture frequency decreases (figure 3.217 and figure 3.2.18). The slip surfaces are spaced at 60cm, the one closest to the main fault has an offset towards south of 65cm whilst the other has a offset towards north of 5cm. The one dipping towards the south has developed cataclasite on the hanging wall side with some lenses in the lower parts of the outcrop. The lenses have a *c*-axis up to 80cm and show signs of being deformed with fractures dividing the lens into higher order lenses. The faults offset two coal bearing seams that are spaced 30cm apart in the sandstone sequence which function well as marker beds even for fractures with small slips.

The area between the two described slip surfaces is heavily deformed with several slip surfaces and breccia. It has several southerly dipping slip surfaces with vertical separation up to 4 cm (figure 3.2.20) and under the lower marker bed there is a loose breccia. The breccia is matrix supported (70-80%matrix) with a matrix consisting of silt mixed with coal fragments. There is some clay bands inside the breccia present along the outcrop from one fault to the other angular to the fault surfaces. The clasts (5) measured have varying degree of sphericity and roundness the largest is 8*3cm whilst the median size is 4*2cm.

The two slip surfaces can be viewed as one southerly dipping fault where the southerly dipping slip surface represent the footwall master branchline and the northerly dipping one the hanging wall master branchline. Several of the fractures in the core have hematite mineralization and some have both hematite and calcite. Figure 3.2.21 shows measurements from the two slip surfaces giving an average direction of 92/80 E. Notice that the footwall master branchline has three very variable measurements.

Figure 3.2.20 Fault core of subsidiary fault in the Lower Crag Point Sandstone . Slip surface to the right is the southerly dipping one and slip surface to the left is the northerly dipping one. The lowermost part of the core contains a breccia (see text for further description). Meterstick marks 1m.

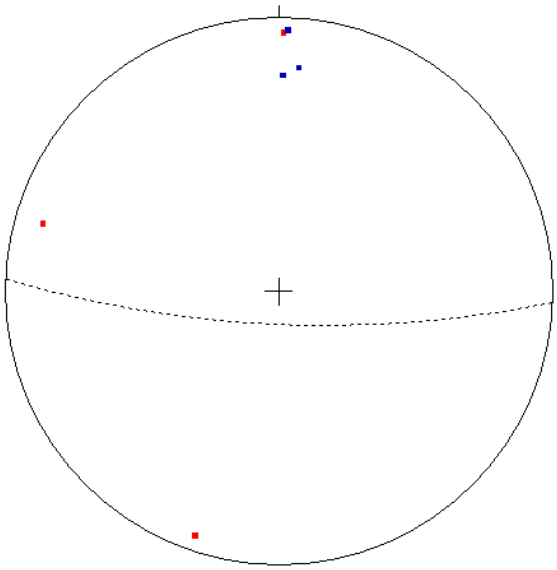

Figure 3.2.21 subsidiary fault Lower Crag Point sandstone. Blue points represent the southerly dipping slip surface and red lines the northerly dipping one
No. of Data = 6
Mean Principal Orientation = 92/80

Subsidiary faults-dipping north

The largest subsidiary fault can be traced both along the lower Crag Point sandstone and outcrops of the lower lying delta plain deposits where it is bounded to the Five Quarter Seam in the footwall (figure 3.2.22). It is a northerly dipping fault with vertical offset of 2m and orientation of 253/50 SSW (figure 3.2.22c). Measurements from the less competent upper delta plain rocks have a more gentle dip than the measurement from the lower Crag Point sandstone that has an orientation of 229/80 SSW. There are lenses on the hanging wall side of this slip surface both in the upper sandstone part of the outcrop(figure 3.2.22a) and in the lower interbedded siltstone outcrop (figure 3.2.22b), lens α, β and γ. Lens γ at the lower Crag Point sandstone is surrounded by breccia with silt, clay and patchy coal material in between. The breccia shows presence of calcite and hematite mineralization up to 3mm thick. Lens α and β in the upper delta plain deposits have no breccia along their boundaries. Lens β show an increasing degree of offset updip.

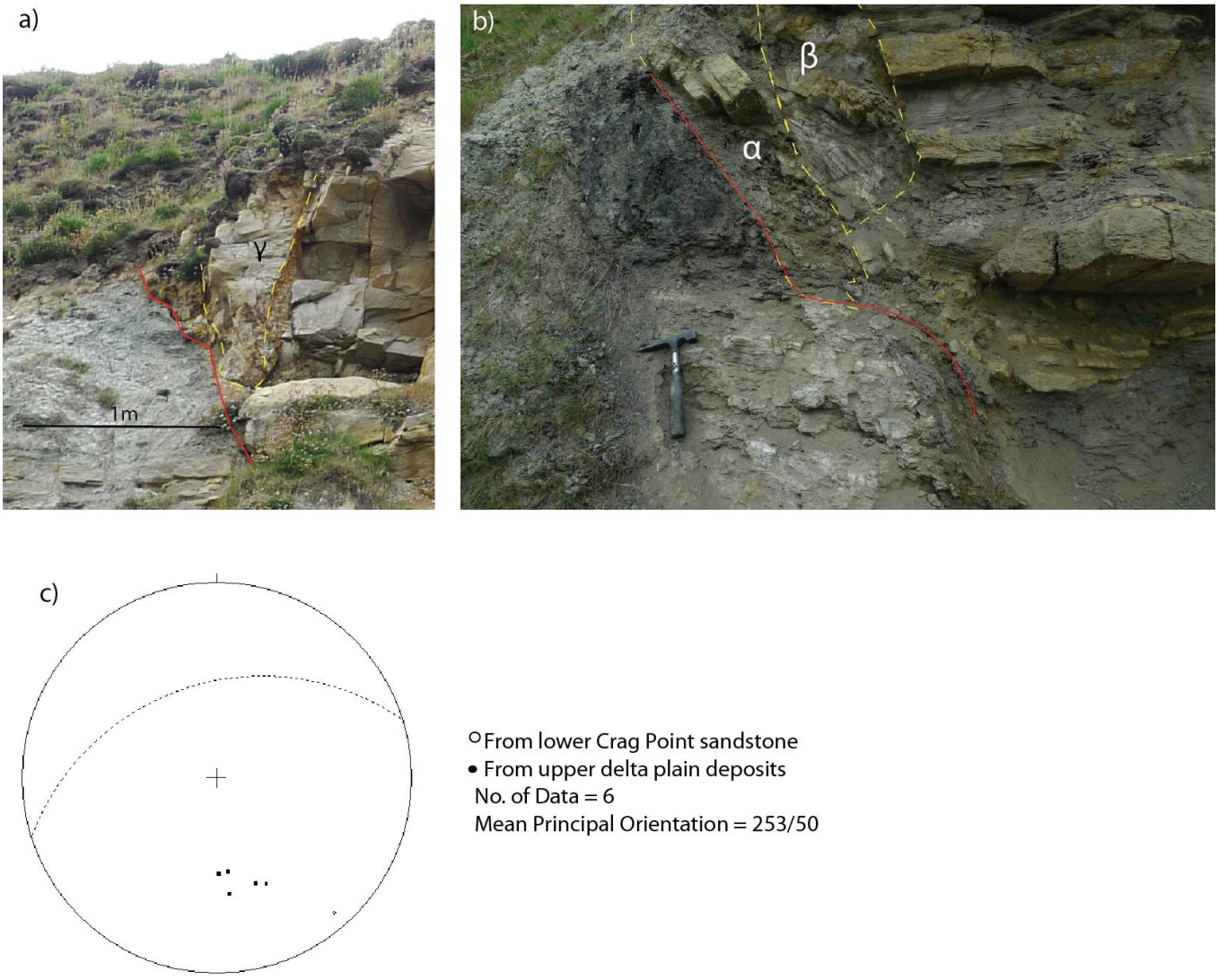

Figure 3.2.22 Subsidiary northerly dipping fault with a vertical separation of c.2m

a) fault trace cutting through Upper Crag Point Sandstone . Red line marks footwall master branchline. yellow lines mark the borders of lens γ

b) fault trace cutting through upper delta plain deposits juxtapositioning the Five Quarter Seam (on the footwall side. . Red line marks footwall master branchline. yellow lines mark the borders of lens α and β

c) Stereographic projection of field measurements taken along the footwall master branchline

On the northern side of the outcrop of upper delta plain deposits there is a northerly dipping fault with 15 cm vertical offset (figure3.2.23). The core widens down-dip and consists of fragments of the footwall. The orientation for this fault is on average 98/73 E, 25o more southerly directed in comparison to the nearby northerly dipping fault.

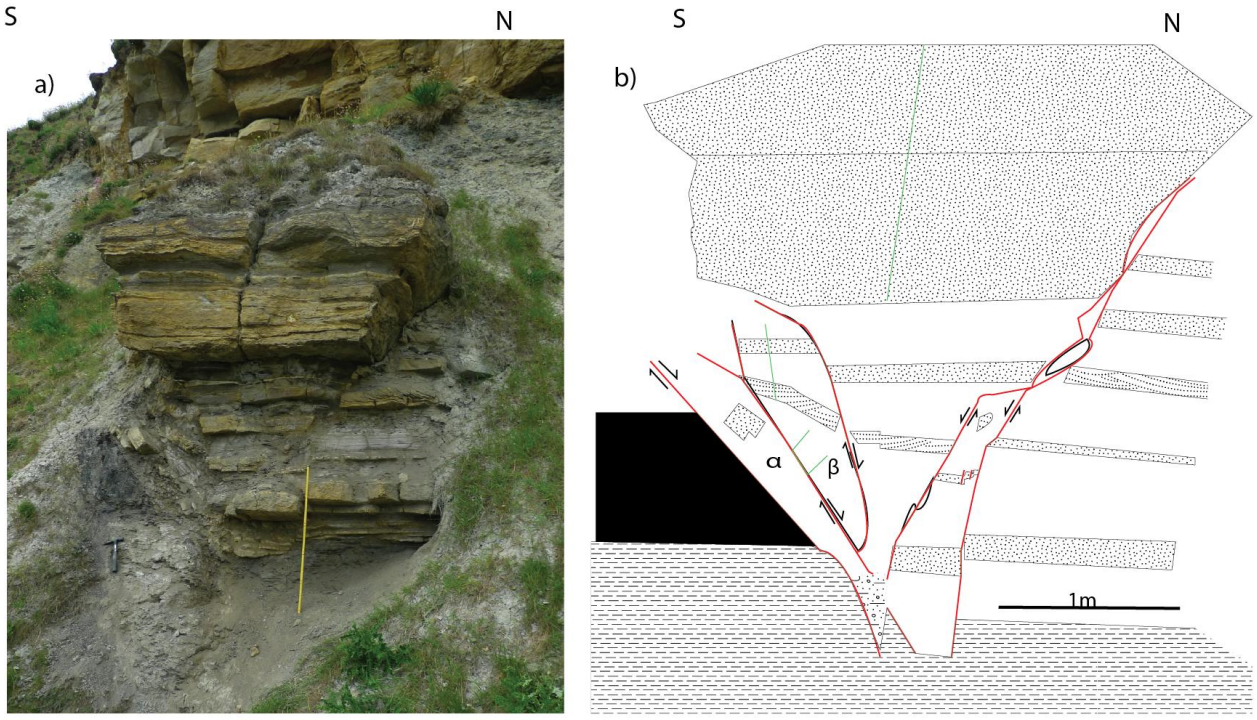

Figure 3.2.23 Outcrop of upper delta plain deposits on hanging wall side of the subsidiary fault pictured in figure 3.2.22.
a) photograph with 1m meterstick and hammer for scale
b)Sketch with red lines marking slip surfaces

3.2.2 Footwall graben

The graben is located about 20m south following the cliffs from the Crag Point Fault (figure 3.2.1 and figure 3.2.2). It offsets the upper delta plain deposits including the Five Quarter Seam. The Graben itself is 10m wide and is bounded by steep faults with a vertical separation of 0,7m and 1,1m. (figure 3.2.24).

The slip surfaces are both steep, average dip of 83^{o}, and the faults have an east westerly direction, average 93^{o}E (figure 3.2.25). Most measurements are taken at the southern fault and one at the northern one and they are all taken in similar stratigraphy of interbedded siltstone. Both graben faults are more eroded than surrounding rocks creating small caves in the cliff. This suggests less competent fault rocks compared to the surrounding siltstone. Both fault cores contain bodies of breccia

From figure 3.2.24 it seems as if the silty section above the Five Quarter Seam is not as faulted as the section below suggesting that deformation dies out up dip.

Figure 3.2.24 Graben in upper delta plain deposits south of Crag Point Fault

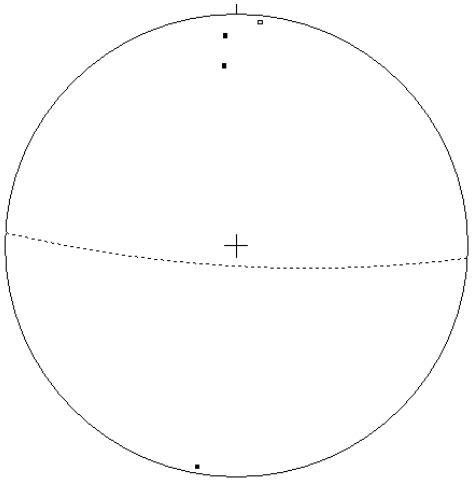

Figure 3.2.25 measurements along slip surfaces at graben offsetting upper delta plain strata
○ From southern fault (0,7m throw)
● From northern fault (1,1m throw)
No. of Data = 5
Mean Principal Orientation = 93/83

The fracture diagram from the graben (figure 2.2.26) shows a generally higher fracture frequency inside the graben compared to the sides. The graben has an average fracture frequency of 7fractures/m. The northern and southern side of the graben has a different fracture frequency development. The southern side has a lower and decreasing fracture frequency. The northern side has a relatively even fracture frequency that doesn't appear to be decreasing away from the graben. This could be because that the northern side of the graben is close to the Crag Point Fault and therefore being part of this damage zone. About 12 m from the southern fault the fracture frequency stabilizes at an average of 2fractures/m. Orientation

of the fractures in and around the graben (figure 3.2.27) is close to the orientation of the faults themselves (figure 3.2.25).

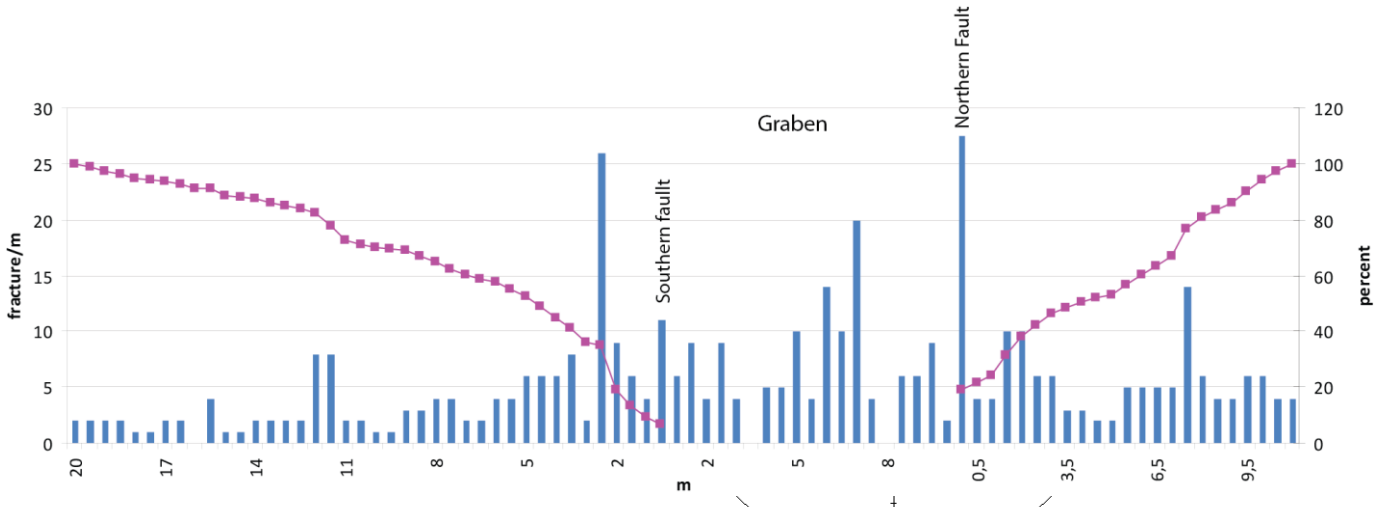

Figure 3.2.26 Fracture frequency diagram for the graben sounth of Crag Point Fault. Purple line marks cumulative fraction.

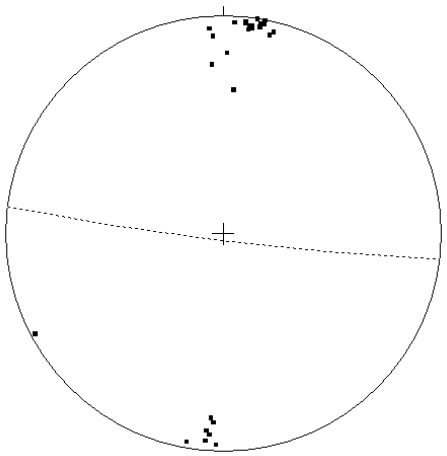

Figure 3.2.27 Stereographic projections of fractures close to and inside graben south of main fault
No. of Data = 29
Mean Principal Orientation = 97/87

3.2.3 Horst and Graben system

The horst and graben system (figure 3.2.28 and figure 3.2.29) is located on the hanging wall side of Crag Point Fault, where the nearest graben is 17m from the main fault. It is about 100 m wide and consists of 5 horsts confined by faults with vertical offset of less than a meter. In the following section the system is first described as a whole in relation to fracture frequency, fracture orientation and fault orientation. Then a closer look is taken at the southernmost graben and horst where mineralization also is described. LiDAR scans (figure 3.28) were taken of the system making measurement on fault surfaces and large fracture systems much easier.

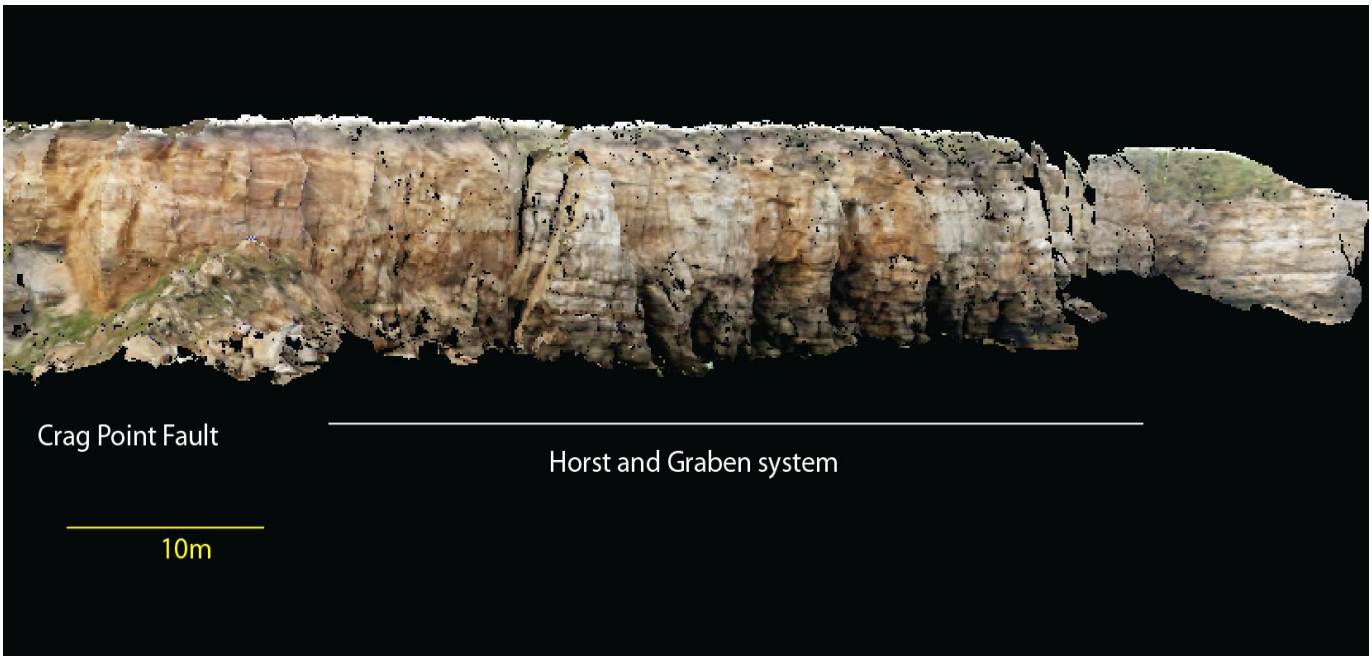

Figure 3.2. 28 Lidar scans from Crag Point showing both the main fault and the horst and graben system on the hanging wall side (see appendix B for larger figure)

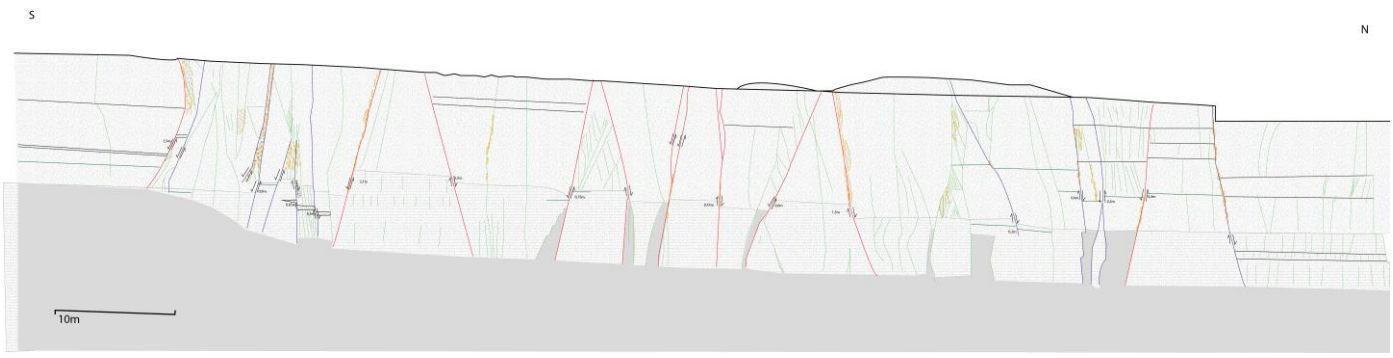

Figure 3.2.29 Field sketch of horst and graben system north of the main fault, Crag Point (see appendix B for larger figure)

There was made a fracture frequency diagram (figure 3.2.30) across the horst and graben system from the southernmost graben and 41m past the last fault recorded (figure 3.2.29) where the recordings was ended at a large cave. The exact width of the system from the southernmost to northernmost recorded fault is 78m. North of the last recorded fault there were a couple of surfaces with the appearance of fault surfaces but no slip was identified and they are owing to this not presented.

The fracture frequency is relatively even within the system of a fracture frequency of about 5fractures/m. The frequency decreases after the northernmost fault in the system before it is increasing towards the cave at the northernmost part of the diagram. From figure 3.2.30 one can also observe that there is more breccia present in the southern part of the horst and graben system. This fits well with the visual impression from the field site where especially the southernmost graben looked more deformed than the others. The grabens have an overall fracture frequency of circa 5fractures/m. The fracture frequency has a decreasing trend northward in the system from 6 to 4 whilst overall variability increases. The fracture frequencies in the horsts are of about 4fractures/m throughout the system. Thus there is a difference in fracture frequencies in the grabens and horsts but the difference is less clear northwards in the system.

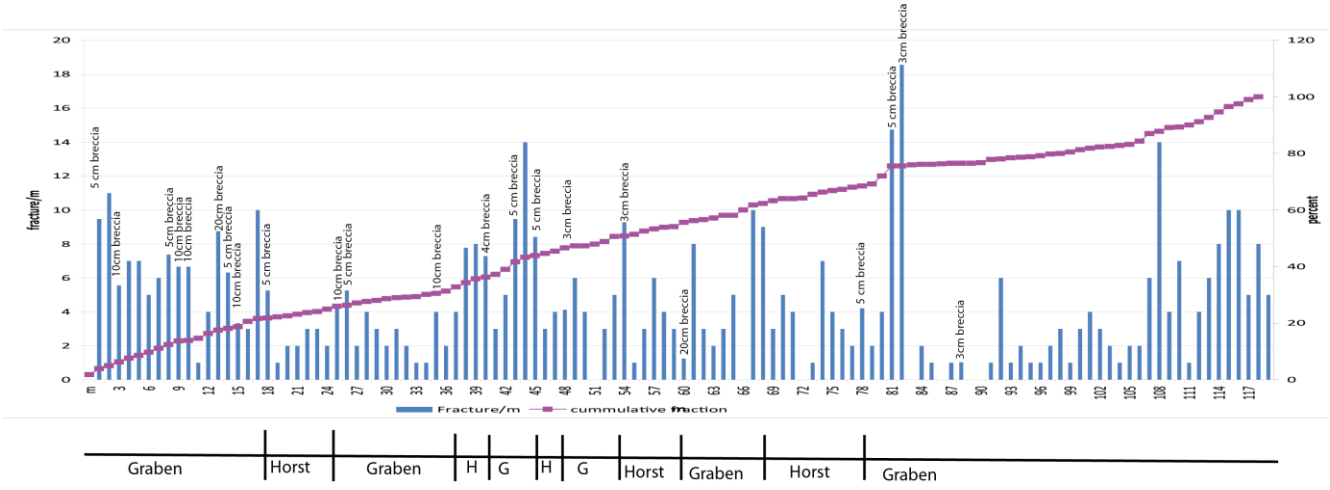

Figure 3.2.30 Fracture diagram across horst and graben system, Crab Point. Fractures counted in bottom of the Upper Crag Point Sandstone.

Figure 3.2.31a show orientations of all fractures measured within the horst and graben system. Overall the dip of the fractures varies from 59^{o} to 90^{o}, with an average of 89^{o}. Fractures within the system are striking in an E-W direction (269^{o}W). The measurements made from the LiDAR scans show a more northerly trend, with a mean principal direction of 38/86NE,

compared to the field measurements that has an average orientation of 269/89W. The measurements made from the LiDAR scans are taken at exposures high up and represent larger surfaces compared to the field measurements.

The faults forming horsts and grabens are varying in vertical offset from 0,2m to 1,5m, where all but one has vertical offset less than a meter. The average orientation for the faults is 267/88W, similar to the overall fracture orientation (figure 3.2.31).The rose diagrams are also similar showing a NE-SW sector representing the data collected from the LiDAR scans.

Fractures horst and graben system north of main fault, Crag Point

a) All fractures within horst and graben system

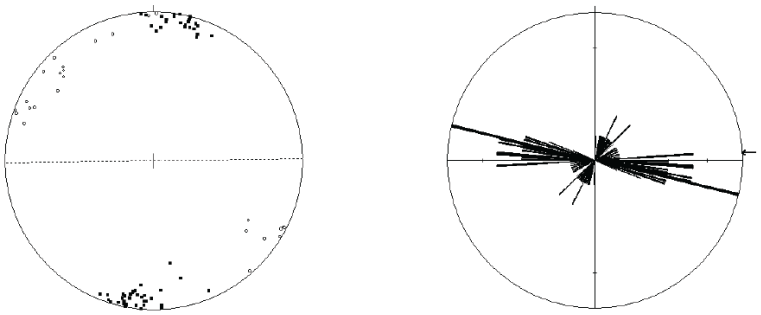

○ Measurements made from Lidar scans
• From field measurements
No. of Data = 87
Mean Principal Orientation = 269/89
The rose diagram show that 6,9% of the data are striking 103E-283W.
4,6% are of the data are striking 94E-274E.
4,6% of the data are striking 85E-265W

b) Slip surfaces belonging to horst and graben forming faults

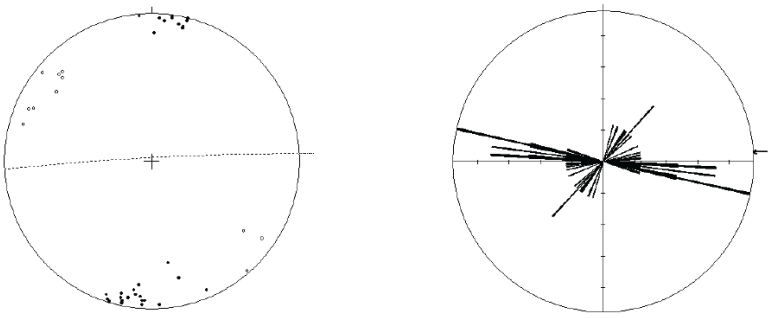

○ Measurements made from Lidar scans
• From field measurements
No. of Data = 42
Mean Principal Orientation = 267/88
The rose diagram show that 9,5% [5 data points] of the data are striking 102E-282W
7,1% of the data are striking 97E-277W [3 data]
7,1% of the data are striking 94E-274W [3 data]
4,7% the data are striking 42NE-227SW [2 data]

Figure 3.2.31 Stereographic projections from fracture surfaces within the horst and graben system

Figure 3.2.32 show the distribution of fractures, deformation bands and cm of breccia in the southernmost graben and horst thus giving a good indication of degree of deformation. When the three different features are viewed together it appears as if the overall deformation is more even within the graben than if only the fracture frequency is taken into consideration. In the horst the amount of deformation bands appears to be high when the fracture frequency is high thereby amplifying the peaks. The breccia distribution shows that it is breccia present only in the southernmost graben. This could suggest that the grabens are the only area within the system which are deformed to a degree at which brecciation occurs which is also the case in figure showing the whole system (figure 3.2.30). It can also be an indication that the southernmost graben is more deformed than the rest of the system which was the visual impression during fieldwork.

There are several fractures with mineralization within the system. Calcite, hematite and manganese oxide are the types of mineralization found. The mineralization was of thickness up to 3cm where the calcite formed the thickest layers. Figure 3.2.32 is a fracture diagram for the southernmost graben and horst showing additional information of mineralization. In average a third of the fractures in that area had some degree of mineralization. The areas with a high fracture frequency are also the areas with high degree of mineralization. Most of the mineralized fractures in Figure 3.2.33 had hematite in them and half had calcite in them whereas 1/6 had manganese oxide.

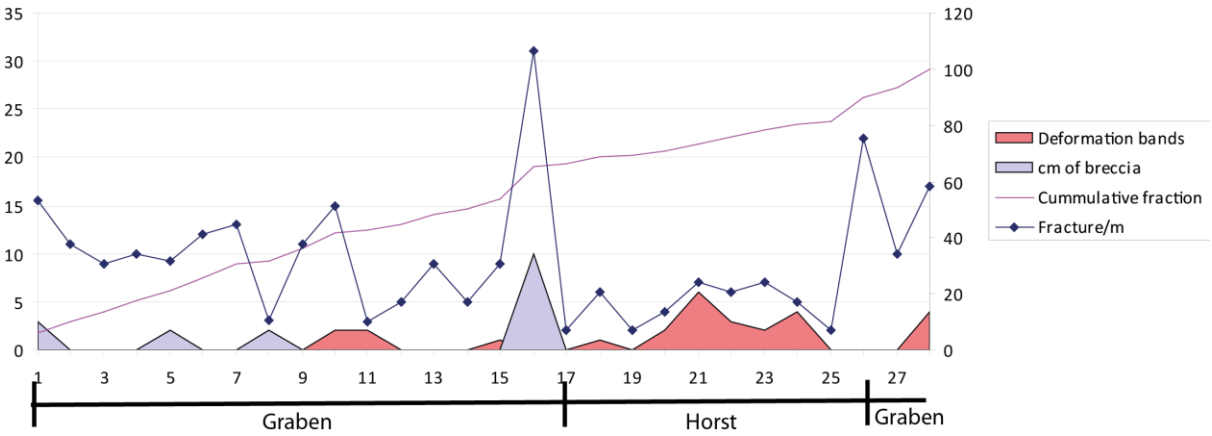

Figure 3.2.32 Fracture diagram southernmost graben and horst in horst and graben system Crag Point. Recordings taken in different lithologies in walking height

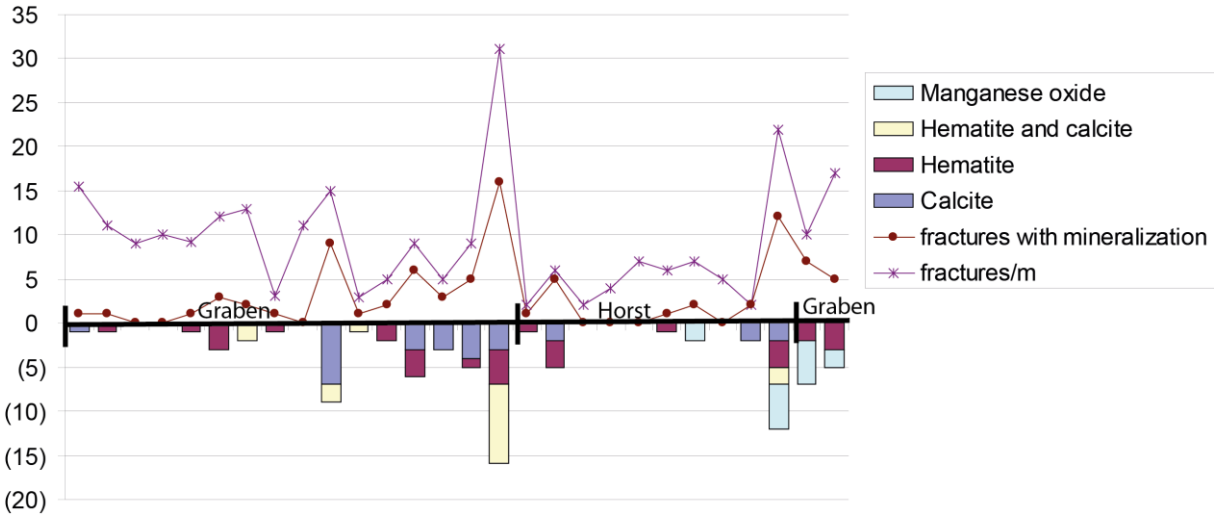

Figure 3.2.33 Fracture diagram southernmost graben and horst in horst and graben system Crag Point. Showing degree of mineralization present in fractures. The bar below the x-axis show amount of different type of mineralization. Recordings taken in different lithologies in walking height.

3.2.4 Overall characteristics of Crag Point

Crag Point Fault is an oblique fault with the majority of slip accommodated in the horizontal component (14m compared to 11m in vertical offset). Most of the vertical offset is accommodated at the footwall side of the fault core where there are most slip surfaces. The hanging wall master branchline has a vertical offset in the opposite direction (south). This gives a deformation structure where the fault core acts as a negative flower structure with downfaulting from both sides. The inequality in vertical offset at the two sides of the fault, 11m compared to 0,55m, gives it an appearance of an oblique fault.

Most of the subsidiary faults are situated in the footwall side of the nearby damage zone. The largest of these subsidiaries has an orientation (253/50) similar to the main fault (79/89). The strike of the subsidiary fault is 6^{o} more towards north in comparison to the main fault. (79/89) The difference in dip gradient is evident as the subsidiary fault has a more gentle dip compared to the main fault.

Fractures in the damage zone were mainly measured in the lower Crag Point sandstone on the footwall side and in the upper Crag Point sandstone on the hanging wall side. The near hanging wall has an average fracture frequency of *c.*5fractures/m whilst the near footwall has *c.*10fractures/m.Competence difference in the damage zones, as well as the very high fracture frequency for the proximal 4m of the footwall damage zone contributes to the frequency

difference. The average directions for the fractures in the footwall (87/88) are 6^{o} more northerly compared to the fractures in the hanging wall (93/88).

Measurements were made at a selection of lenses at Crag Point, but not as many as at Snab Point. The difference in lens quantity is due to the limited exposure of the main fault at Crag Point compared to Snab Point. The lenses at Crag Point are measured along dip giving length-thickness relations(*c*:*a*). Length(dip)-thickness relations for lenses at Crag Point are given in figure . The lenses are recorded in the Crag Point Fault core and some in the footwall damage zone. In figure 3.2.34 the largest lens (lens one) is disregarded since it is an outlier compared to the other measurements and thereby will skew in the statistical data. Thicknesses vary from 0,06m to 1,50m and length from 0,15m to 2,00m. The best fit regression line is the exponential trend with a confidence factor of 0,85. Using the power law equation with a confidence factor of 0,71 to calculate we get a *c*:*a* ratio of 3:1.

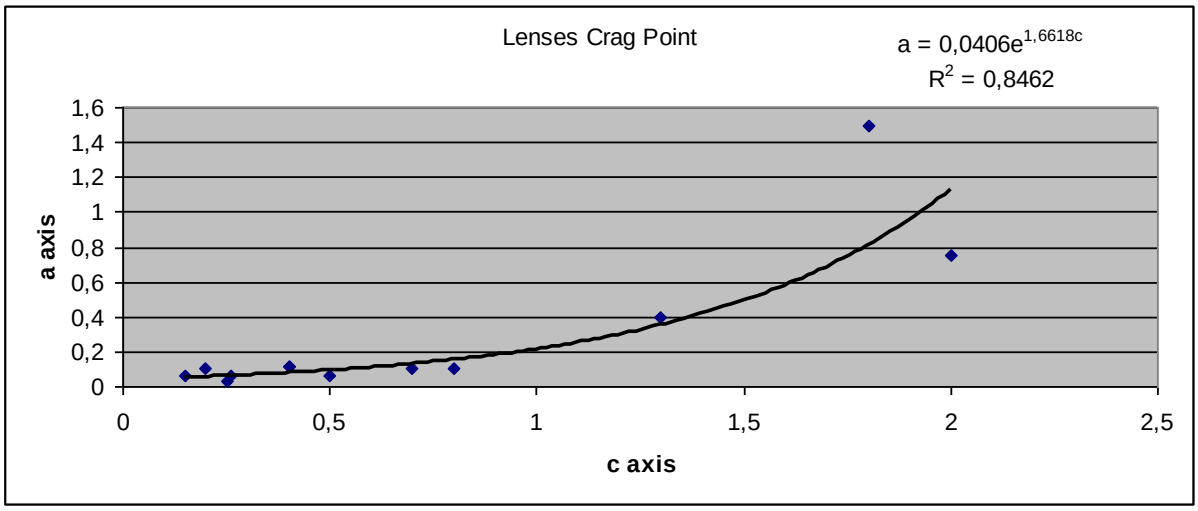

Figure 3.2.34 Lens data for Crag Point fault zone
N=12.

Overall characteristics of structures on North and South side of the Crag Point Fault

The north side of Crag Point Fault is characterized by deformation in sandstones whereas the south side has deformation structures in mixed lithologies. The fractures and faults are steep and generally trending in an E-W direction. Deviations to this dominating trend is found in fractures near the hanging wall master branchline and in fractures measured from LiDAR in the horst and graben system. The fracture frequency is generally higher on the southern side of Crag Point Fault. This variation could be due to lithological differences as there are less competent and thinner beds on the southern side (Heynekamp et al. 1999).

It is not clear whether any of the graben structures at Crag Point are secondary structures to Crag Point Fault itself and thereby are part of the Crag Point Fault zone. They could have formed independently simultaneous with or without activation of the Crag Point Fault both before and after the formation of Crag Point Fault. All orientations measured at Crag Point have an average overall direction varying between E-W and NE-SW within a reasonable variation for one deformation mechanism. The orientations for the Crag Point Fault have more measurements in a NNE direction whereas measurements from both the southern graben and the northern horst and graben system were dominantly E-W. This could suggest that the grabens are independent structures and not part of the Crag Point fault zone. The horst and graben system is located between the Crag Point Fault and the significantly larger fault with 52m vertical southern dipping offset north of the system(Jones 1968). The area between these faults might have been weakened and thereby prone to deformation.

4. Discussion

The foremost scientific aim of this thesis is to study the architecture, fault facies and properties of two fault systems exhibiting sand-sand juxtaposition by detailed description and analysis. Subsequently the faults steep geometry and their relation to the regional setting are studied and seen in relation to the fault architecture (section 1.1).

In the following the tectonic significance will be discussed before the main interest of this study, the fault architecture is discussed. The final part of the discussion deals with the status of the faults in relation to the regional development as known from the literature

4.1 Tectonic significance of the Snab Point and Crag Point faults

The faults at Snab Point and Crag Point displace sediments of similar age and lithology, juxtaposing fluvial sandstone beds within the Coal Measures. The main faults in the two localities have similar vertical separations (9m and 11m for Snab Point and Crag Point). Both faults are very steep to subvertical and strike ENE-WSW. The main fault segments at Snab Point strikes slightly more northerly (45/85 and 66/79) compared to the fault at Crag Point (79/89). Both faults display some degree of mineralization, dominantly calcite with subordinate hematite and occasionally manganese oxide. Mineralization is most prominent in the horst and graben system at Crag Point.

The main differences between the two main fault zones discussed are the following: The main fault at Crag Point has more subsidiary deformation structures on its footwall side, where several small faults are present, while at Snab Point there is a subsidiary fault (segment 2) on the hanging wall side. The main fault at Snab Point is likely to represent a subsidiary fault to the larger fault 3 which has a vertical displacement of 21m (section 3.1.5). At Crag Point oblique slickenlines associated with the master fault planes indicating a significant horizontal component with a mean pitch of 36^{o} (section 3.1.5). None such lineations indicative of oblique movement are found at Snab Point.

4.2.1 Geometries of the steeply dipping faults

The main faults at both localities are steeper than predicted by the Andersonian configuration for normal faults. There are several possible explanations for the faults to be sub-vertical where the geometry is a result of how the faults have been affected by regional processes, discussed in section 4.5. The following chapter deals with the steepness of the faults where the following explanations for this are proposed;

1) Normal faults initiated at a very shallow level
2) Normal faults developed in mechanically strong lithologies
3) Primarily strike-slip faults
4) Hanging wall migration during reactivation
5) Antithetic faults developed over a larger fault

Normal faults initiated at a very shallow level

Steepness of the faults could suggest shallow burial, as faults close to the surface are very steep the upper tens of metres where pressure is low (Jackson and McKenzie 1983). Surface traces of modern tectonic outcrops show a much steeper dip angle than the subsurface continuation of these (figure 4.1). In the Aegan region of northern Greece this is observed for fault segments cutting quaternary surface deposits (Jackson et al. 1982, Jackson and McKenzie 1983, Stewart and Hancock 1991). Near the surface there is a lack of tension and thus open vertical fractures are likely to form. The steep surface segments of the Aegan faults are hard linked with considerably lower angle faults in depth (Jackson and McKenzie 1983). If this model is correct, it implies that the actual sections of the faults investigated by me were at a very shallow level of burial where the pressure is low probably initiates with less than 100-50m of overburden. Faults formed at shallow depths or within high fluid pressure may result in failure angles that vary with lithology (Ferrill and Morris 2003).

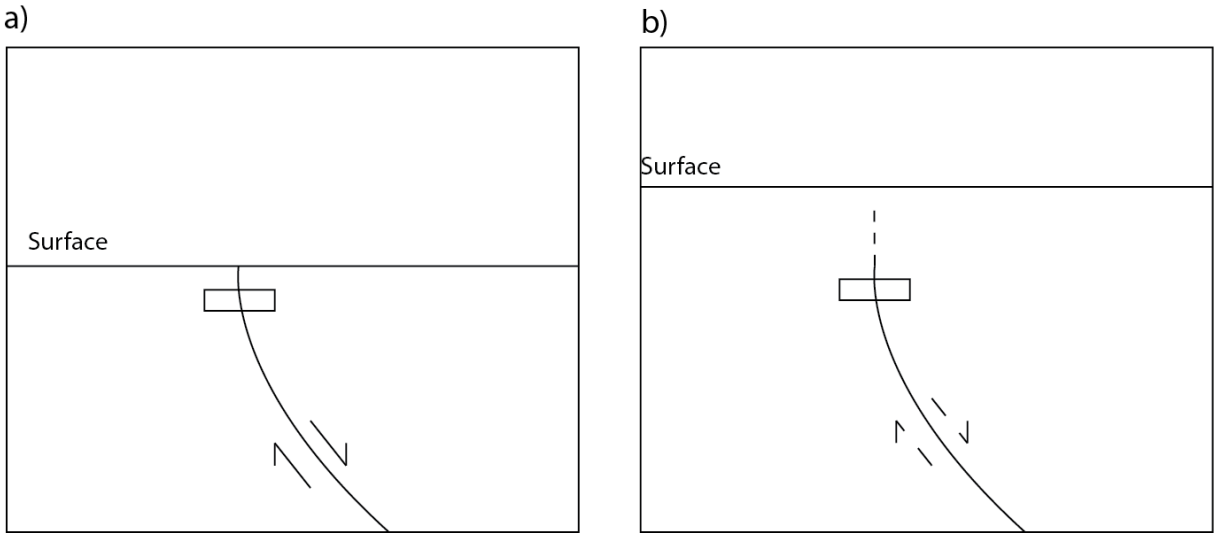

Figure 4. 1 how shallow burial might affect fault geometry. a) Shallow initiation of fault leading to a steep fault trace near the surface. b) the fault trace in (a) during continued burial. Little square marks our present day window of observation which displays steep fault traces at both Snab Point and Crag Point.

Normal faults developed in mechanically strong lithologies

The faults at Crag Point that are dominated by sandstone in both hanging wall and footwall are significantly steeper (ca.85^{o}) than those in areas of mixed lithology (ca.70^{o}) at Hartley Steps (Kjemperud 2011). At Snab Point segment 3, the fault trace of which affects different lithologies, has a perfect extensional Andersonian configuration (60^{o}) whereas the segments of fault 1 self-juxtapositioning a fluvial sandstone bed are much steeper (79^{o} and 85^{o}). This could suggest a lithological control on fault geometry, where fault traces in sandstone are steeper than those in mixed lithologies (figure 4.2). Alternatively the difference in geometry could suggest that the faults have been formed by different regional stress events. At Snab Point one possible scenario is that segment 3 were formed first during extension and fault 1 was formed later. However dip measurements from the largest subsidiary fault at the footwall of Crag Point Fault show that the dip angle varies according to which lithology it displaces. It has a more gentle dip (50^{o}) when cutting the less competent upper delta plain rocks compared to when cutting the Lower Crag Point Sandstone (80^{o}) (section 3.2.1). Rock of markedly different lithology can experience different infinite strain fields leading to strain controlled displacement (De Paola et al. 2005a). Mechanical strength of the host rock that faults are cutting has effects on fault geometry (Martel 1999). Fractures are well known to exhibit steeper dip angles when cutting competent beds than when cutting less competent lithologies (Wallace 1861, Dunham 1988, Ferrill and Morris 2003). Hence it is expected that

faults cutting softer lithologies have different characteristics than the main sandstone-cutting faults of this study.

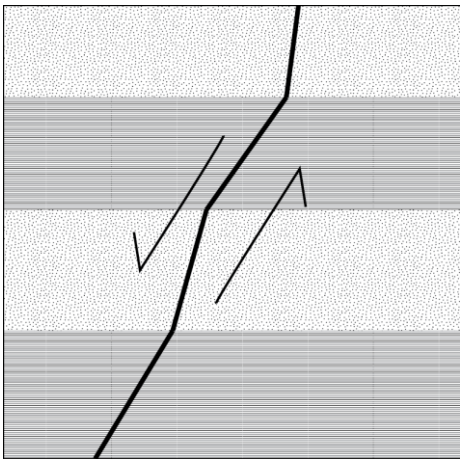

Figure 4. 2 Schematic illustration of lithological control on fault steepness where the faults are steeper in the relatively more competent sandstone compared to a weak shale

Strike-slip dominated faults

A significant horizontal component on both faults is likely to form steep faults as predicted by the Andersonian concepts which gives vertical orientation for strike-slip faults (Anderson 1951). Oblique slickenside lineations on master fault planes observed for the Crag Point Fault confirms horizontal influence however such structures are not seen everywhere. Along the main fault at Snab Point indications of horizontal movements are only faintly developed (if at al present) (figure 4.3). If the faults were strike slip dominated there are two possible scenarios;

i) The faults could have been initiated as strike-slip faults

ii) The faults could have been reactivated as strike-slip faults.

Figure 4. 3 Lenses in segment 1.2 displaying dextral shear

Both scenarios have potential to give the fault segments studied the orientation predicted by the Andersonian concepts for primary strike-slip faults (Anderson 1951). The regional development (section 4.5) excludes strike-slip activation as it is most likely that the faults were formed during thermal relaxation thus being extensional of nature. It is possible that strike slip reactivation could have steepened originally extensional shallowly dipping faults. At Crag Point the moderately dipping fault in the footwall of the main fault could represent the original fault trace (figure 4.4). Another possibility is that the faults were reactivated as strike slip faults because they were so steep (Richard and Krantz 1991). If strike slip reactivation has been a significant factor the reactivation of already steep fault traces appears to be the most likely case both considering the main fault at Snab Point and the faults delineating the horst-and-graben structures. No remnants of 60^{o} normal faults are found to be cut by the steep fault axes in either in these systems. In the horst and graben system many faults have a breccia content indicating high degree of deformation whereas negligible vertical separation is detected. Thus a possible horizontal movement is plausible as an additional deformation mechanism. No striations were found within either the fault systems at Snab Point or the horst and graben system at Crag Point which if found could either have confirmed or dismissed this. Since indications of strike-slip influence is only faintly

developed and only directly observed along the Crag Point Fault horizontal movement is proposed to have little or no influence on the geometry of the fault systems in this study.

Hanging wall migration

Reactivation of the faults is feasible to have steepened the faults independently whether reactivation was mainly a strike-slip or normal. Basin subsidence often steepens faults from the active extension phase of the basin formation (Gibbs 1984). During reactivation a steepening can be formed by migration of the active slip surface towards the hanging wall (Stewart and Hancock 1991). Active slip planes cut through the more brecciated hanging wall rather than the footwall. As slip deviates into the hanging wall the dip angle gets steeper by initiation of alternative fault traces (Stewart and Hancock 1988, 1991). The moderately dipping (50^{o}) subsidiary fault in the footwall of Crag Point Fault can represent an abandoned fault trace and the main fault a later developed steeper fault surface (figure). The subsidiary fault has a vertical offset of 2m and is trending in about the same direction as the main fault. Slip surfaces within Crag Point Fault tend to be steeper than the footwall master branchline and the hanging wall master branchline is steeper than the footwall one (figure 3. and figure 4.4), which support a steepening by hanging wall migration. At Snab Point no faults with a more shallow dip in the footwall were observed. The fault at Snab Point is however very steep (45/85 and 66/79) and the hanging wall master branchline is steeper than the footwall one. As no abandoned fault scarps are observed at Snab Point a different explanation must be sought for its steepness.

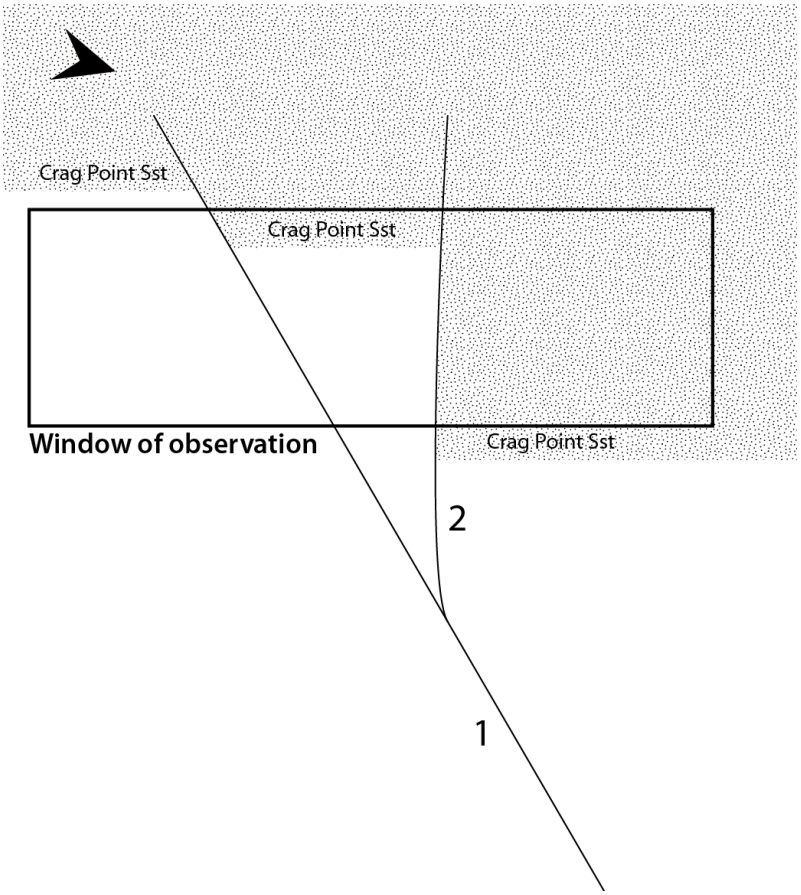

Figure 4. 4 An interpretation of how the fault traces can be outside our window of observation at Crag Point if hanging wall migration has occurred. The timing of the faults are marked with numbers where fault .2 represents Crag Point Fault

Antithetic faults developed over a larger fault

It is acknowledged that the main fault zones at both field sites are subsidiary antithetic structures within the hanging wall of larger faults (chapter 3).Steeper antithetic faults might form detached from the main fault within the hanging wall of this. This type of fault set is however more common in the basement and pre-rifting sediments and not post-rift sediments such as the Coal Measures (Gibbs 1984). At Snab Point the larger fault (segment 3) has a vertical separation of 21m and is located 20-30m SE of the main fault. At Crag Point the larger fault has a vertical separation of 56m and is located about 150m NNE of the main fault. It seems unlikely that these larger faults are large enough to have an influence. If the faults are formed as subsidiary steeper faults it must be as activation over an undetected shallowly dipping basement fault.

Conclusions

It seems unlikely that the faults have been formed as primarily strike-slip faults as strike-slip evidence are rare and scarce indicating an incipient strike-slip movement without significant effect on the faults' steepness. The faults show no indication of being formed as steep antithetic faults as no good subject for a larger fault they are likely to be formed in relation to is found.

The most likely explanation for the steepness of the faults appears to be a combination of the effects of shallow burial and lithological control of the relatively stronger sandstone. The lithological control requires that the burial must have been sufficient for the faults to be lithified during faulting. At Crag Point Fault an additional steepening factor could be hanging wall migration (figure 4.4). This process could have been active either during normal reactivation or strike-slip reactivation. A reactivation with a significant horizontal component (mean pitch 36^{o}) is suggested based on slickenlines.

4.3 Fault architecture (fault facies)

In the following section different elements constituting the fault zone (fault facies) (Braathen et al. 2009) is discussed and compared to previous studies done considering fault architecture. However elements directly affecting the faults sealing properties, membranes and cementation, are discussed separately.

4.3.1 Fault Zone

The difference in characteristics of the outer and central part of the fault zone is inferred by Clausen et al. (2003) to represent different stages in the faulting. First there is a development of a wide strain zone (the damage zone) where the frequency and density of fractures and/or deformation bands increase, before slip is transferred and a fault core is developed (Heynekamp et al. 1999, Clausen et al. 2003). From field observations it is challenging to determine how the fault zone developed and what feature came first as it is only viewed at one point in time. At Crag Point a theory that the damage zone is developed before the main fault trace fits well with the hanging wall migration theory (Stewart and Hancock 1991) where the more gentle dipping subsidiary fault in the footwall damage zone were developed first.

4.3.2 The fault core

Fault cores can act as both barriers and conduits to fluid flow, and such properties may vary during the fault progresses depending on the different constituents of the core. A common scenario is that the fault core is a conduit during the active faulting stage and a barrier later as pore space is filled by mineral cementation as the fault act as a control on fluid flow (Antonellini and Aydin 1995, Caine et al. 1996, Nelson et al. 1999, Clausen et al. 2003).

The fault core includes several different fault rock lithologies and structural elements such as fault lenses, membranes and discrete fractures (Caine et al. 1996, Heynekamp et al. 1999, Wibberley et al. 2008, Braathen et al. 2009). At Snab Point nearly all rocks in the core except for the relatively undeformed lenses has been eroded indicating that the core is mechanically weaker than the unfaulted rocks. Caine et al. (1996) suggest that a variation in thickness and composition of the core is an important control factor of fluid flow. These properties may vary both along strike and down dip, thus fluid properties may vary accordingly (Caine et al. 1996). The main fault at both localities have larger fault core at sections where there are several large lenses present (figure 3. and figure 3.) suggesting that the lens density is a major control on fault core size. This is comprehensible as lenses are larger than the other fault core components such as membranes and breccias. At Snab Point the core of segment 1.1 is largest where the fault segment is branching (figure 3.). At this position several large lenses are present illustrating the role of lenses as a core thickness control.

Grain size of the faulted rocks has a large significance for the deformation processes taking place. Clay rich host sediments get thinned and distributed far into the fault zone, whereas coarse grained host sediments typically get deformed into blocks and lenses and not moved as far (Heynekamp et al. 1999). The fault cores in this study all display lenses of similar material to that of the immediate damage zone. The largest lens at Crag Point has evidently been sourced from the immediate hanging wall (figure 4.5) illustrating that more competent material gets divided into blocks and incorporated into the fault zone (Heynekamp et al. 1999). The weaker material gets smeared within the fault zone (Heynekamp et al. 1999) as seen along the fault segment 3 at Snab Point where coal is smeared along the fault trace (Faerseth 2006).

Figure 4. 5 Lens 1 at Crag Point is sourced from the immediate hanging wall. a) Lens 1 in red b) faulted coal seams from the hanging wall damage zone

Several studies show that core thickness increases as the throw of the fault increases and that with increasing throw the variation of core thickness along dip also increases (Fossen and Bale 2007, Lindanger et al. 2007, Braathen et al. 2009). The measurements from Snab Point and Crag Point fits quite well with the dataset of Braathen et al. (2009) being in the upper part of the spectrum where the core thickness is rather large compared to the vertical offset (figure 4.6). This is as expected as the faults in this study both probably have a significant horizontal component making the total offset larger.

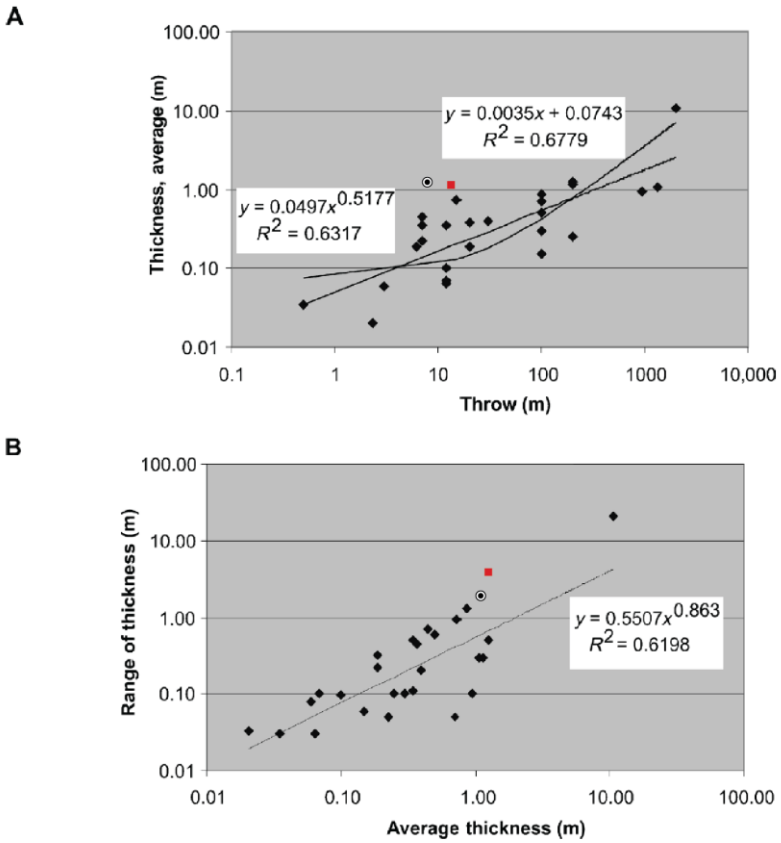

Figure 4. 6 Main fault of Crag Point (red square) and Snab Point (round point) compared to the data of Braathen et al.(2009). Regression lines are not adjusted to the data of this study.
A: Throw vs. average thickness of the fault core.
B: Average thickness vs. thickness range. Modified from Braathen et al. (2009)

Lenses

Most lens statistics in this study were gathered at Snab Point where 116m of the fault trace was mapped along strike. In the 26 studied fault outcrops by Braathen et al. (2009) there was dominance for four sided lenses. No lens statistic based on the symmetry and lens shapes were made at either locality. There are several lenses which are difficult to categorize due to their lack of symmetry. However from figure 3.7, figure 3.21 and figure 3.32 one gets a general impression of the lens shapes present. Several of the lenses have long sides parallel with y-direction and short rounded or parallel ends, something of the sort of 6-sided lenses in the study. All the studied lenses at Snab Point are sandstone lenses and as in the study of Braathen et al. the commonly contain an open network of discrete structures. The relative roughness that is prominent within the system is indicative of an early stage network of large lenses. Continued deformation is likely to smooth the lens surfaces as well as divide the larger lenses into smaller ones (Gabrielsen and Clausen 2001). This is a likely explanation for the smaller lenses to appear smoother and more symmetric.

Lenses formed in the secondary stage are mainly generated by coalescence of Riedel shears and other secondary fractures, while lenses formed in early are mostly generated by segment splaying and amalgamation(Gabrielsen and Clausen 2001, Lindanger et al. 2007). From the rose diagrams made on the lens populations in this study it appears that few of the lenses in this study are generated by coalescence of Riedel shears as the majority of b-axes are trending in y-direction. It is only in segment 2 that there is some trend 30^{o} off the y-axis direction main trend (figure 4.7) which is at odds with the literature since this is the least developed fault trace. Asperity bifurcation is the most common initiation mechanism for fault lenses throughout the extension (Gabrielsen and Clausen 2001, Lindanger et al. 2007).

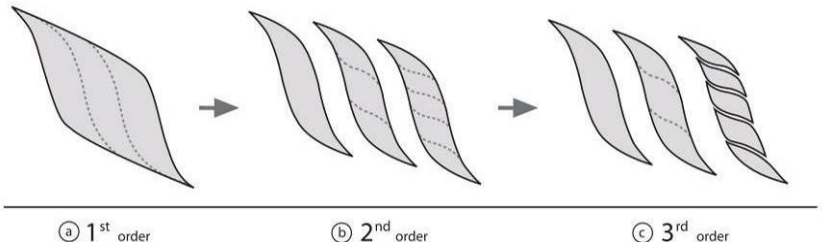

figure 4. 7 Creation of higher order lenses by splitting of existing ones (Lindanger et al. 2007)

In Segment 1.1 7 out of 10 large lenses have several smaller lenses within thus displaying several generations of lenses at once. Generally fault lens geometry changes and often becomes more varied through the faulting process. This is due to the increased presence of several generations of lenses, both by initiation of new (first-order) lenses and initiation of higher-order lenses by breaking up old ones. Since the breakup of existing lenses often takes place in fractures of Riedel shear direction (30°), we get shorter and relatively thicker lenses as the higher order lenses are generated (figure 4.7) (Lindanger et al. 2007).

Dimension of lenses

The relative dimensions of the lenses in this study are compared to three different studies from the literature Bastesen et al. (2009), Braathen et al (2009) and Lindanger et al. (2007) (table 4.1). The lenses in the study of Bastesen et al. (2009) were measured along a fault lane of the Doumena fault from the Gulf of Corinth, Greece, with a vertical offset of 500m. Most of the lens measurements were made on length (*c*-axis) and width (*b*-axis), while thickness (*a*-axis) measurements were made on 7 of the 33 lenses. Braathen et al (2009) analysed 26 faults in silisiclastic rocks in Sinai, Egypt, with vertical offsets ranging from less than a meter to nearly 2000m. The length vs. thickness ratio (*c:a*) on the faults in Braathen et al. (2009)

shows varied lens geometry with some large, probably first order, lenses and several smaller and thicker (higher-order) lenses (Braathen et al. 2009). The lenses reported by Lindanger et al. (2007) were measured along length (*c*-axis) and thickness (*a*-axis). Measurements come from 4 different settings in 3 field sites and one analogue plaster study, while the faults have vertical separation ranging from 0,01m-19m. For higher order lenses Lindanger et al (2007) found a 1:1 relationship between the length (*b*) and thickness (*c*). Regarding both higher and lower order lenses, it is found that the c-axis is longest along dip while the a-axis is shortest perpendicular to both dip and strike(Lindanger et al. 2007, Bastesen et al. 2009).

Dataset	N	Regression analyses	R^2 Confidence factor	Relative length (*c*) vs width (*b*) vs thickness (*c*) *a:b:c*
Frøya, all lenses	25	a=0,06c+5,60	0,47	16,7:*b*:1
Bornholm, all lenses	83	a=0,09c+1,523	0,57	12,5:*b*:1
Kilve, all lenses	96	a=0,18$c^{0,83}$	0,74	7,9:*b*:1
Plaster-of-Paris, all lenses	119	a=0,13c-0,01	0,59	7,7:*b*:1
Complete dataset (Lindanger et al. 2007)	323	a=0,08c+1,26	0,71	12,5:*b*:1
Doumena Fault (Bastesen et al. 2009)	33	b=0,39c+3,096	0,85	32:19:1
Western Sinai, all lenses (Braathen et al. 2009)	48	a=0,14$c^{0,8999}$ (outlier excluded)	0,85 (outlier excluded)	9:*b*:1
Snab Point, segment 1.1	94	a=0,27b^{075672}	0,58	*c*:5,6:1
Snab Point, segment 1.2	35	a=0,24$b^{0,6111}$	0,46	*c*:10,6:1
Snab Point, all lenses fault 1	129	a=0,26$b^{0,7281}$	0,55	*c*:6,3:1
Snab Point, segment 2	21	a=0,28$b^{0,8877}$	0,55	*c*:6,4:1
Crag Point Fault	12	a=0,28$c^{1,1291}$	0,71	3:*b*:1

Table 4. 1 1 Data on lenses in this study as well as from the dataset of Lindanger et al. (2007) and Bastesen et al. (2009). The *a:b:c* relationship is calculated from linear or power law regression equations in pursuance of which gives the best fit regression line. The regression analyses present the best fit regression lines except for the Crag Point Fault and segment 1.2 at Snab Point. The Crag Point Fault dataset has a best fit for an exponential trend (a=0,0406e^{1,6618c} R^2=0,8482) The segment 1.2 dataset has a best fit for a logarithmic trend (a=0,1904ln(*b*)+0,3373 R^2=0,4996). Note that this table display regression lines for both thickness (*a-axis*) vs length *(c-axis)*, thickness (*a-axis*) vs width *(b-axis)* and width *(b-axis)*, vs length *(c-axis)*.

Although *b*:*a* ratios generally result in thicker lens data than *c*:*a* ratios, the difference is considered to be insignificant in this context as the *c*:*a* ratios at Crag Point were the thickest overall (table 4.1). Presuming a universal *c:b*:*a* relation of 10:9:1 and using this to calculate estimated *c:a*-ratio for the lenses at Snab Point we get 7:1 for fault 1. This is still markedly thicker than in the literature (table 1). In the following discussion *b*- and *c*-axes are directly compared for simplicity. The *b*-axes at fault 1 at Snab Point are 3 times thicker than the *b*-axis Bastesen et al. (2009) measured in the Domena fault, 2 times thicker than average c-axes in Lindanger et al.(2007) and 1,4 times thicker than the *c*-axis from Braathen et al (2009) (table 1). The *c*-axes at fault 1 at Crag Point are 11 times thicker than the *c*-axis Bastesen et al. (2009) measured in the Domena fault (table 1), 4,2 times thicker than average c-axes in Lindanger et al.(2007) and 3 times thicker than the *c*-axis from Braathen et al (2009) (table 4.1). Bastesen et al. (2009) a 3:2 relation between *c*:*b*-axes found in his study of the Doumena Fault in Greece, which represents a much bigger difference than what is presumed to be the case at Snab Point. The lack of knowledge of the *c*:*b*-ratio at Snab Point adds insecurity to the relative thickness of the lenses.

Lindanger et al. (2007) found that lenses in faults with a large vertical displacement seem to be relatively thicker than those in faults with less displacement. This is probably related to the lens forming mechanism active during their generation. The main faults in this study have a relatively large vertical displacement compared to their faults. The large throw indicates that the faulting would have proceeded for such an amount of time that several higher-order lenses have formed (Lindanger et al. 2007). The lenses measured at Snab Point are on average thicker than the ones measured in Lindanger et al. (2007). This fits with the assumption that lenses in faults with a large vertical displacement seem to be relatively thicker than those in faults with less displacement. However the lenses in fault 1 are not markedly thicker than the lenses in the segment 2, as the difference in vertical displacement could suggest. Thus vertical displacement has negligible importance on the lens thickness in this study.

Colnclusions

Lens geometry is proposed to be self-similar within one fault system but to a less degree so when systems of different lithology, strain rate and displacement are compared (Bastesen et al. 2009). Contrary to these assumptions the lens relations at Snab Point have a low self-similarity, expressed by their confidence factor. Lenses in this study, from both localities, are thicker than the ones in the literature indicating some similarity within the same lithology and

regional stress influence. However the average *c:a* relation for the lenses at Crag Point are nearly 1,6 times thicker than the *b:a* at Snab Point. This is contradictory to the assumption that *c*-axes are relatively longer than *b*-axes. It can be concluded on basis of lens statistics from Snab Point and Crag Point that the individual fault system exercises great control on the lenses relative dimensions and there is great variety within individual systems. It is therefore unsuitable to directly compare lens geometries without taking the individual fault characteristics into account.

4.3.3 Damage zone

At Snab Point the main fault is within the hanging wall of fault 3, which was studied by Færseth (2006). At Crag Point it is difficult to determine the full extent of the damage zone due to grabens both south and north of the Crag Point Fault. These circumstances make the damage zones of both localities dependant of external factors and therefore they can not be used in a direct comparison with other studied damage zones. Statistically damage zone width is about 2 orders of magnitude wider than its fault core when measured as an increase in brittle deformation (Fossen and Bale 2007). This gives an expected damage zone width for Snab Point (with an average core width of c.1,5m) of *c.*150m, and for Crag Point (with an average core width of c.1,2m) *c.*120m. Estimates such as this illustrate that there are great variations both in damage zone and fault core thicknesses along faults (Braathen et al. 2004, Fossen and Bale 2007).

The width of damage zones varies according to what parameter is being measured, where an increased fracture frequency gives the widest fault zone and microscopic and compositional changes gives a much narrower one (Schulz and Evans 2000). Crag Point Fault has subsidiary faults in an area 17m from the footwall master branchline and none on the hanging wall side. This is at odds with previous studies which have shown that the hanging wall damage zone is often observed to be wider than at the footwall (Berg and Skar 2005, Fredman et al. 2008).

The steepness of the faults in this study should be taken into consideration since this makes for less clearly defined hanging walls and footwalls. This could be a possible explanation for the lack of accordance with previous studies of damage zones in extensional faults. In strike-slip faults damage zones are characterized by being long, narrow and symmetrically

distributed along the fault trace (Kim et al. 2002). Most of the damage zones in this study are distributed damage that occurs along the fault trace based on the classification given by Kim et al. (2002). However at Snab Point the left stepping soft linked fault bridge between segment 1.1 and segment 1.2 falls under the classification of linking damage. Like the study of strike-slip faults at Masalforn (Kim et al. 2002) the linking damage at Snab Point show extensional fracturing between the fault traces (chapter 3.1).

Fracture frequency diagrams made across the main fault at Snab Point show a high fracture frequency as far as 20m into the footwall (figure). Either the damage zone is greater than 20m or there is a high background fracture frequency. The hanging wall side of the damage zone is more deformed than the footwall one as there is a subsidiary fault there, segment 2. As the hanging wall damage zone is within the hanging wall damage zone of the significantly larger fault 3 it is likely that segment 2. as well as fault 1. are both subsidiary faults to this within fault 1 hanging wall.

Wide damage zones are created by multiple slip episodes, where each episode overprints the previous (Caine et al. 1996, Shipton and Cowie 2002). Strain softening is decreasing the overall width, gathering the strain within the fault core. Strain hardening is increasing the width as damage is preferentially accumulated in undeformed host rock (Shipton and Cowie 2002). The regional development implies that the faults in this study have been reactivated up to four times and the damage zones are therefore expected to be large. This is a likely explanation for the high fracture frequency far away from the core at Snab Point. At Crag Point it is difficult to infer a damage zone width as the graben to the south and the horst and graben system to the north are conflicting the original damage zone. However it can be argued that this is a part of the Crag Point Fault damage zone as the deformation process creating the graben structures probably also reactivated the fault. Both Heynekamp et al. (1999) and Caine et al. (1996) found a relation between grain sizes and bed thickness of host material and damage zone width, where coarse grained material in thick beds as the ones in this study gave a wide damage zone. Thus it is expected that the fault at Crag Point has a larger damage zone than the ones in the nearby delta plain deposit studied by Kjemperud (2011). Damage zone width is varying according to changes in slip along the fault trace which is among other factors dependent on changes in host rock properties (Martel 1999, Kim et al. 2000). Damage in mixed lithologies where slip is expected to vary due to varying host rock properties should

therefore be expected to have larger damage zones than damage zones in self-juxtapositioned sandstone such as the main faults of this study.

On the foundation of fieldwork, Berg and Skar (2005) subdivided the footwall damage zone into two zones, the inner and outer zone where the outer zone is by far the largest. The inner zone shows a high but even fracture frequency with high connectivity between fractures and is where most of the deformation bands are present. On average the outer zone has an 8 times lower fracture frequency, which is relatively even throughout or decreasing some towards the unaffected host rock (Berg and Skar 2005). This is somewhat similar to the footwall of Crag Point Fault where the first four metres have a fracture frequency of *c*. 20 fractures/metre followed by a zone of lower fracture frequency (figure).

There is a tendency for damage zones to be better conduits than both the fault core and the host rock (Caine et al. 1996, Heynekamp et al. 1999). The majority of the fractures in the damage zone of Crag Point Fault are oriented in y-direction direction (figure). This implies that the overall conductivity primarily increases in a fault parallel direction. Deformation bands in the damage zone reduce permeability, while the overall fracturing increases it (Caine et al. 1996). Few deformation bands were found at either of the localities, while those found were present within the cores. Even in highly permeable sandstone damage zones where deformation bands are the dominant deformation mechanism they are unlikely to present significant fluid flow barriers (Fossen and Bale 2007). Where deformation bands are organized in closely spaced zones they could cause a drop in permeability of about 2 orders of magnitude (Antonellini and Aydin 1995). It is likely to assume that the damage zone permeability was increased at both localities due to fracturing (Caine et al. 1996). As the damage zone appears to have similar permeability as the fault rocks of the core it is likely that the damage zone makes a significant contribution to the bulk fault zone permeability (Odling et al. 2004).

4.4 Sealing capacities of the faults

The self-juxtapositioning faults in this study will not form juxtapositioning seals. To form seals these fault systems are dependant on impermeable fault rock oriented so that the fault is sealing either along or across dip. Orientation of impermeable fault rocks is of large significance for the sealing capacities. Fault perpendicular fluid flow will be restricted by

fault parallel seals and vice versa. The faults could have been sealed during primary processes such as faulting by membranes forming, or secondary processes such as cementation (Knipe et al. 1997, Heynekamp et al. 1999).

Membranes

Some membranes were found within the fault cores at the localities in this study mostly along the vertical exposures whereas fault rocks often have been eroded along the horizontal sections. Membranes consist of fault rocks as cataclasite, breccias, sand gouge, shale gouge, sand smear or shale smear (Fredman et al. 2008, Braathen et al. 2009). Cataclasite, breccias and gouge such as those found in the core of Crag Point Fault are fault rocks created by crushing of host rocks. Smears such as the one along segment 3 at Snab Point are host sediments that have been transported along the fault core in a ductile manner (Braathen et al. 2009). Membranes present in the core of fault 1 and fault 2 at Snab Point might have been present along the fault trace but later exposed to secondary erosion. Hence potential membranes are probably composed of weaker material than the host rock, as material around the lenses is eroded and thus offers no restriction to fluid flow.

The potential of self juxtaposed sandstones such as the ones at Crag Point and Snab Point to be sealing across the fault surface relies of mechanisms such as denser grain packing and grain crushing. Fluid flow barriers can be formed from membranes formed either by grain disaggregation or phyllosilicate smearing (Faerseth et al. 2007). Some smearing of thin coal bands are observed along the fault surfaces but as these seams originally are *c.*1cm in thickness the sealing capacity is estimated to be low. The sandstones affected in this study are composed of clean quartzitic sand so disaggregation is the most likely mechanism.

The shape of membranes ranges from continuous to pockets of fault rock with less than 10% continuity (Figure 4.8 and figure 4.9). Their continuity is important due to its significance to fluid flow (Braathen et al. 2009). The breccias at Crag Point are not continuous along dip, they are only extensive where the lithology contrast is greatest and the Upper Crag Point Sandstone is juxtaposed against upper delta plain deposits. It is difficult to map out continuity of the clay gouge membranes present between several of the breccias due to visibility and secondary erosion. The gouge membranes are thin, less than a cm in average and it is therefore unlikely that they are continuous in three dimensions. The fine grained material of the gouge is likely to make the membranes flow retarding or sealing if continuous. If we had

been able to map out continuous membranes along our fault surfaces it would still have been an estimate for the faults sealing capacity. Fluid flow in faults often is channelled into areas with highly fractured rock (Sibson 1977, Caine et al. 1996, Kim et al. 2002).

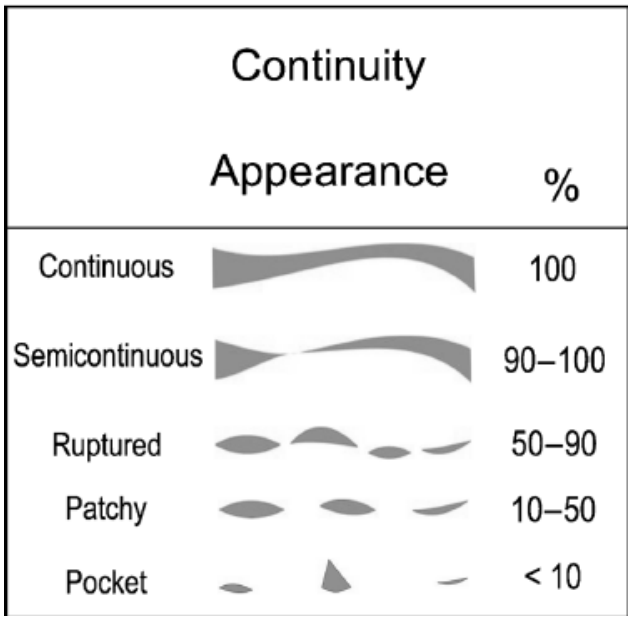

Figure 4. 8 Classification of membrane shape (Braathen et al. 2009)

The ratio between lens covering membranes and lenses is important as membranes covering lenses will decrease fluid flow (Fredman et al. 2008). Since lenses often are made up of relatively undeformed host rocks, such as the lenses in this study, there is a large permeability contrast between membranes and lenses (Lindanger et al. 2007, Fredman et al. 2008, Braathen et al. 2009). However no continuous membranes were found except at segment 3 at Snab Point where smeared coal forms a membrane varying between 20-2cm. A fault dominated by sandstone lenses will be sealing if it is enveloped by continuous clay membranes all around. This is not observed around any of the lenses in this study but membranes might have been present and then later eroded when the faults where exposed at the surface. In ring-shear experiments and at locality no.1 in Clausen et al. (2003) continuous membrane envelopes was a common scenario. They also found through experiments that continuous to semi continuous clay membranes are typically formed by plastic clays with a high water pressure (Clausen et al. 2003).

It appears unlikely that the faults have sealing membranes as the membranes which are observed are thin and not continuous. However it is possible that there have been continuous membranes present that have later has been exposed to secondary erosion. Thus it is impossible to tell from present day exposures if there have been sealing membranes or not. As

erosion at Snab Point is differential and has mainly affected fault rocks it is plausible that they have been formed during strain weakening and thus unlikely to be sealing.

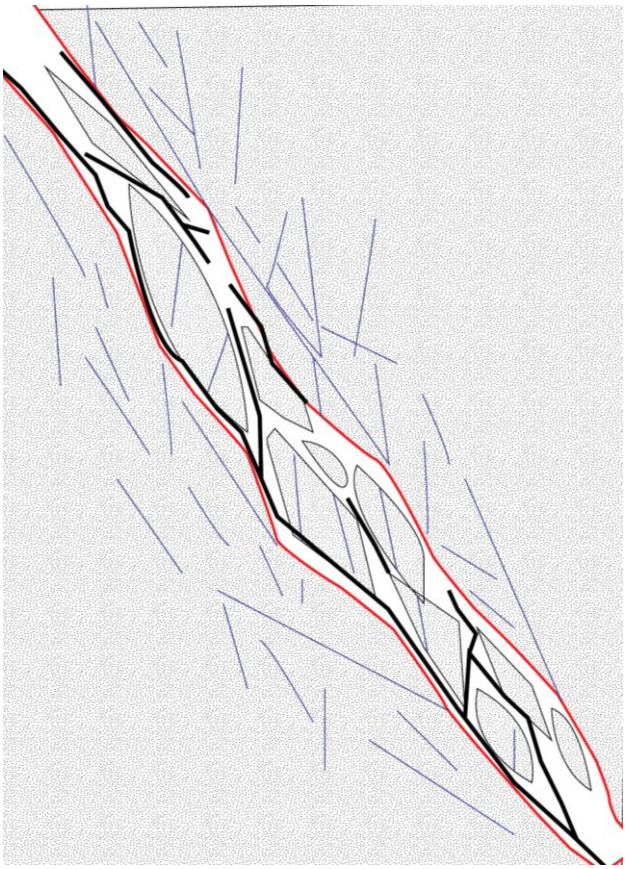

Figure 4. 9 Conceptual figure for a fault self-juxtapositioning sandstone sealed by continuous membranes. Membranes formed by grain disaggregation where deformation has been greatest. In this figure deformation has been greatest along the footwall master branchline and in between some of the lenses. The degree of fluid flow restriction is controlled by 3D continuity of the membranes. Fractures-blue. Master branchlines-red.

Cementation

Sealing across the fault zone can be obtained by permeability reduction due to cementation (Knipe et al. 1997). Some calcite cementation is found within fault cores from both localities (appendix A) indicating that they originally were permeable but that later cementation has retarded the flow potential. Diagenic alterations such as cementation are assembled in areas of structural complexity (Sibson 1996, Eichhubl et al. 2009). It is therefore likely to find cementation at Snab Point near the stepping fault trace of fault 1 and at the intersection between segment 1.1 and branch 1. This fits with observations of calcite mineralization in a lens near the branching point of segment 1.1 (figure). Mineralization such as cementation and mineral filled fractures indicate that fracture parallel permeability has been enhanced (Antonellini and Aydin 1994). Thus fault parallel permeability probably has been enhanced along faults at both Crag Point and Snab Point. In smaller normal faults (throw up to 1m) near

vertical normal faulting is known to enhance pathways for along-strike fluid flow (Ferrill and Morris 2003). If fluid flow was focused along the fault core this will have lead to a differential cementation. Hence the fault zone later may act as a seal due to cementation as in the study of Nelson et al (1999). Another possibility is that the fault zone can be enriched in calcite cement by preferential growth on quartz disaggregation membranes during fault perpendicular flow (Whitworth et al. 1999). Here a more extensive microscope study of the rock samples gathered would be of help. Field observations of fractures show inconsistence in mineralization, where a variable part of the fractures are mineralized (figure 3.2). Therefore it is assumed that mineralized fractures have negligible effect on fluid flow whereas the effect of cementation still remains uncertain. Depending on degree of cementation the faults could act as seals (figure 4.10) (Knipe et al. 1997). Degree of cementation and mineralization of fractures may vary several orders of magnitude at the same depth depending on the spatial distribution of fluid pressure (Bruhn et al. 1994).The timing of cementation is crucial in order to understand how it might have affected fluid flow. The two end member possibilities is;

i) Cementation is extensive and has effectively sealed the faults when inactive. They have only been permeable during active faulting stages (Bruhn et al. 1994, Antonellini and Aydin 1995, Caine et al. 1996, Nelson et al. 1999, Clausen et al. 2003).

ii) Cementation is scattered and does not affect fluid flow in any significant degree. Traces of cement that is found has been emplaced in the system at a late stage.

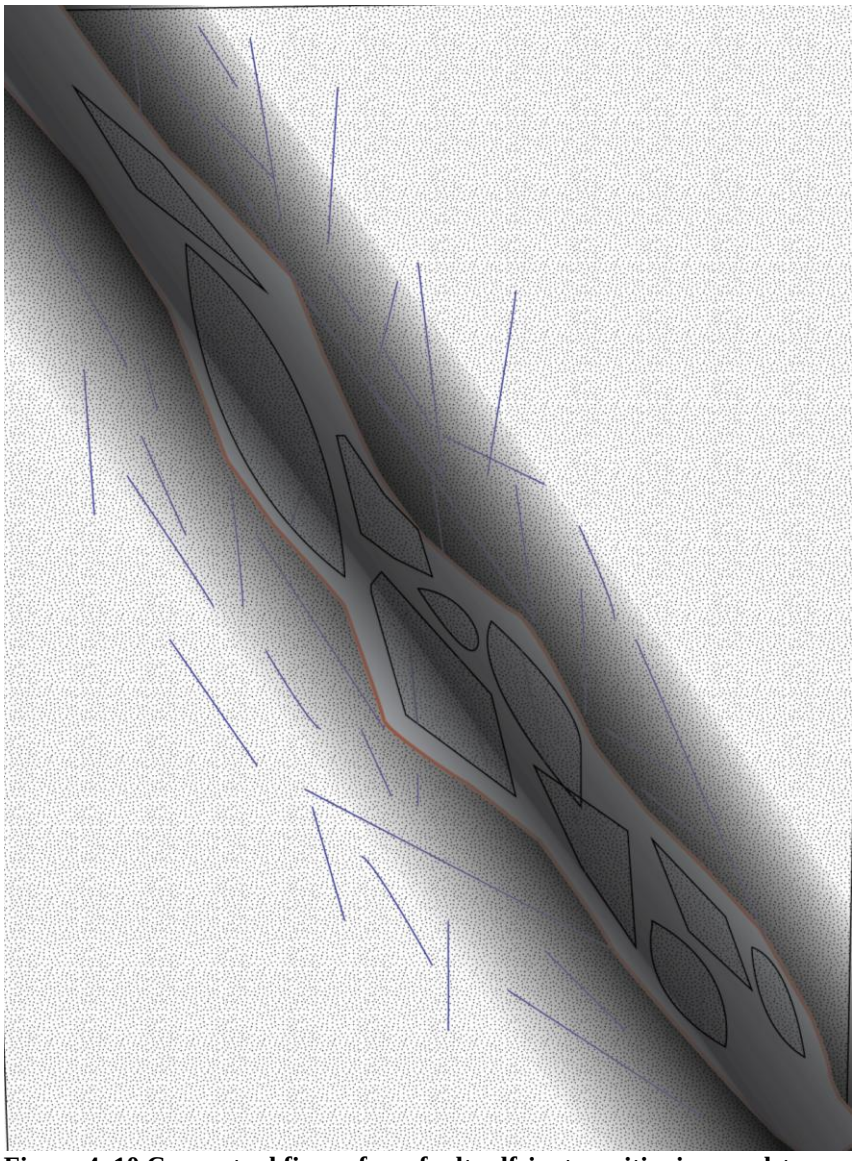

Figure 4. 10 Conceptual figure for a fault self-juxtapositioning sandstone sealed by cementation which has preferentially grown in the fault core. The degree of fluid flow restriction is controlled by amount and extent of cementation.

4.5 Structural history and stress configurations (extension then reactivation)

The stratigraphy at Crag Point is well known and placed within the regional stratigraphy (Jones 1968, Land et al. 1974, Johnson 1984, O'Mara and Turner 1999). At Snab Point none of the regional marker beds are present. However local marker beds that are adequate for correlation of the scale of the faults are available. Geological maps of the basin show that the Coal Measures Strata extends north of Amble where the stratigraphically lower Upper Limestone Group is outcropping (Johnson 1984, Chadwick et al. 1993). Johnson et al.(1984) stated that the sedimentation of Westphalian Coal Measures over the Northumberland Basin

was of uniform thickness. Thus the northernmost locality, Snab Point, has been buried deeper than Crag Point. The maximum thickness of Coal Measure Strata in the Northumberland Basin was 850m (Chadwick et al. 1993). Based on the Five quarter Seam marker bed the Coal Measures overlay at Crag Point was *c*.650m with that the overlay at Snab Point must have been between 650m-850m (Johnson 1984, Chadwick et al. 1993).

Estimations of burial depth during the post-Permian deformation is highly uncertain as the thickness of Permian strata in Northumberland is uncertain (Smith 1970, Chadwick et al. 1995). Vitrinite reflectance data suggest that the Northumberland Basin reached its maximum burial during the thermal subsidence of the basin thus the Mesozoic burial was limited and the sediments in this study were shallower than 650m at Crag Point and shallower than 850m at Snab Point (Johnson 1984, Fraser and Gawthorpe 1990, Chadwick et al. 1993, Chadwick et al. 1995). Erosion was in progress from middle Triassic times affecting burial depth at reactivation (Austin et al. 2009).

4.4.1 Initiation

The main faults in the two localities studied have orientations parallel to the basin forming faults that are varying from E to ENE and formed in a dominantly N-S extensional stress field (figure) (Chadwick et al. 1993). This makes it likely that the main faults at both localities are formed within the same stress field during the thermal relaxation phase of the basins history. The post rift phase was characterized by steady pace normal faulting and took place from early Namurian into Westphalian times (Kimbell et al. 1989). The faults were then likely to be hard linked with older active extension faults at depth. Thermal subsidence took place both during and after deposition of the faulted rocks which was deposited in Westphalian B times (Land et al. 1974, Johnson 1984, O'Mara and Turner 1999). Faulting due to thermal subsidence could therefore have happened both during and after sedimentation. Syn-sedimentary faulting is likely to have acted simultaneously with sedimentary compaction effects which could have modified the faults (Chadwick et al. 1993). If the faults are formed after sedimentation they are still likely to be formed near the surface. The maximum overlay of Coal Measure Strata was at Crag Point *c*.650m and at Snab Point up to 850m at the end of Westphalian (Johnson 1984, Chadwick et al. 1993). Steepness of the faults could suggest shallow burial, as faults close to the surface are very steep the upper tens of metres where lateral confining pressure is low (Jackson and McKenzie 1983).

4.4.2 Reactivation of fault systems

The following section concerns later tectonic events and how these could have affected the fault systems. It is likely that the faults were active several times in the geological history (figure 4.11). The slickenlines with a significant horizontal component found on Crag Point Fault is an indication that pure extension during thermal subsidence is not the only process that has influenced the systems.

There are four different events timed after the thermal relaxation phase of the system which could have affected the system (chapter 2.2).

1) The Variscan inversion which influenced the Northumberland Basin with an N-S to NE-SW strike folds in a NE-SW to NNW-SSE orientation in the north and west of basin. In the southern and eastern part where both localities in this study are located it is suggested that the entire basin (or at least the upper part) was transported westwards as one coherent allochthonous unit (Collier 1989).
2) The faults could have been affected by extension due to the emplacements of the Whin Sill complex.
3) A Late Carboniferous partitioned transtensional event as suggested by De Paola et al. (2005b). With a regional transport direction in a NNE-direction.
4) Early rifting stages in the North Sea is known to have affected nearby strata of Permian age with one set of dextral ENE strike slip faults, one set of ESE sinistral strike-slip faults and N-S trending reverse faults indicating a E-W σ^3.

The main faults in this study are striking in an ENE-WSW to NE-SW direction. Where the main fault at Crag Point is striking more to the east, 79/89, compared to Snab Point where the fault segments are oriented 45/85 and 66/79 (Chapter 3). At Crag Point the diagonal coal striations confirms a significant horizontal component. It is unlikely that the striations are formed near the surface since near-surface faults rarely observe strike-slip reactivation as the cohesion loss observed on faults near the surface is insignificant (Richard and Krantz 1991). Negative flower structures in the core of Snab Point Fault and segment 2 at Snab Point suggests a transtensional influence. In an idealized Andersonian dextral strike-slip fault σ_1 is placed 30^o south of the fault trace (Anderson 1951). Thus the oblique slip observed on Crag Point Fault could be indicative of a north easterly transport direction as opposed to an easterly

one that pure strike-slip slickenlines would suggest. The main types of mineralization found in the horst and graben system is calcite, hematite and manganese oxide.

It seems likely that the westward transportation of the basin during the Variscan inversion could have reactivated the faults of this study in a dextral sense. However a transtensional regime as indicated by observations is at odds with an inversion such as the Variscan that represent a compression. It is possible that the extensional component of the coal striations is a representation of local strain variations as opposed to a different transtensional regional event. The fault could be placed in a releasing bend in a scale larger than our window of observation. Alternatively it could be that the faults were reactivated during an extensional stress state after the Variscan inversion where residual strain from the Variscan orogeny caused the horizontal component.

As it is common that faults act as a conduit for fluids during the active stages of faulting (Caine et al. 1996) it seems probable that there is a hydrothermal signature if the faults were reactivated during emplacement of the Whin Sill Complex. The mineralization associated with the Whin Sill intrusions is quartz, calcite and pyrite (De Paola et al. 2005b). It is therefore different to that associated with the fault systems in this study. Here data from the microscope study would be of help in adding certainty to the field observations. The subsurface water given the type of mineralization seen within the fault systems of this study could have a different origin, such as meteoric water, buried seawater or water released by dehydration. Diffusion driven transportation across the redox boundary often gives high gradients of reduced sulphur and manganese in porewater derived from seawater (Bjørlykke 2010). Hence it is probable that the hematite and manganese mineralization is derived from subsurface seawater enriched with these ions.

The NNE Late Carboniferous transport direction proposed by De Paola et al. (2005b) fits well with the oblique slip observed on Crag Point Fault. However both Crag Point and Snab Point are within the extension dominated domain. Strike-slip components within this domain are interpreted to represent reactivation of deeper Dinantian structures reactivated during a later Permo-Mesozoic deformation (De Paola et al. 2005a, De Paola et al. 2005b).

The negative flower structures at Crag Point and segment 1.2 at Snab Point as well as diagonal coal striations at Crag Point could indicate a stress field transtensional to the pre-

existing faults which led to a dextral reactivation. This is how the post-Permian transtensional regime affected Permian strata at Cullercoats approxiomately 5km south of Craig Point (Collier 1989). If North Sea stress fields have caused a strike-slip component on faults in this study this is compatible with a reactivation of existing ENE-WSW normal fault structures (Collier 1989).

Considering the negative flower structure that is evident at both localities it does not seem likely that two local strain fields varied from the regional, e.g. releasing bends present at both field sites. It could be that the Variscan orogeny had little or no effect on the faults and that they have been reactivated by a different transtensional event such as one caused by the early rifting stages in the North Sea.

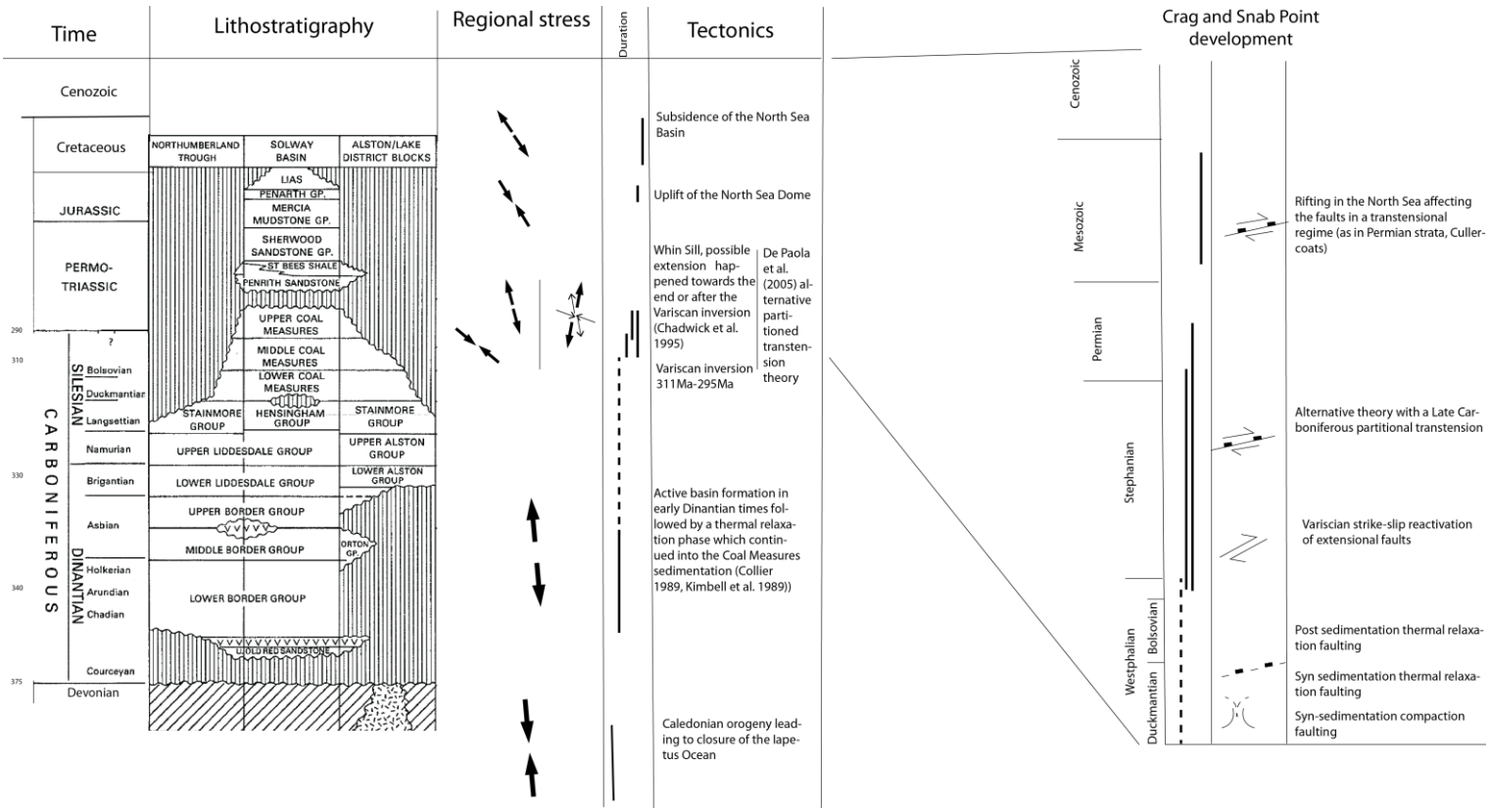

Figure 4. 11 Regional stress events and how they might have affected the faults in this study. See discussion for further explanation

5. Summary and final conclusions

5.1 Geometry

The most likely explanation for the steepness of the faults appears to be a combination of the effects of shallow burial and lithological control of the relatively stronger sandstone. The lithological control requires that the burial must have been sufficient for the faults to be lithified during faulting. At Crag Point Fault an additional steepening factor could be hanging wall migration (figure 4.4). This process could have been active either during normal reactivation or strike-slip reactivation. A reactivation with a significant horizontal component (mean pitch 36^{o}) is suggested based on slickenlines.

5.2 Fault architecture

Core thickness is directly related to the amount of displacement on both study sites similar to what has been found in other studies e.g. Braathen et al. (2009). Lenses are the greatest control on core thickness at both field sites. Different to other studies the lenses in this study are mainly directed in y-direction along strike with no significant Riedel shear influence and they are relatively thicker than ones in the literature (Braathen et al. 2004, Lindanger et al. 2007, Bastesen et al. 2009). Vertical displacement has negligible importance on lens thickness in this study as lenses in fault 1 are self-similar to the lenses in fault 2. The individual fault system exercise great control on the lenses relative dimensions.

The damage zones of both localities are dependant on external factors. It is likely that both localities have a wide damage zone probably related to multiple slip episodes due to reactivation (Caine et al. 1996, Shipton and Cowie 2002). At Crag Point the footwall damage zone can be divided into an inner and a outer zone, where the outer zone is the largest and the inner zone show a high but even fracture frequency (Berg and Skar 2005). The damage zone permeability was increased at both localities due to fracturing and it is a significant contributor to the bulk fault zone permeability (Caine et al. 1996, Odling et al. 2004).

5.3 Sealing capacities

No continuous membranes are observed. There are two possible explanations for this, (i) membranes could have been exposed to secondary erosion; or (ii) they have never been present. The thickness of sections of fine grained membranes observed are thin therefore it is

assumed that they have not been sealing. The estimation of membranes influence on the core is challenging at Snab Point as fault rocks have been eroded. This suggests strain weakening dominating the deformation process thus it is unlikely that sealing fault rocks were formed.

Mineralization found along the fault traces indicate that fault parallel permeability has been enhanced (Antonellini and Aydin 1994), some degree of mineralization is found along all fault surfaces in this study. Hence fault parallel permeability has been enhanced. If the fault systems exhibit preferential growth of cementation and mineralization the faults could act as seals depending on degree of cementation (Knipe et al. 1997).

To determine whether the faults in this thesis are sealing either by continuous membranes or cementation, further studies need to be done. Field observations suggest that membranes may not be sealing, while thin section analysis displays evidence of calcite cementation (Appendix A), suggesting this could be a dominant sealing process.

5.4 Structural development

The faults were probably initiated syn-sedimentary during thermal relaxation and exposed to reactivation up to several times later. There are at least four structural events that possibly have caused reactivation.

- Post-sedimentary faulting during burial.
- Variscan inversion
- Extension in relation with Whin Sill emplacement
- Right lateral extensional in relation with early North Sea rifting.

There are some problems with the late Carboniferous theory of de Paola et al. (2005b). It has in later studies not gotten significant acknowledgement as an explanation for the cause of events. It is therefore uncertain whether it should be taken into consideration. Additionally de Paola et al.(2005) themselves seek post-Permian explanations for wrench faults present in their extension dominated domain. The Variscan inversion is a possible activation event if regional strain variations that promote transtension were active at both localities since the Variscan event represents transpression.

5.5 Further studies

Further studies need to be done to better understand burial depth and timing of events affecting the faults in this system. In particular post-Palaeozoic development is currently vaguely determined.

To better understand and be able to predict fault zone architecture a continued development of fault core characteristics is necessary. To better understand fault architecture of the faults in this thesis further processing of data gathered in the field, (e.g. lens statistics) as well as expansion of the existing data (e.g. widening of the fracture frequency diagrams) is required.

Different techniques can be used to better describe the faults in this study. Drill sections of the fault cores can provide a better idea for the sealing properties of the fault membranes as this will disregard any secondary erosion. More detailed mineral study of the thin sections in appendix A as well as further studies on samples gathered during fieldwork can increase our understanding on micro-structural damage as well as sealing capacity of the cement.

6. References

Anderson, E.M. 1951. The dynamics of faulting. *The dynamics of faulting and dyke formation with applications to Britain*. Edinburgh and London: Oliver and Boyd, 7-22.

Antonellini, M. and Aydin, A. 1994. Effect of faulting on fluid flow in porous sandstones: petrophysical properties. *American Association of Petroleum Geologists Bulletin* 78, 355-377.

Antonellini, M. and Aydin, A. 1995. Effect of faulting on fluid flow in porous sandstones: geometry and spatial distribution. *American Association of Petroleum Geologists Bulletin* 79, 642-670.

Austin, L., Egan, S., Clarke, S., Kirby, G. and Millward, D. 2009. The geology and geodynamics of the Northumberland Trough Region: Insights from mathematical modelling. 17.

Bastesen, E., Braathen, A., Nøttveit, H., Gabrielsen, R.H. and Skar, T. 2009. Extensional fault cores in micritic carbonate-Case studies from the Gulf of Corinth, Greece. *Journal of Structural Geology* 31, 403-420.

Berg, S.S. and Skar, T. 2005. Controls on damage zone asymmetry of a normal fault zone: Outcrop analyses of a segment of the Moab fault, SE Utah. *Journal of Structural Geology* 27, 1803-1822.

Bjørlykke, K. 2010. Subsurface Water and Fluid Flow in Sedimentary Basins. *In* Bjørlykke, K. (ed). *Petroleum Geoscience: From Sedimentary Enviroments to Rock Physics*. New York: Springer, 259-279.

Braathen, A., Osmundsen, P.T. and Gabrielsen, R.H. 2004. Dynamic development of fault rocks in a crustal-scale detachment: An example from western Norway. *Tectonics* 23, 21.

Braathen, A., Tveranger, J., Fossen, H., Skar, T., Cardozo, N., Semshaug, S., Bastesen, E. and Sverdrup, E. 2009. Fault facies and its application to sandstone reservoirs. *American Association of Petroleum Geologists Bulletin* 93, 1-29.

Brenchley, P.J. and Rawson, P.F. 2006. *The geology of England and Wales*. 2 ed, Bath: The Geological Society Publishing House. 559 pp.

Bruhn, R.L., Parry, W.T., Yonkee, W.A. and Thompson, T. 1994. Fracturing and hydrothermal alteration in normal fault zones. *Pure and Applied Geophysics* 142, 609-644.

Buckley, S.J. 2010. *Lidar Intepretation and Manipulation Enviroment* (Version 0.4) Simon J. Buckley 2010 [Accsessed: 2010].

Caine, J., Evans, J. and Forster, C. 1996. Fault zone architecture and permeability structure. *Geology* 24, 1025-1028.

Chadwick, R. and Holliday, D. 1991. Deep crustal structure and Carboniferous basin development within the Iapetus convergence zone, northern England. *Journal of Geological Society* 148, 41-53.

Chadwick, R.A., Holliday, D.W., Holloway, S. and Hulbert, A.G. 1993. The evolution and hydrocarbon potential of the Northumberland–Solway Basin. *Petroleum Geology of Northwest Europe*, 717-726.

Chadwick, R.A., Holliday, D.W., Holloway, S., Hulbert, A.G. and Lawrence, D.J.D. 1995. *The structure and evolution of the Northumberland-Solway Basin and adjacent areas*, London: H.M. Stationary Office.

Chester, F. and Logan, J. 1986. Implications for mechanical properties of brittle faults from observations of the Punchbowl fault zone, California. *Pure and Applied Geophysics* 124, 79-106.

Clausen, J., Gabrielsen, R., Johnsen, E. and Korstgård, J. 2003. Fault architecture and clay smear distribution. Examples from field studies and drained ring-shear experiments. *Norwegian Journal of Geology* 83, 131-146.

Collier, R.E.L. 1989. Tectonic evolution of the Northumberland Basin; the effects of renewed extension upon an inverted extensional basin. *Journal of the Geological Society* 146, 981-989.

Corfield, S., Gawthorpe, R., Gage, M., Fraser, A. and Besly, B. 1996. Inversion tectonics of the Variscan foreland of the British Isles. *Journal of the Geological Society* 153, 17-32.

De Paola, N., Holdsworth, R. and McCaffrey, K. 2005a. The influence of lithology and pre-existing structures on reservoir-scale faulting patterns in transtensional rift zones. *Journal of the Geological Society* 162, 471-480.

De Paola, N., Holdsworth, R., McCaffrey, K. and Barchi, M. 2005b. Partitioned transtension: an alternative to basin inversion models. *Journal of Structural Geology* 27, 607-625.

Dunham, K.C. 1988. Pennine mineralisation in depth. *Proceedings of the Yorkshire Geological and Polytechnic Society* 47, 1-12.

Eichhubl, P., Davatz, N.C. and Becker, S.P. 2009. Structural and diagenetic control of fluid migration and cementation along the Moab fault, Utah. *American Association of Petroleum Geologists Bulletin* 93, 653-681.

Enge, H.D., Buckley, S.J., Rotevatn, A. and Howell, J.A. 2007. From outcrop to reservoir simulation model: Workflow and procedures. *Geosphere* 3, 469-490.

Faerseth, R.B. 2006. Shale smear along large faults: continuity of smear and the fault seal capacity. *Journal of Geological Society* 163, 741-751.

Faerseth, R.B., Johnsen, E. and Sperrevik, S. 2007. Methodology for risking fault seal capacity: Implications of fault zone architecture. *American Association of Petroleum Geologists Bulletin* 91, 1231-1236.

Ferrill, D.A. and Morris, A.P. 2003. Dilational normal faults. *Journal of Structural Geology* 25, 183-196.

Fossen, H. and Bale, A. 2007. Deformation bands and their influence on fluid flow. *American Association of Petroleum Geologists Bulletin* 91, 1685-1700.

Fossen, H. and Gabrielsen, R.H. 2005. *Strukturgeologi*: Fagbokforlaget.

Francis, E. 1982. Magma and sediment-I Emplacement mechanism of late Carboniferous tholeiite sills in northern Britain. *Journal of the Geological Society* 139, 1-20.

Fraser, A. and Gawthorpe, R. 1990. Tectono-stratigraphic development and hydrocarbon habitat of the Carboniferous in northern England. *Geological Society, London, Special Publications* 55, 49-86.

Fredman, N., Weranger, J., Cardozo, N., Braathen, A., Soleng, H., Roe, P., Skorstad, A. and Syversveen, A.R. 2008. Fault facies modeling: Technique and approach for 3-D conditioning and modeling of faulted grids. *American Association of Petroleum Geologists Bulletin* 92, 1457-1478.

Færsteth, R. 2010. Personal communication during field work. Cresswell.

Gabrielsen, R.H. 2010. The Structure and Hydrocarbon Traps of Sedimentary Basins. *In* Bjørlykke, K. (ed). *Petroleum Geoscience*: Springer, 299-327.

Gabrielsen, R.H. and Clausen, J.A. 2001. Horses and duplexes in extensional regimes: A scale-modeling contribution. *In* Koyi, H.A. and Mancktelow, N.S. (eds). *Tectonic modeling: a volume in honor of Hans Ramberg*. Boulder, Colerado: Geological Society of America, 192, 207-221.

Getmapping©. 2010. *Aerial Photography* 2010 [Accsessed: 2010]. Available at http://www2.getmapping.com/.

Gibbs, A.D. 1984. Structural evolution of extensional basin margins. *Journal of the Geological Society* 141, 609-620.

GoogleMaps™. 2011. *GoogleMaps* 2011 [Accsessed: 2011]. Available at http://maps.google.no.

Harding, T.P. 1985. Seismic characteristics and identification of negative flower structures, positive flower structures, and positive structural inversion. *American Association of Petroleum Geologists Bulletin* 69, 582-600.

Haszeldine, R. 1984. Muddy deltas in freshwater lakes, and tectonism in the Upper Carboniferous Coalfield of NE England. *Sedimentology* 31, 811-822.

Heynekamp, M.R., Goodwin, L.B., Mozley, P.S. and Haneberg, W.C. 1999. Controls on fault-zone architecture in poorly lithified sediments, Rio Grande Rift, New Mexico; implications for fault-zone permeability and fluid flow. *In* Haneberg, W.C., Mozley, P.S., Moore, C.J. and Goodwin, L.B. (eds). *Faults and subsurface fluid flow in the shallow crust*. Geophysical Monograph. 113. Washington, D.C.: American Geophysical Union, 27-49.

Holcombe, R. *GeoOrient©* 2010 [Accsessed. Available at http://www.holcombe.net.au/software/.

Jackson, J., Gagnepain, J., Houseman, G., King, G., Papadimitriou, P., Soufleris, C. and Virieux, J. 1982. Seismicity, normal faulting, and the geomorphological development of the Gulf of Corinth (Greece): the Corinth earthquakes of February and March 1981. *Earth and Planetary Science Letters* 57, 377-397.

Jackson, J. and McKenzie, D. 1983. The geometrical evolution of normal fault systems. *Journal of Structural Geology* 5, 471-482.

Johnson, G.A.L. 1984. Subsidence and sedimentation in the Northumberland Trough. *Proceedings of the Yorkshire Geological Society* 45, 71-83.

Jones, J.M. 1968. The geology of the coast section from Tynemouth to Seaton Sluice. *Transactions of the Natural History Society of Northumberland, Durham, and Newcastle-upon-Tyne* 16, 153-192.

Kim, Y.S., Andrews, J.R. and Sanderson, D.J. 2000. Damage zones around strike-slip fault systems and strike-slip fault evolution, Crackington Haven, southwest England. *Geosciences Journal* 4, 53-72.

Kim, Y.S., Peacock, D.C.P. and Sanderson, D.J. 2002. Mesoscale strike-slip faults and damage zones at Marsalforn, Gozo Island, Malta. *Journal of Structural Geology* 25, 793-812.

Kimbell, G.S., Chadwick, R.A., Holliday, D.W. and Werngren, O.C. 1989. The structure and evolution of the Northumberland Trough from new seismic reflection data and its bearing on modes of continental extension. *Journal of the Geological Society* 146, 775-787.

Kjemperud, M.V. 2011 *Fault architecture of reactivated faults in Carboniferous sediments, Northumberland, GB* Geological Institute, University of Oslo (UiO) and Centre for integrated Petroleum Research (CiPR), Oslo.

Knipe, R.J., Fisher, Q.J., Jones, G., Clennell, M.R., Farmer, A.B., Harrison, A., Kidd, B., McAllister, E., Porter, J.R. and White, E.A. 1997. Fault seal analysis: successful methodologies, application and future directions. *Norwegian Petroleum Society Special Publications* 7, 15-38.

Land, D.H., Calver, M. and Harrison, R.K. 1974. *Geology of the Tynemouth district*, London: H.M. Stationery Office Books (TSO).

Leeder, M.R. 1974. The origin of the Northumberland basin. *Scottish Journal of Geology* 10, 283-296

Lindanger, M., Gabrielsen, R. and Braathen, A. 2007. Analysis of rock lenses in extensional faults. *Norwegian Journal of Geology* 87, 361-372.

Liss, D., Owens, W. and Hutton, D. 2004. New palaeomagnetic results from the Whin Sill complex: evidence for a multiple intrusion event and revised virtual geomagnetic poles for the late Carboniferous for the British Isles. *Journal of the Geological Society* 161, 927-938.

Martel, S.J. 1999. Mechanical controls on fault geometry. *Journal of Structural Geology* 21, 585-596.

Mort, K. and Woodcock, N.H. 2008. Quantifying fault breccia geometry: Dent Fault, NW England. *Journal of Structural Geology* 30, 701-709.

Nelson, E.P., Kullman, A.J., Gardner, M.H. and Batzle, M. 1999. Fault-fracture networks and related fluid flow and sealing, Brushy Canyon Formation, West Texas. *In* Haneberg, W.C., Mozley, P.C., Moore, J.C. and Goodwin, L.B. (eds). *Faults and subsurface fluid flow in the shallow crust*. Washington, DC: American Geophysical Union, 113, 69-81.

Nystuen, J.P. 1989. *Rules and recommendations for naming geological units in Norway*. Edited by Nystuen, J.P. Norsk geologisk tidsskrift. 69, suppl 2: Univ.-Forlaget. 111 pp.

O'Mara, P. and Turner, B. 1999. Sequence stratigraphy of coastal alluvial plain Westphalian B Coal Measures in Northumberland and the southern North Sea. *International Journal of Coal Geology* 42, 33-62.

Odling, N.E., Harris, S.D. and Knipe, R. 2004. Permeability scaling properties of fault damage zones in siliclastic rocks. *Journal of Structural Geology* 26, 1727-1747.

Richard, P. and Krantz, R.W. 1991. Experiments on fault reactivation in strike-slip mode. *Tectonophysics* 188, 117-131.

Schulz, S.E. and Evans, J.P. 2000. Mesoscopic structure of the Punchbowl Fault, Southern California and the geologic and geophysical structure of active strike-slip faults. *Journal of Structural Geology* 22, 913-930.

Shipton, Z.K. and Cowie, P.A. 2002. A conceptual model for the origin of fault damage zone structures in high-porosity sandstone. *Journal of Structural Geology* 25, 333-344.

Sibson, R.H. 1977. Fault rocks and fault mechanisms. *Journal of the Geological Society* 133, 191-213.

Sibson, R.H. 1996. Structural permeability of fluid-driven fault-fracture meshes. *Journal of Structural Geology* 18, 1031-1042.

Smith, D.B. 1970. Submarine slumping and sliding in the Lower Magnesian Limestone of Northumberland and Durham. *Proceedings of the Yorkshire Geological Society*, 1-36.

Stewart, I.S. and Hancock, P.L. 1988. Normal fault zone evolution and fault scarp degradation in the Aegean region. *Basin research* 1, 139-153.

Stewart, I.S. and Hancock, P.L. 1991. Scales of structural heterogeneity within neotectonic normal fault zones in the Aegean region. *Journal of Structural Geology* 13, 191-204.

Wallace, W. 1861. Of the laws regulating the descent of water below the surface of the earth. *The laws which regulate the deposition of lead ore in veins: illustrated by an examination of the geological structure of the mining districts of Alston Moor*. The formation and geological structure of the mining districts of Alston Moor. Book 1. London: Stanford, E., 109-141.

Whitworth, T., Haneberg, W., Mozley, P. and Goodwin, L. 1999. Solute-sieving-induced calcite precipitation on pulverized quartz sand: Experimental results and implications for the membrane behavior of fault gouge. *In* Haneberg, W.C., Mozley, P.C., Moore, C.J. and Goodwin, L.B. (eds). *Faults and subsurface fluid flow in the shallow crust*. Washington D.C: American Geophysical Union, 113, 149-158.

Wibberley, C.A.J., Yielding, G. and Di Toro, G. 2008. Recent advances in the understanding of fault zone internal structure: a review. *Geological Society, London, Special Publications* 299, 5-33.

Ziegler, P.A. 1990. Tectonic and palaeogeographic development of the North Sea rift system. *In* Blundell, D. and Gibbs, A.D. (eds). *Tectonic Evolution of the North Sea Rifts* International Lithosphere Programme: Oxford University Press, 1-36.

Appendix

Appendix A- Thin sections

Appendix AI- Thin sections Snab Point

Appendix AII- Thin sections Crag Point

Appendix B- key figures magnified

Appendix BI- Sketches of fault 1 Snab Point

Appendix BII-Sketch and LiDAR scan figure of horst and graben system Crag Point

Appendix A

Thin sections

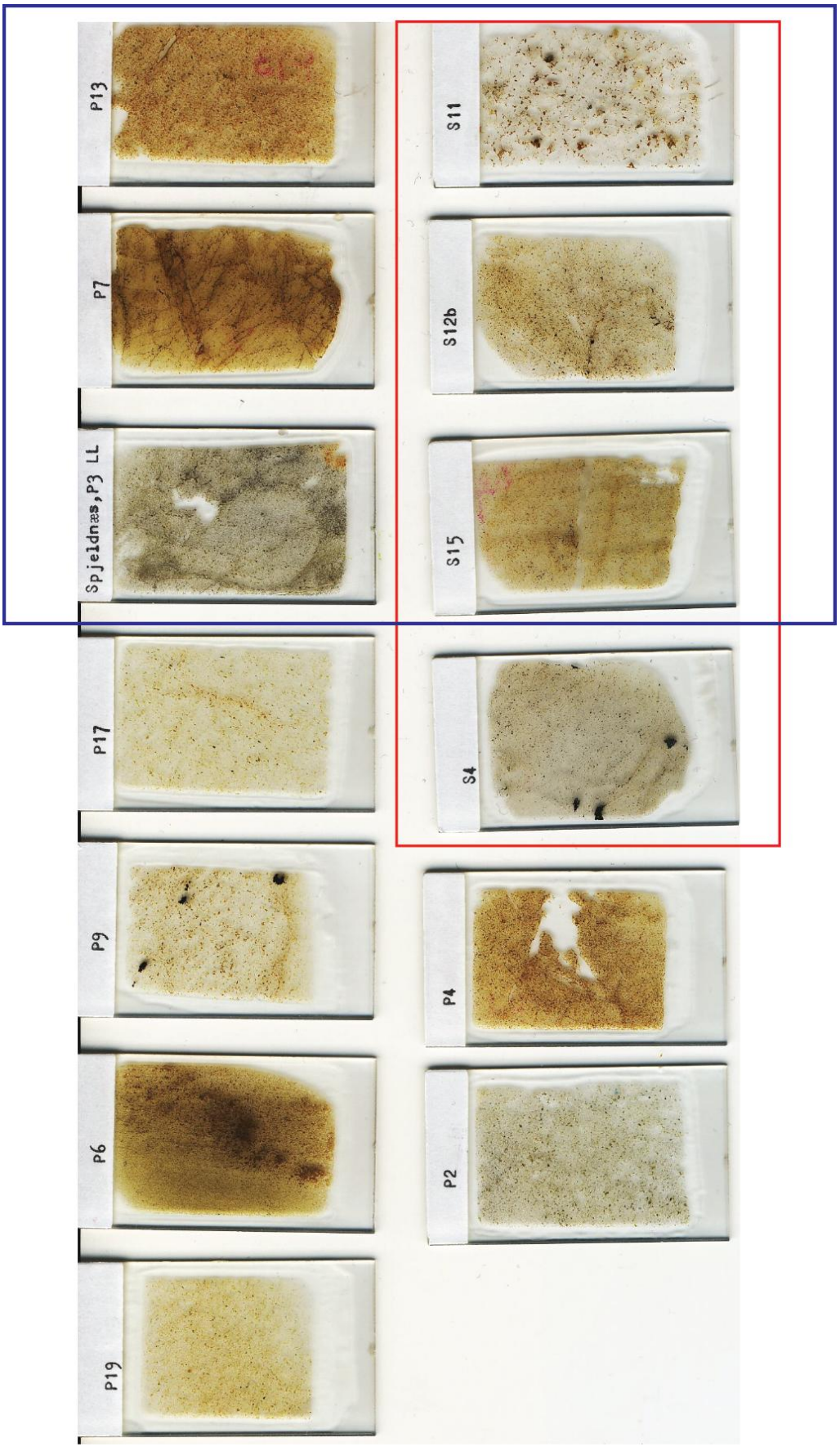

Figure 1 All thin sections made from the localities. The ones within the red square is from Crag Point. The ones within the blue square have been looked at in microscope.

Appendix A I

Thin sections

Snap Point

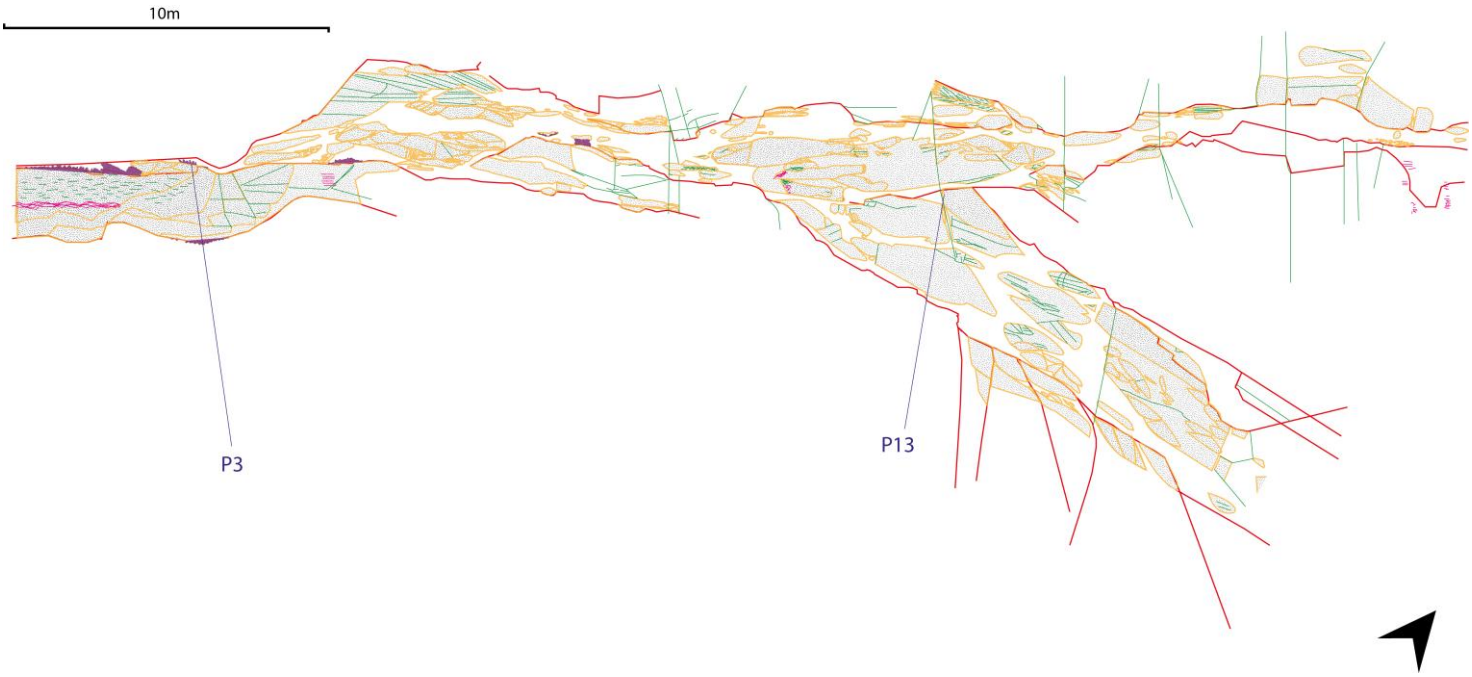

Figure 2 Location of thin sections taken from sample P3 and P13

a

b

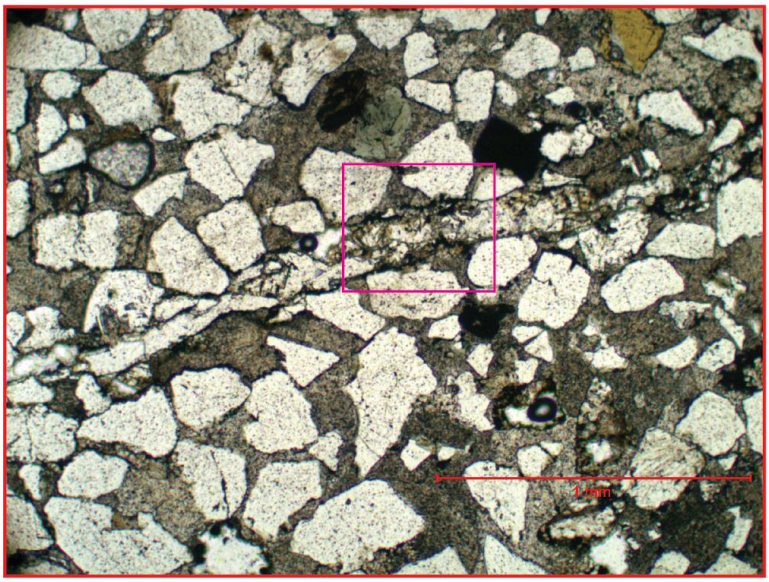

c

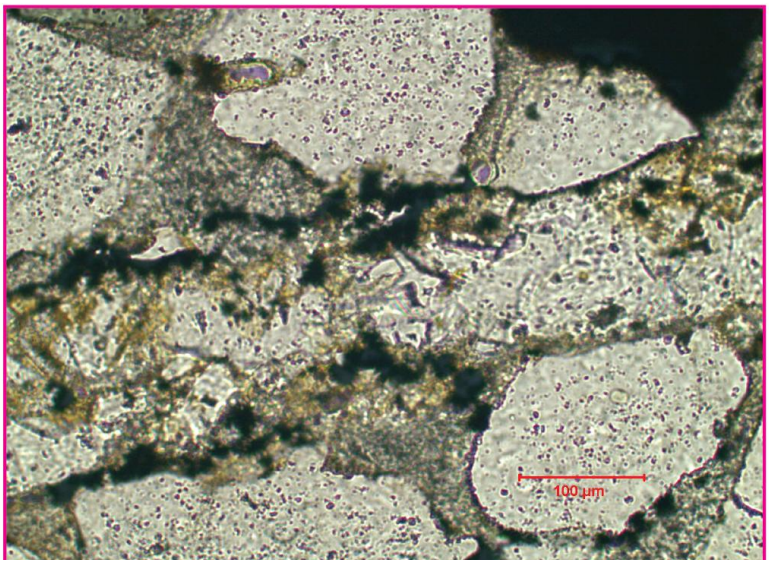

Figure 3 Sample P3. Breccia from segment 1.1 domain a Snab Point.
a) Scan of thin section
b) deformation band within thin section. Notice calcite cementation between grains (red line marks 1mm.
c) Close up of deformation band

a

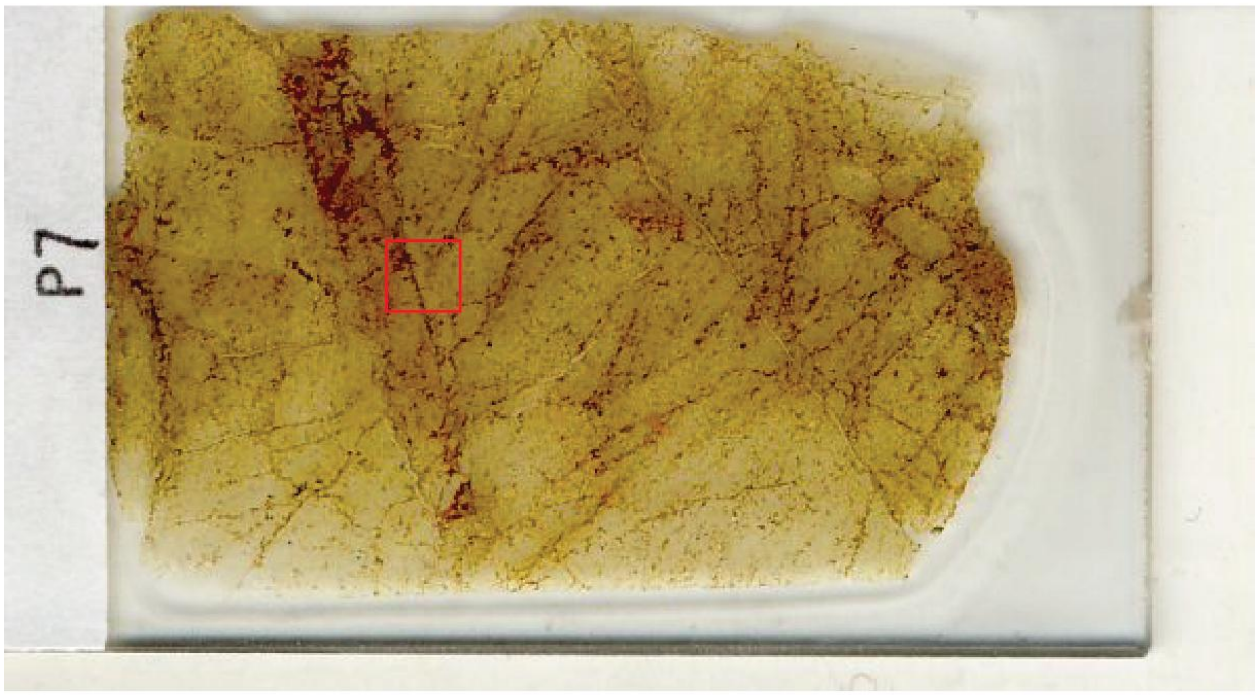

b

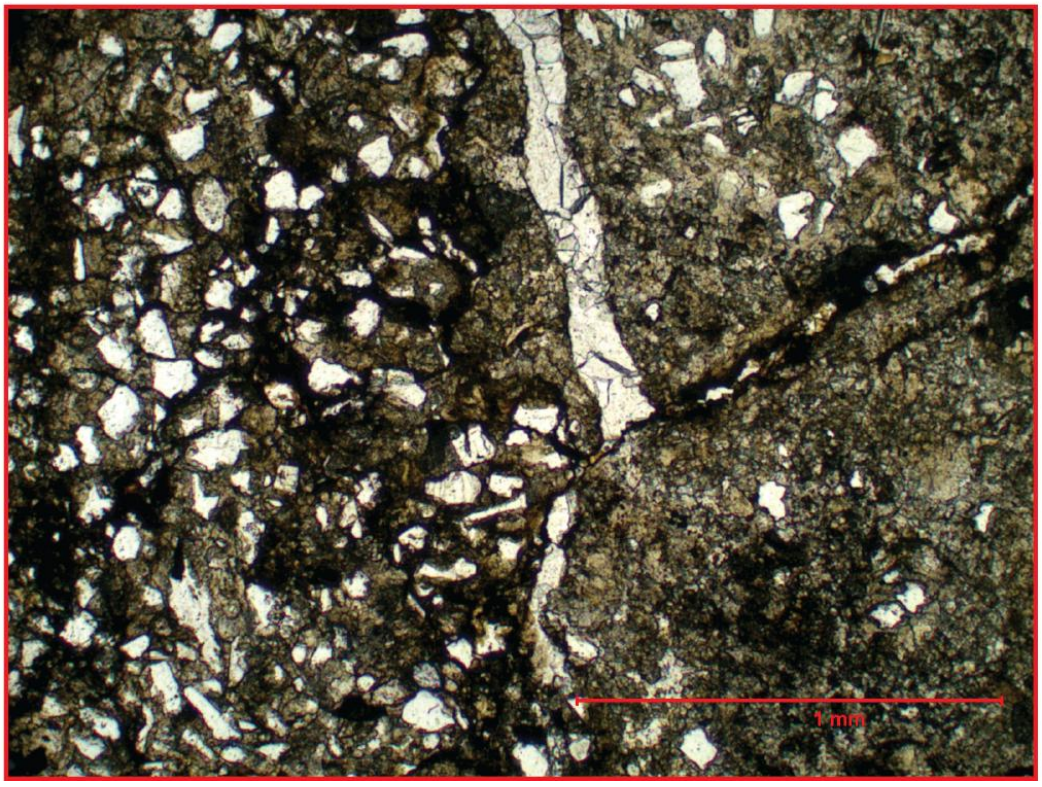

Figure 4 P7 Snab Point from loose breccia sample from the core of segment 1.1 domain a
a) Scan of thin section
b) Close up of fracture. The fracture is separated from the rest of the rock by a mineral-filled vein. Notice some degree of calcite cemetation (red line marks 1mm)

a

b

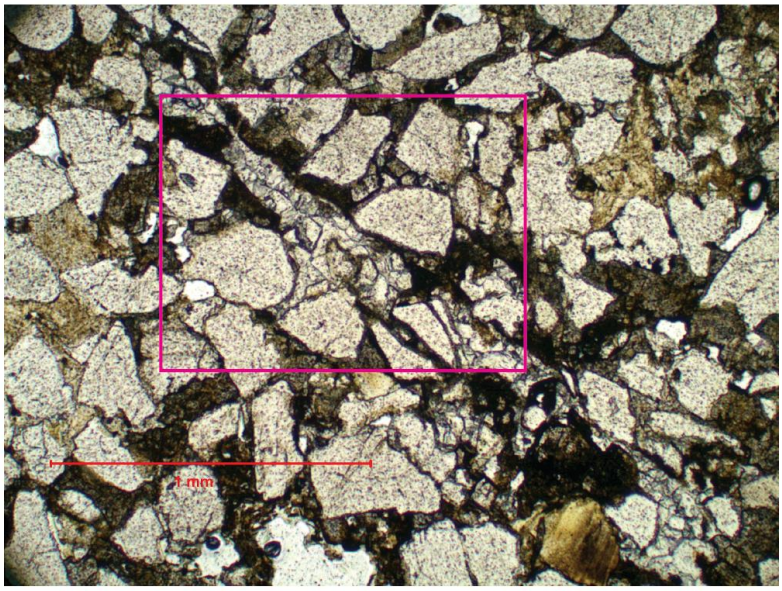

c

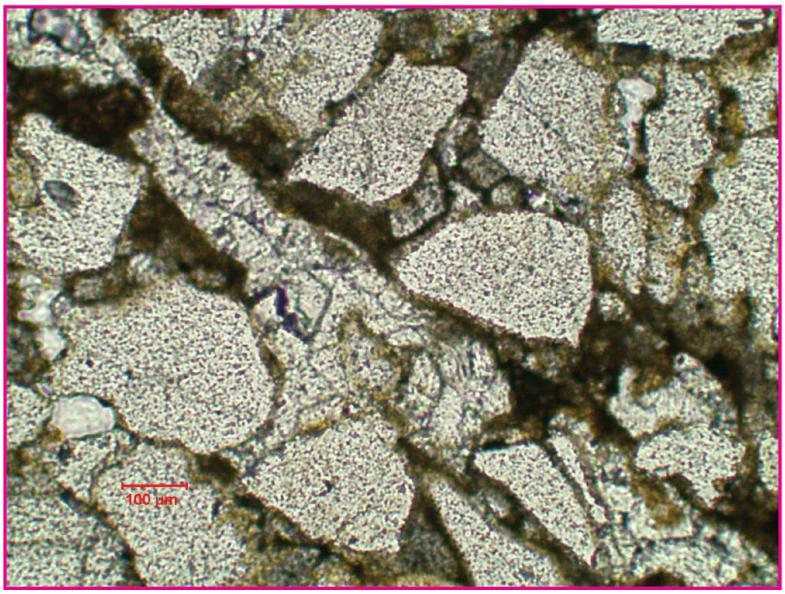

Figure 5 P13 From core in intersection between segment 1.1 and branch 1.1
a) Scan of thin section
b) Fracture with elements of nearby grains (notice some degree of sedimentation)
c) Close up of fractue

Appendix A II

Thin sections

Crag Point

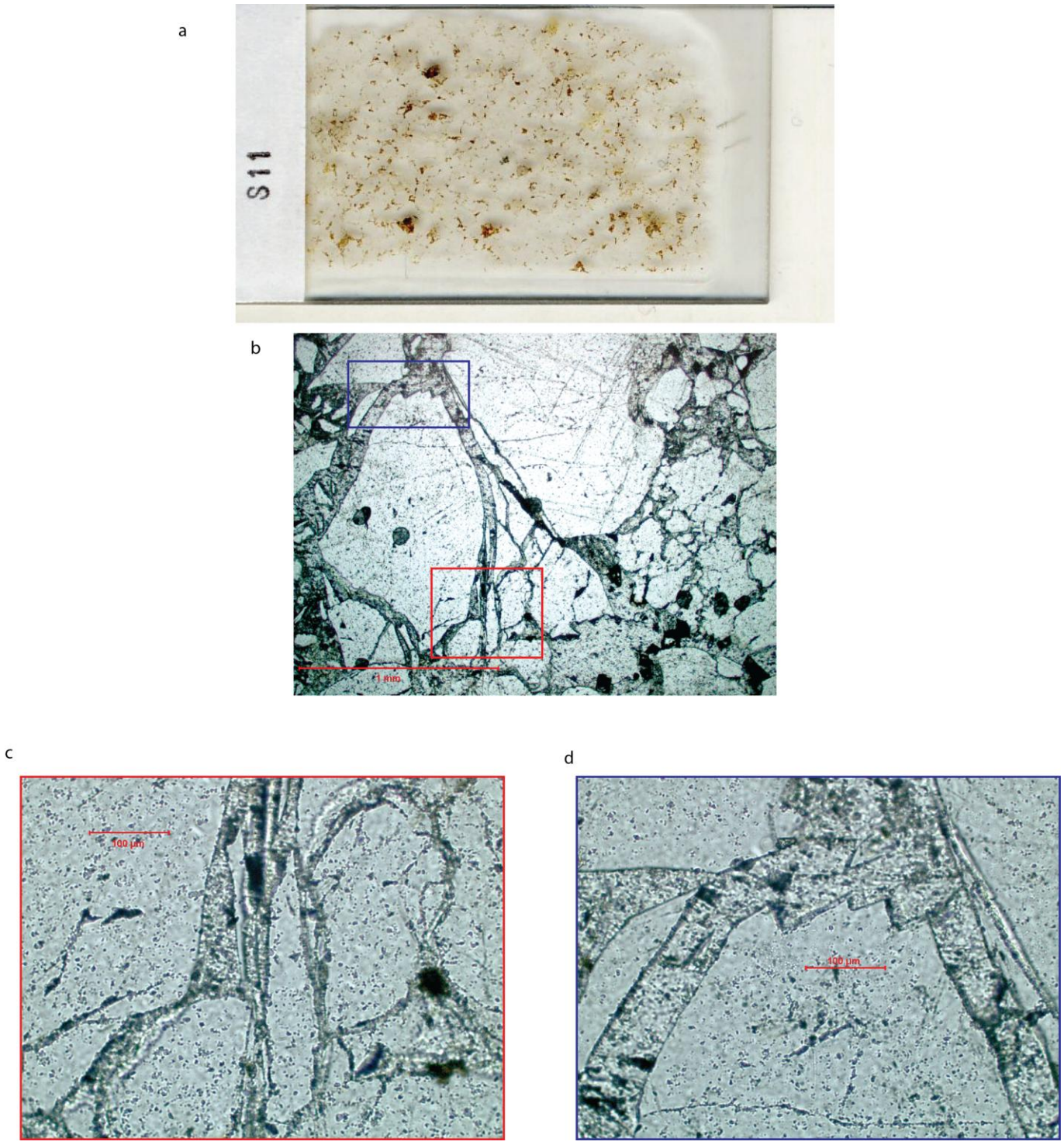

Figure 6 S11 Core of Crag Point Fault breccia #1
a) Scan of thin section
b) Fractured clasts with some cement and lens shaped pieces in between
c) Close up of red area displaying lens shaped pieces
d) Close up of rough edged sand grain

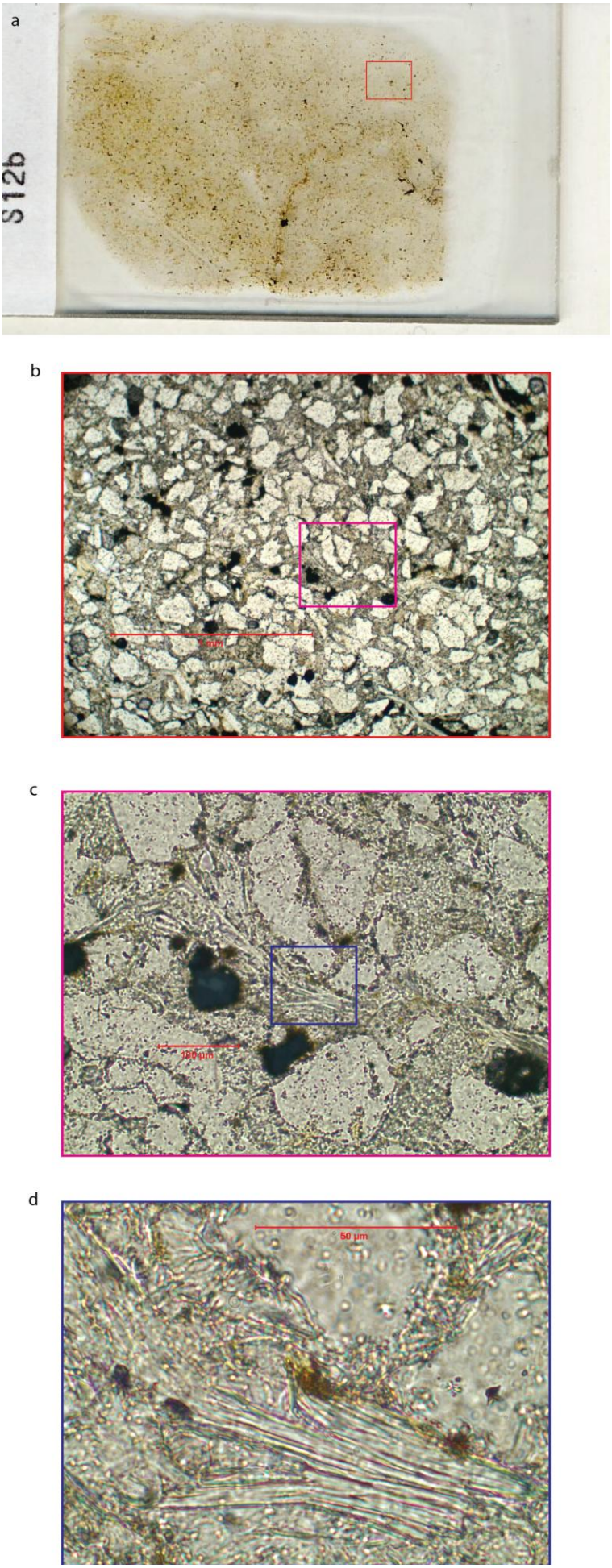

Figure 7 S12b From matrix of breccia within footwall of Crag Point Fault (figure 3.2.21)
a) Scan of thin section
b) Matrix composition with cementation
c) Possible fracture
d) Close up of possible fracture

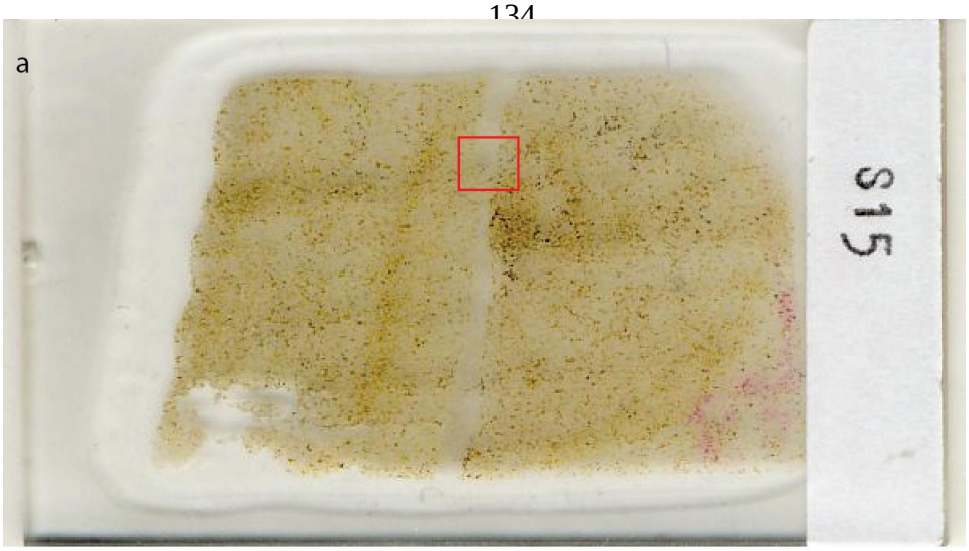

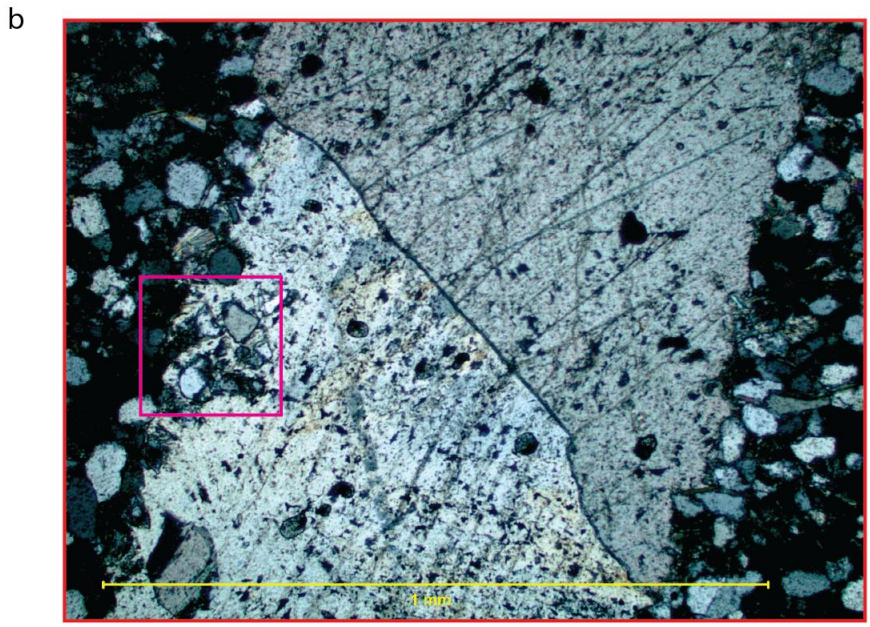

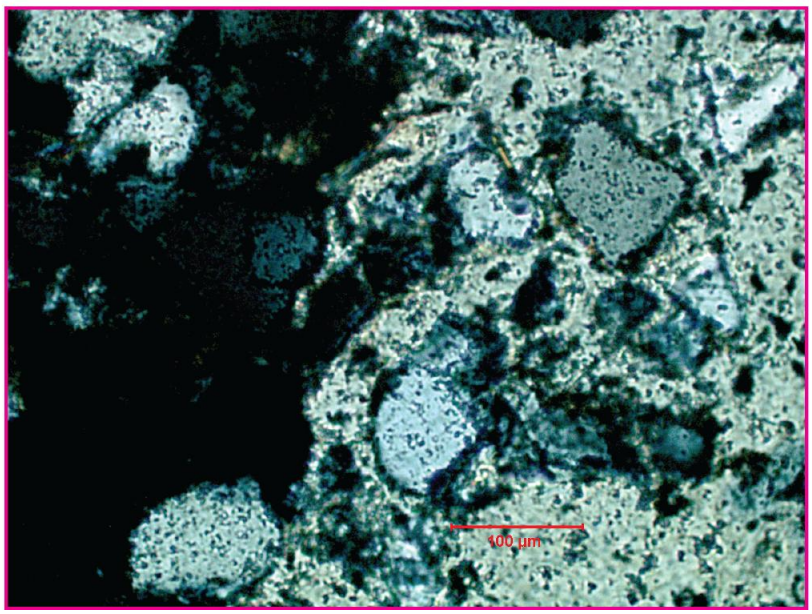

Figure 8 S8 From first graben (close to first horst) in horst and graben system Crag Point
a) Scan of thin section showing fracture
b) Close up of calcite filled fracture (yellow line marks 1mm)
c) Close up of fracture edge

Appendix B

Appendix B II, Snab Point

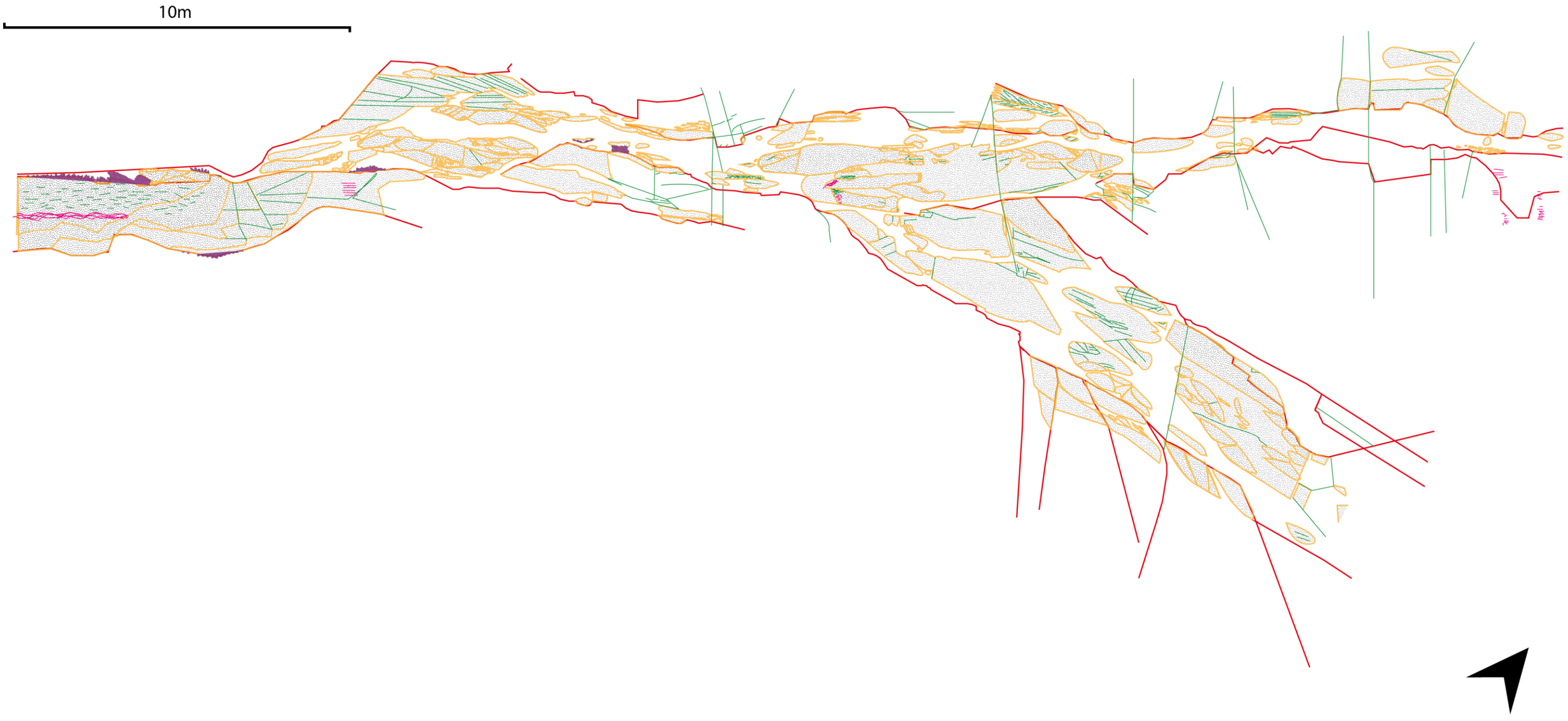

Figure 9 Segment 1.1 along strike. Lenses within yellow borders. Red- master branchlines. Green-fractures. Purple-breccia. Pink-deformation bands.

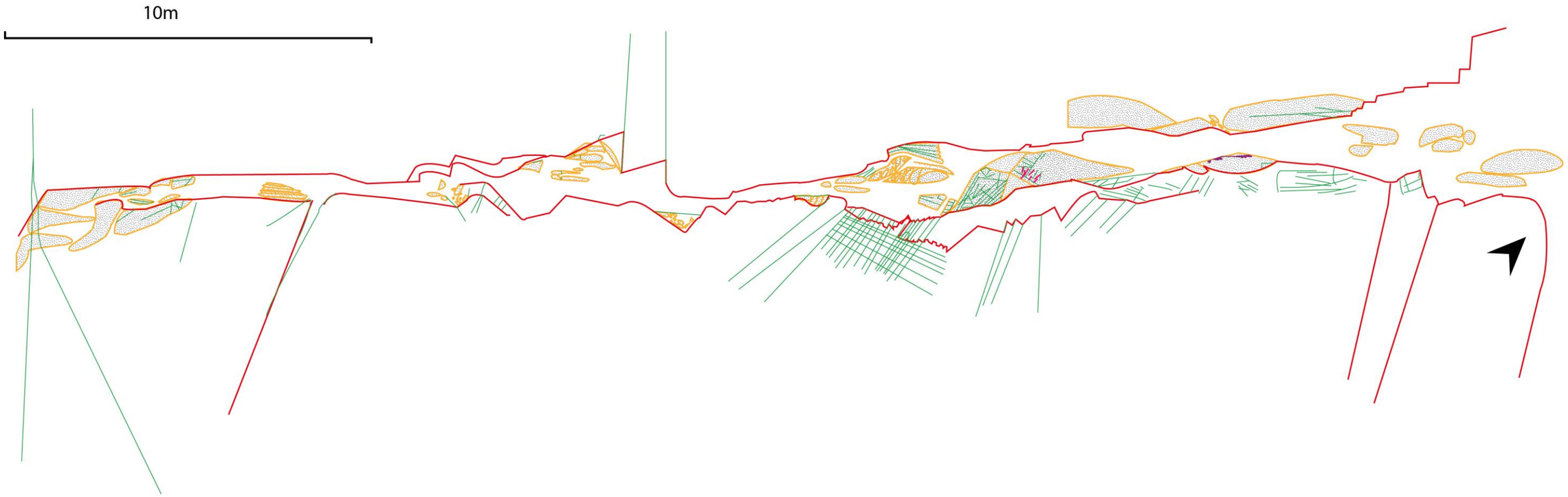

Figure 10 Segment 1.2 along strike. Lenses within yellow borders. Red- master branchlines. Green-fractures. Purple-breccia. Pink-deformation bands.

Appendix B II, Crag Point

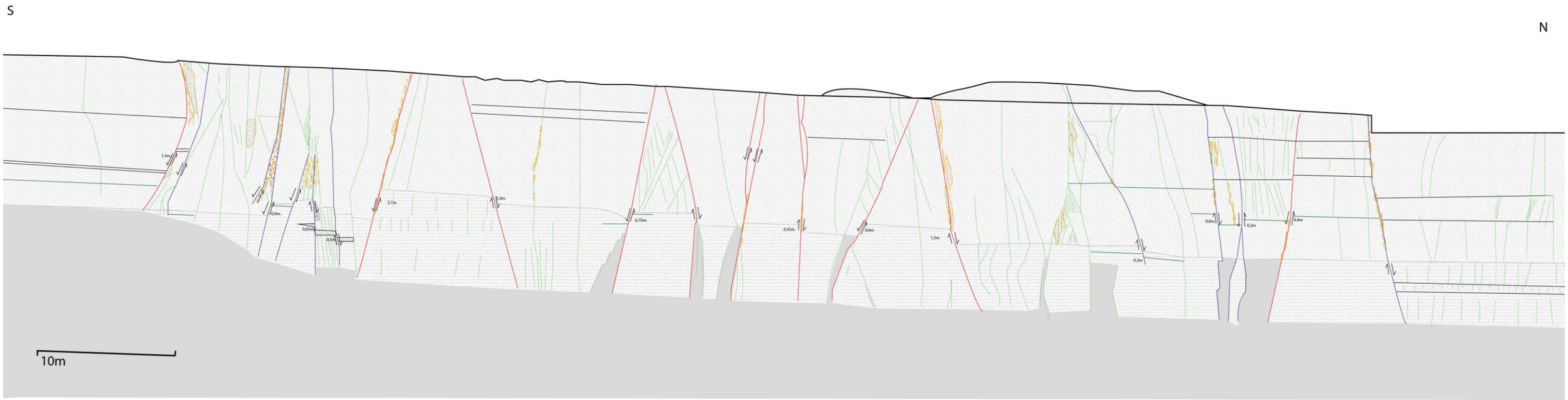

Figure 11 Horst and graben system, vertical section

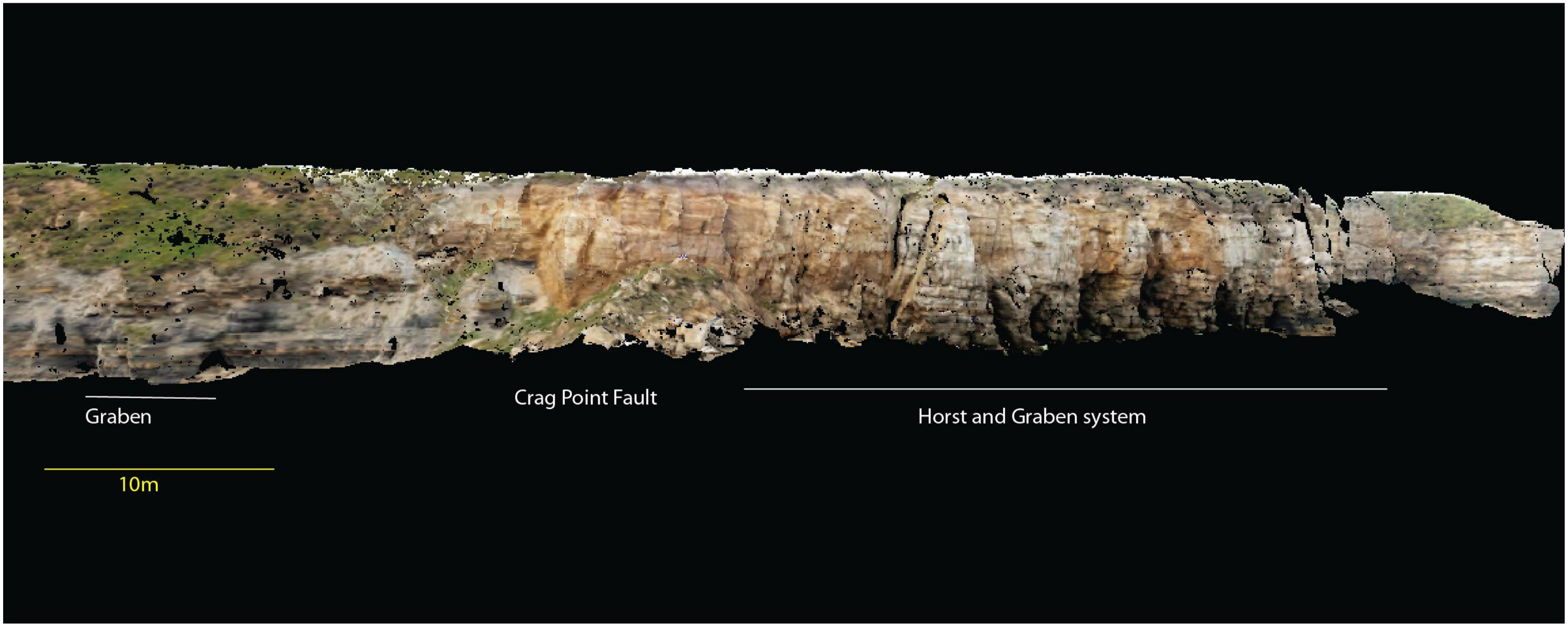

Figure 12 Crag Point field site from LiDAR scan data